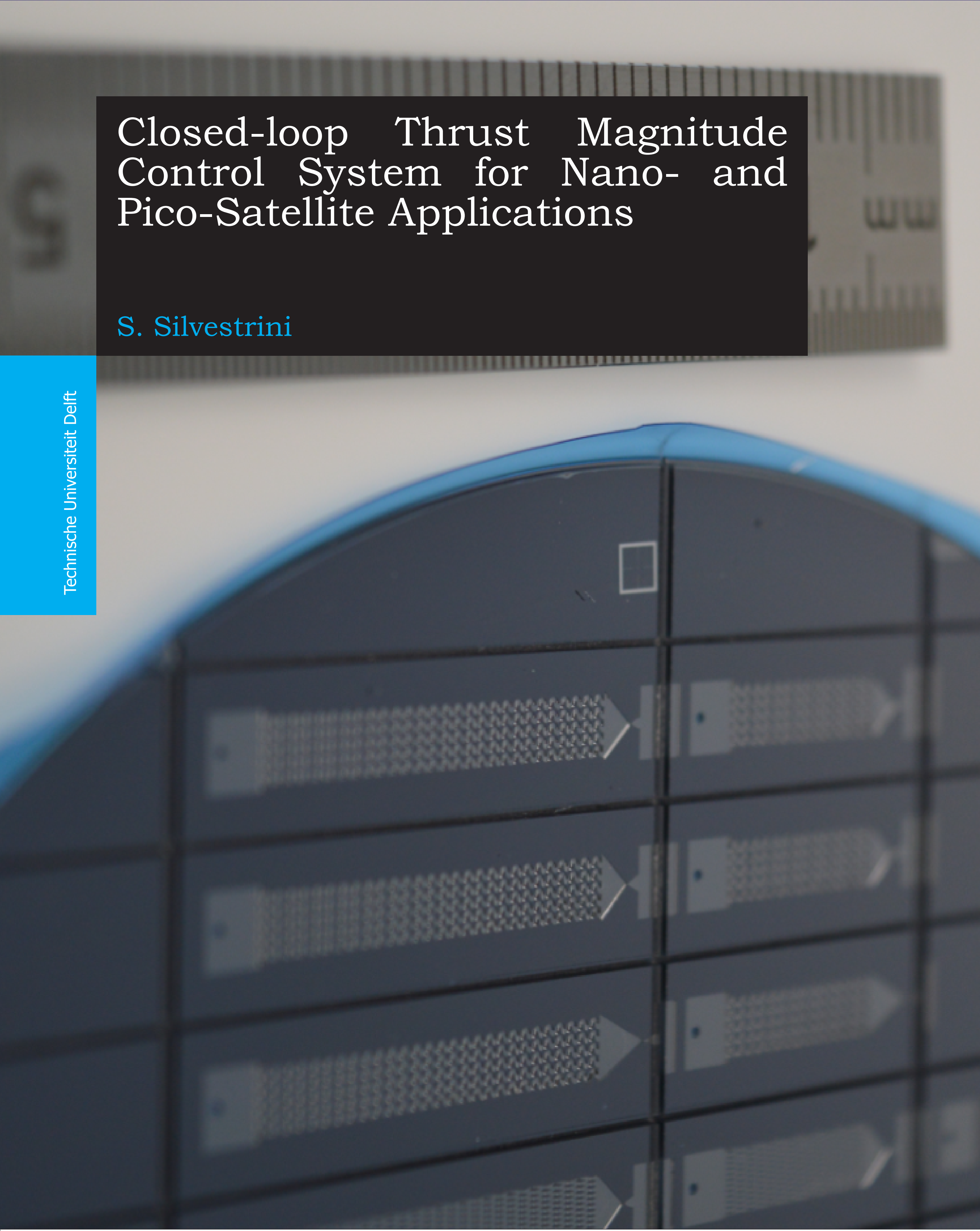

Closed-loop Thrust Magnitude Control System for Nano- and Pico-Satellite Applications

S. Silvestrini

Technische Universiteit Delft

Challenge the future

Closed-loop Thrust Magnitude Control System for Nano- and Pico-Satellite Applications

by

S. Silvestrini

in partial fulfillment of the requirements for the degree of

Master of Science
in Aerospace Engineering

at the Delft University of Technology,
to be defended publicly on Thursdayy July 27, 2017 at 14:00.

Student number:	4517261	
Project duration:	December 12, 2016 – July 27, 2017	
Supervisor:	Dr. A. Cervone	
Daily Supervisor:	M. de Athayde Costa e Silva	
Thesis committee:	Dr. Ir. C. J. M. Verhoeven,	TU Delft - LR-SSE
	Dr. Ir. E. Mooij,	TU Delft - LR-ASM
	Dr. M. K. Ghatkesar,	TU Delft - 3ME

TU Delft Delft University of Technology

Preface

This thesis represents the ultimate effort to earn the Master of Science Degree at the Aerospace Engineering faculty in TU Delft. Such project challenged me in several engineering fields, from space propulsion to mechatronics, from control engineering to microfluidic. In addition, both theoretical and experimental work was carried in order to develop the system as a whole. To me, the possibility to merge different disciplines was an incredible added value of this thesis. Beside the professional growth that this work enabled, I would like to underline the impact it had on my personality. The thesis has been a true platform to test my non-technical capabilities: the perseverance required to carry out the work, the dedication to a personal product and, above all, the passion towards research. Also, this thesis allowed me to be accepted and attend the International Astronautics Conference 2017 in Adelaide, Australia, which represents a invaluable experience for my professional life.

Important steps in life require important people. I am extremely grateful to Marsil de Athayde Costa e Silva, my daily supervisor, for his constant support and the friendly relationship we established during the last months. I would like to thank Dr. Cervone for his guidance and precious hints, always at the right moment in time. Also, I would like to thank all the committee members that showed interest in my work: I hope you will like it until the end!
Many words could be said to the large amount of friends I made during these two years at TU Delft but I will keep it short: I have learnt something from everyone of you and, somehow, you shaped the person I ended up being.
Last, but of course not least, I would like to thank my family for the unconditional love and support: you simply taught me how to live, and that is quite significant in life!

S. Silvestrini
Delft, July 2017

Abstract

The growing needs of nano- and pico-satellite missions require several enhancements in micro-propulsion capabilities to enable the satellites to perform an increasing variety of orbital maneuvers. Among them, the possibility to accurately control the thrust would open up new scenarios for nano- and pico-satellites applicability to include, for example, missions such as space debris removal and orbit transfer.

This thesis presents the design and the implementation of a closed-loop control system for thrust magnitude regulation in micro-resistojets. This is achieved by controlling the propellant mass flow in the micro-valve of the feeding system which is designed to make extensive use of off-the-shelf components. The Vaporizing Liquid Micro-resistojet (VLM) is one of the micro-thrusters under development at TU Delft and, for this reason, it is selected for performing the tests. The outcome of this work is meant to give insights into the design and performance level of future technologies for thrust magnitude control, which will be designed and manufactured at TU Delft. In order to develop appropriate controllers, a non-linear state-space model of the micro-valve system is developed analytically. The model includes different domains, such as electro-magnetic, fluid and mechanical, in order to bring together the complex dynamic behavior of the actuator. The performance of the analytical model is compared to a more sophisticated multi-domain analysis performed with finite element method (FEM) and computational fluid dynamics (CFD). Two controllers, namely PID (proportional-integral-derivative) and SMC (sliding mode control), are designed and tested using the models developed. The ON/OFF micro-valves are controlled with PWM (pulse width modulation) by tuning the operating duty cycle. A hybrid sliding mode control scheme is developed based on the insights gave by the experiments, which enables the thrust magnitude control of the comprehensive system.
Finally, the closed-loop control system is implemented in the preliminary hardware design of the micropropulsion system. The experimental set-up comprises the propellant tank, the micro-valve, the micro-thruster, the feeding channel, pressure and temperature sensors and the processing microcontroller. The tests are focused on the performance of the controller, and the fine tuning of its parameters, and also in the validation of the design approach.

The controlled micro-propulsion system delivers the commanded input with a response time of $\sim 1.5\ s$ and a resolution of $50\ mbar$ in the chamber pressure. As a first implementation of a control system for micro-propulsion at TU Delft, the results are promising and certainly pave the way for future developments on this research field.

Contents

List of Figures

List of Tables

Acronyms and Symbols

Acronym	Description
CFD	Computational Fluid Dynamics
DC	Duty Cycle
FEM	Finite Element Method
IAE	Integral Absolute Error
ISE	Integral Squared Error
ITAE	Integral Time-weighted Absolute Error
MCU	Micro Controller Unit
MEMS	Micro Electro-Mechanical Systems
PID	Proportional-Integral-Derivative
PWM	Pulse Width Modulation
SMC	Sliding Mode Control
VLM	Vaporizing Liquid Micro-Resistojet

Symbol	Units	Description
Latin		
A	m^2	Area
a	m	Bottom iron strips length
c	$N \cdot s \cdot m^{-1}$	Viscous coefficient
C_d	-	Discharge coefficient
c_p	$J \cdot kg^{-1} \cdot K^{-1}$	Specific heat at constant pressure
c_v	$J \cdot kg^{-1} \cdot K^{-1}$	Specific heat at constant volume
dg_0	m	Initial upper air gap
d_{in}	m	Inlet diameter
d_{sol}	m	Solenoid diameter
F	N	Force
g	m	Side air gap
h	$J \cdot kg^{-1}$	Specific enthalpy
i	A	Electric current
I_{sp}	s	Specific impulse
k	$N \cdot m^{-1}$	Elastic spring constant
L	H	Inductance
L_0	m	Initial valve cavity length
M	kg	Mass
$\dot{m}$	$kg \cdot s^{-1}$	Mass flowrate
$Ma(M_x)$	$-$	Mach number
N	$-$	Number of coil turns
p	Pa	Pressure
Q	$m^3 \cdot s^{-1}$	Volumetric flowrate
R	Ω	Electric resistance
T	K	Temperature
t	s	Time
$\begin{pmatrix} u \\ v \\ w \end{pmatrix}$	$m \cdot s^{-1}$	Velocity components

V	m^3	Volume
v	V	Voltage
Greek		
γ	$-$	Specific heat ratio
Δ	$-$	Difference in values. Delta.
ϵ_0	$F \cdot m^{-1}$	Vacuum electric permittivity
ζ	$-$	Loss coefficient
λ	$Wb - turns$	Flux linkage
μ	$Pa \cdot s$	Dynamic viscosity
μ_0	$H \cdot m^{-1}$	Vacuum electromagnetic permeability
ρ	$kg \cdot m^{-3}$	Density
σ	Pa	Normal stress
σ_{SMC}	$-$	SMC Sliding surface
τ	Pa	Shear stress
Φ	Wb	Magnetic flux

1

Introduction

The promising development of nano-satellites requires a continuous improvement of their capabilities to achieve mission goals, which were originally fulfilled only by traditional large spacecraft. Miniaturization of propulsion modules is targeted to this aim; furthermore, there is a need to progress in such modules to a more sophisticated control functionality, enabling the nano-satellite to perform precise flight maneuvers (e.g. formation flight). In particular, a closed-loop control system would enable a fine tuning of the delivered thrust; the thrust magnitude control can be achieved by controlling the propellant mass flow within the microvalve and microchannels of the feeding system. In order to develop the control concepts, a mathematical model, which describes the fluid flow in microscale as a dynamical system, is necessary. The inherent non linearity and complexity of a fluid system require several analysis on the accuracy of a state-space model to describe its dynamics; alongside of such investigations, stability analysis and specific controllers need to be assessed and evaluated by taking into account propulsive parameters, such as I_{sp}, response time and thrust range itself. One major challenge of such project is the miniaturization of all its constituents. As far as the control loop is concerned, the micro-valve is the most critical device within the system. Thus, a possible hardware architecture needs to be tested complying with size, power and mass constraints of a pico-satellite mission, such as the TU Delft-PocketQube one.

1.1. Motivation

An effective way to enhance micropropulsion capabilities of nano- and pico-satellites is to adopt a closed-loop thrust magnitude control system that enables accurate maneuver and thruster's firing using a desired propellant flowrate. It is retained that the implementation of a closed-loop control for regulating the thrust magnitude increases the flexibility and agility of the micro-propulsion system for nano- and pico-satellite applications [9]. The fine orbital maneuvers, such as scanning control [10] for instance, require a precise and stable thrust, which may vary in intensity throughout the mission. When choosing a micro-propulsion system, the application is critical for determining the requirements it needs to respect. For example, to perform attitude control maneuvers, the minimum thrust, and pulse time, is required to be tiny to ensure precise pointing accuracy of the satellite [11], on the other hand the thrust level is required to be significantly higher to perform optimal orbital maneuvers. These twofold requirements can be solved by implementing a stable and precise closed-loop control system for thrust regulation. Moreover, implementing a control system would enable a constant and stable thrust level for extended time even in simple blowdown systems, as long as the intensity is lower than the maximum deliverable thrust. Several research questions are posed to be answered to achieve its realization:

1. How can the flow within a microvalve and its actuation be modelled as a dynamic system?
    - What are the equations to be used to properly model fluid-flow in microscale?
    - What are the major assumptions (geometrical and related to fluid properties) that can be made to simplify the equations?

  - How can the equations be turned into a state-space representation for control purposes?
  - How accurately can a state-space model describe the dynamics in a microvalve?
  - How do the parameters set in the model affect the output of the model?
2. How can the controllers be designed to execute the aforementioned task successfully?
  - Which are the most suitable techniques for fluid flow control?
  - Is the dynamic system stable together with the control-loop? What are the results of the system's stability and frequency analysis?
  - Are linear Proportional Integral Derivative (PID) controllers the only candidates to be investigated? Are the other strategies suitable for the scope of fluid-flow control, such as Sliding Mode Control (SMC)?
  - What are the theoretical performances of the simulated system (thruster + closed-loop control system) in terms of typical control parameters, such as response time, thrust resolution and thrust range?
3. What is a potentially suitable architecture of the actual closed-loop control system to be implemented in the TU Delft-PocketQube?
  - Are there any miniaturized solution that would suit the limited size of the TU Delft-PocketQube?
  - What is the required electronics to implement a closed-loop system?
  - What are the actual performances of the tested system (thruster + closed-loop control) in terms of typical control parameters, such as response time, thrust resolution and thrust range?
  - How adherent are simulated results to test data?

The project goal is to improve and enhance micropropulsion capability of nano- and pico-satellites by implementing a closed-loop thrust magnitude control system achieved by controlling the propellant mass flow through the microvalve and in the micro channels of the feeding system. The micro-propulsion system will make use of the vaporizing liquid micro-resistojet (VLM) developed at TU Delft and the control system is designed to control the thrust up to 1 mN, utilizing a maximum pressure of 5 bar in the propellant tank. Finally, the controlled system has to be designed to comply with nano- and pico-satellite size standards.

In order to achieve the main objective, several sub-objectives have been identified, which will then represent milestones in the planning process.

- Describe the flow within a electromagnetic solenoid-actuated microvalve as a dynamical system by derivation from Navier-Stokes equations. Together with the fluid flow modelling, the actuation of the valve needs to be described in terms of the electro-magnetic actuation.
- Develop a CFD model of the flow within the microvalve and compare numerical results with simulation outcomes.
- Develop the controllers for fluid mass flowrate by using Proportional-Integral-Derivative (PDI) control and investigate other potential control strategies, such as Sliding Mode Control (SMC).
- Test the model and deliver theoretical simulation-based results upon its performance.
- Test and practically implement the coupled system made up by the control system together with the microthruster.

The MSc thesis project is divided into two phases, which own different perspective on the work to be done. The first part is a theoretical approach used to simulate and analyze system's performance; in order to develop control concepts and investigate the feasibility of such control system, modelling effort has to be made to predict whether the design is worth being taken to a next step. The second phase is focused on the practical implementation of the control system and targeted to acquire a robust knowledge of the devices required to build it; the ultimate aim is to be able to perform physical tests with a preliminary configuration of the controlled micro-propulsion system.

1.2. Literature Review

The following section reports an excerpt from the extensive literature review that has preceded this thesis project. In order to develop the analytical model of the micro-valve, the fundamental equations for fluid flow are reviewed. In particular, equations, found in literature, to describe the flow within a valve are listed. In addition, although truly scarce, literature on the performance levels of closed-loop control systems for micro-propulsion subsystems has been analyzed.

1.2.1. Micro-valves Actuation Principles

Components off-the-shelf and MEMS-based valves can be categorized according to their actuation principle; the performance of the actuator is strongly related to that of the entire valve, thus a reliable comparison should be made among the end-product. Nevertheless, actuators major influence lies in response time, stroke, available force and sealing capability, hence these parameters represent a suitable set for comparison.

Electromagnetic Actuators Electro-magnetic actuated microvalves make use of the interaction between a magnetic field and a ferro-magnetic element capable to move. The magnetic field is typically generated by current-carrying wires in the form of coils. The reversed principle is also used in which Lorentz force is responsible for the movement of current-carrying wires immersed in a magnetic field (usually generated by a permanent magnet [12]. Due to current limitation of MEMS machining technique able to develop miniaturized coils with enough turnings, these devices are often coupled with external coils or permanent magnets [13], making them MEMS-hybrid valve [14].

The electromagnetically generated pressure in such actuators can be calculated as follows [15]:

$$p_{em} = \frac{M_m}{A} \int \frac{\partial H_x}{\partial x} dx \tag{1.1}$$

where A is the area of the coil, M_m the magnetization of the moving element and H_x the component of the coil-generated magnetic field in the direction of the element-motion. The response time of electro-magnetic actuators is strongly dependent on the driving electronics, nevertheless most of the developed design assure timing in the order of few milliseconds.

Electrostatic Actuators An electrostatic actuator is in principle very simple. The standard configuration consists of a fixed electrode and a movable one; when a voltage is applied the electrostatic force pulls the movable part toward the fixed one. The electro-static pressure can be determined as follows (derived from electric field density):

$$p_e = \frac{1}{2}\epsilon_0 \left(\frac{V}{d_o}\right)^2 \tag{1.2}$$

where $epsilon_0$ is the vacuum permittivity, V the voltage and d_0 the distance. The highly non-linear relation between electrodes separation and electrostatic force leads to two consequences: rather small strokes are available if relatively large pressure are needed; secondly, ”pull-in” effect occurs at a certain point preventing the actuator to fully perform proportional capability. Tang et al.[16] seems to have overcome the problem by the use of laterally driven comb drive. Another concern with such actuators is the high voltage required, which can lead to the electrolysis of some conducting species [17].

According to [14], the majority of electrostatic actuated valves are still far from being adopted in high pressure environment due to the limited electrostatic forces achievable. However, more recent developments claim to have reached higher performances in terms of maximum pressure level, for example Galambos et al. [18]. In terms of operating speed, electrostatic actuators present high performance (if resistance and capacitance are kept low) and also low power consumption in steady-state [19].

Piezoelectric Actuators Piezoelectricity is a physical phenomenon that occurs in some crystals able to generate mechanical stress or strain when subject to an applied voltage. The blocking force that a piezoelectric actuator can deliver to a external load (at maximum displacement) is [20]:

$$F_{piezo} = c_p d_{31} E_{3,max} l_0 \tag{1.3}$$

where c_p is piezo stiffness, d_{31} strain coefficient and $E_{3,max}$ is the maximum component of the electric field along the strain direction. Piezoelectric actuators provide more force at smaller deflections: normally the strain is limited to 0.1% of the original size [19]. Hence, although limited stroke is available, large forces are provided. The actuation voltage is rather high (~ 100 V [21]), comparable to that of electrostatic actuation. Both of the above-mentioned issues can be partially solved by using bimorph membrane [19] or building stack of actuators ([14],[22],[23]), in which small deflections of each element add up yielding significant stroke with much lower applied voltage (~ 25 V) and large forces unaltered. Despite high required voltage, the response time is short and the power consumption is typically very low [19][24]: accordingly, these features make them promising candidates for space applications.

Thermal-bimorph Actuators A very simple actuation principle consists in exploiting differential thermal expansion of different bonded materials. A simple equation can be derived for the deflection of two layers of equal thickness ([25],[15]):

$$\delta \sim \frac{6L^2(\alpha_2 - \alpha_1)\Delta T}{t(E_1 + E_2 + 14E_1E_2)} \tag{1.4}$$

$$p_{bm} \sim (\alpha_2 - \alpha_1)\Delta T \tag{1.5}$$

where α are the thermal expansion coefficients, E Young modulus and ΔT temperature difference. The use of such actuators yields large strokes concurrently achieving large forces for a microstructure [17]. On the other hand the response time tend to be rather slow due to the heating process that needs to take place; more, temperature changes require increased power consumption with respect to the previous alternatives. Furthermore there might be the hazard of unwanted actuation due to environmental increase in temperature [14]. According to [14], most of thermal-bimetallic valve are for gaseous media but recent designs accounted for liquid applications [26].

Thermal Volumetric Expansion Actuators Thermo-pneumatic actuation relies on thermal expansion and potential phase change of gases, liquids or even solids [27]. The volumetric thermal expansion is coupled to membrane deflection to operate the valve. The thermally generated pressure can be expressed as ([15],[25]):

$$p_{tp} = p_0 e^{\frac{-L_0}{RT}} \tag{1.6}$$

where P_0, L_0, R and T are the initial pressure, the latent heat of vaporization, gas constant and temperature, respectively. Similarly to bimetallic thermally actuated devices, response time is a bit too long for precise flow control and power consumption is large and strongly dependent upon thermal capacitance of the operating medium. Nevertheless interesting alternatives (for example the thermo-pneumatically actuated microvalve by Fitch et al. [28]) have been designed, which present improvements in power consumption and actuation time. Furthermore, especially for low-condensing point fluids, issues with these valves include their limited temperature range due to the risk of unintended actuation at high environmental temperatures.

Shape-Memory Alloy Actuators The shape memory effect is a particular transformation that occurs in some metal alloys, for instance NiTi, when subject to temperature change. In particular the effect is due to the crystalline transformation between austenite, present at high temperatures, and martensite, which prevails at low temperature. The original shape is memorized at high temperatures, then, when the alloy is cooled down, the shape can be easily deformed; if it undergoes a heating process, the alloy is shaped back to the original one. This kind of actuators allows compact structures with high blocking forces [17]. Similarly to all the thermally actuated devices, response time is significantly high due to the heating/cooling process. According to Shoji et al. [15] such actuators are not suitable for flow control and can be adopted only for on/off application; however Pemble et al. [29] presented a SMA microvalve able to control the flowrate. Another drawback is that SMA's performance degrades after thousands of cycles, which may be a critical concern in reliability of flow-control along operation time [19]. A bistable design has been presented by Barth et al. [30] that allows power saving in steady-state mode but it obstacles the implementation of proportional control capability.

Electromagnetic	Fast response time. Limited actuation voltage.	Difficult to integrate miniaturized coil.
Electrostatic	Simplicity. High speed. Low power consumption.	High voltage. Limited Forces.
Piezoelectric	Strong forces. Fast response time. Low power consumption.	Small strokes. High voltage (solved with stack layers).
Thermal-bimorph	Large strokes. Large blocking forces.	Long response time. High power consumption. Sensitive to the environment.
Thermopneumatic	Large strokes. Large blocking forces.	Long response time. High power consumption. Sensitive to the environment.
Shape Memory Alloy	Compact structures. High blocking forces.	Long response time. Difficult to implement for flow control. Degradation of performances.
Thermo actuated	Large blocking forces	Long response time.

Table 1.1: Main advantages and disadvantages for different actuation principles.

Components Off-the-shelf The existing market concerning microvalves is undoubtedly dominated by solenoid actuated devices. Constraints in size (no more than 40 mm) and actuation voltage have disregarded most of the analysed options. Major advantages in using such microvalves are certainly the fast response time, low power consumption as well as relatively low actuation voltages. Nevertheless, this design bring several drawbacks: the coil tends to be rather bulky and hardly miniaturizable yielding an overall large product; more, the blocking force is not so high, preventing the device usage for very high pressure applications.

An electro-magnetic actuated micro-valve has been chosen for the implementation of the control system, justified by the advantages mentioned above among the components off-the-shelf. A summarizing table regarding the different actuation methods for the devices found in the scientific literature is reported in Tab. 1.1.

1.2.2. Navier-Stokes Equations

The analysis of liquid flow is rather challenging since the liquid molecules exist in a state of continual collision but, except from Reynolds number, there are no parameters, such as the Knudsen number for gases, able to determine the liquid behavioral regime [31]. The two primary assumption for the majority of fluid flows are Newtonian flow and Fourier conducting fluid. The former states that the stress is directly proportional to strain rate, whereas the latter sets the proportionality between heat flow and temperature gradient. The most comprehensive set of equations governing liquid fluid flow in continuum regime are Navier-Stokes equations ([31],[32]). The following section deals with the derivation of such equations starting from Newton's second law. Furthermore, another important equation, used under the assumption of incompressible, steady, inviscid and irrotational flow, is the Bernoulli equation, whose derivation will be dealt in section 1.2.3. Considering the fluid element represented in Fig.1.1, Newton's second law can be written as:

$$\delta \mathbf{F} = \rho \delta m \mathbf{a} \tag{1.7}$$

where **F** is the vector resultant of the forces acting on the volume, ρ is the fluid density, $\delta m = \delta x \delta y \delta z$ and **a** is the resultant acceleration. Recalling that σ is the normal stress and τ the shear one, one can expand the above equation into:

$$\rho g_x + \frac{\partial \sigma_{xx}}{\partial x} + \frac{\partial \tau_{yx}}{\partial z} + \frac{\partial \tau_{zx}}{\partial z} = \rho\Big(\frac{\partial u}{\partial t} + u\frac{\partial u}{\partial x} + v\frac{\partial u}{\partial y} + w\frac{\partial u}{\partial z}\Big) \tag{1.8}$$

$$\rho g_y + \frac{\partial \tau_{xy}}{\partial x} + \frac{\partial \sigma_{yy}}{\partial z} + \frac{\partial \tau_{zy}}{\partial z} = \rho\Big(\frac{\partial v}{\partial t} + u\frac{\partial v}{\partial x} + v\frac{\partial v}{\partial y} + w\frac{\partial v}{\partial z}\Big) \tag{1.9}$$

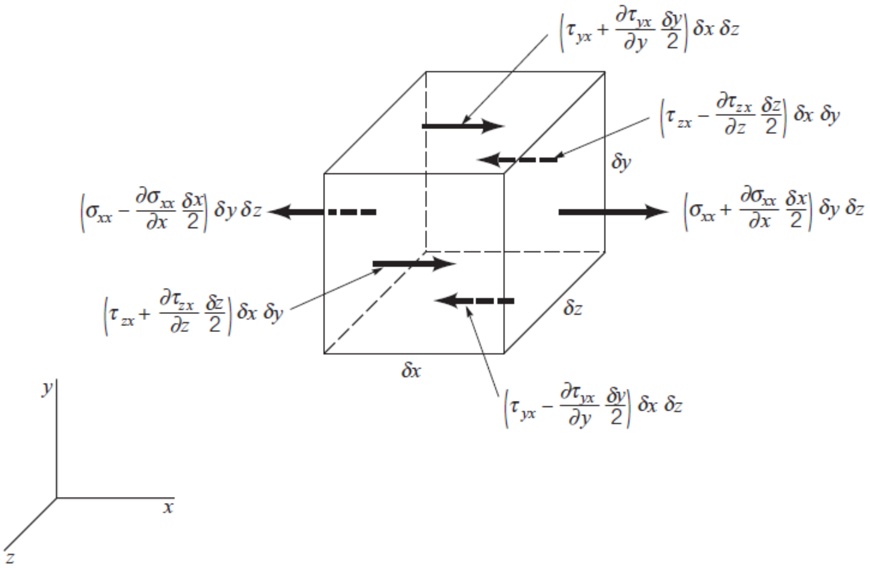

Figure 1.1: Surface forces in the x direction acting on a fluid element [1].

$$\rho g_z + \frac{\partial \tau_{xz}}{\partial x} + \frac{\partial \tau_{yz}}{\partial z} + \frac{\partial \sigma_{zz}}{\partial z} = \rho\left(\frac{\partial w}{\partial t} + u\frac{\partial w}{\partial x} + v\frac{\partial w}{\partial y} + w\frac{\partial w}{\partial z}\right) \tag{1.10}$$

where the volume contribution $\delta x \delta y \delta z$ cancels out; u, v, w are the x, y, z component of the velocity respectively. The above equations are the general differential equations for any continuum in motion or at rest. The above equations are not solvable (more unknowns than equations), unless additional information about the stresses are given. In particular, it is necessary to establish a relationship between the stresses and velocities. In the assumption of **viscous**, **incompressible**, **Newtonian** flow, it is known that the stresses are linearly related to the rates of deformation [1] and can be expressed in Cartesian coordinates as:

$$\sigma_{xx} = -p + 2\mu\frac{\partial u}{\partial x} \tag{1.11}$$

$$\sigma_{yy} = -p + 2\mu\frac{\partial v}{\partial y} \tag{1.12}$$

$$\sigma_{zz} = -p + 2\mu\frac{\partial w}{\partial z} \tag{1.13}$$

for the normal stresses and as follows for shearing stresses:

$$\tau_{xy} = \tau_{yx} = \mu\left(\frac{\partial u}{\partial y} + \frac{\partial v}{\partial x}\right) \tag{1.14}$$

$$\tau_{yz} = \tau_{zy} = \mu\left(\frac{\partial v}{\partial z} + \frac{\partial w}{\partial y}\right) \tag{1.15}$$

$$\tau_{zx} = \tau_{xz} = \mu\left(\frac{\partial w}{\partial x} + \frac{\partial u}{\partial z}\right) \tag{1.16}$$

where p is the pressure, the negative of the average of the three normal stresses, namely $p = \frac{1}{3}(\sigma_{xx} + \sigma_{yy} + \sigma_{zz})$ [1]. If the stresses are now substituted in the equations of motion, the well-known Navier-Stokes equation are obtained:

$$-\frac{\partial p}{\partial x} + \rho g_x + \mu\left(\frac{\partial^2 u}{\partial x^2} + \frac{\partial^2 u}{\partial y^2} + \frac{\partial^2 u}{\partial z^2}\right) = \rho\left(\frac{\partial u}{\partial t} + u\frac{\partial u}{\partial x} + v\frac{\partial u}{\partial y} + w\frac{\partial u}{\partial z}\right) \tag{1.17}$$

$$-\frac{\partial p}{\partial y} + \rho g_y + \mu\left(\frac{\partial^2 v}{\partial x^2} + \frac{\partial^2 v}{\partial y^2} + \frac{\partial^2 v}{\partial z^2}\right) = \rho\left(\frac{\partial v}{\partial t} + u\frac{\partial v}{\partial x} + v\frac{\partial v}{\partial y} + w\frac{\partial v}{\partial z}\right) \tag{1.18}$$

$$-\frac{\partial p}{\partial z}+\rho g_z+\mu\Big(\frac{\partial^2 w}{\partial x^2}+\frac{\partial^2 w}{\partial y^2}+\frac{\partial^2 w}{\partial z^2}\Big)=\rho\Big(\frac{\partial w}{\partial t}+u\frac{\partial w}{\partial x}+v\frac{\partial w}{\partial y}+w\frac{\partial w}{\partial z}\Big) \tag{1.19}$$

The above Navier-Stokes equation for the dynamics can be coupled with the well-known continuity equation. The last equation, namely the energy equation, can be derived from the first law of thermodynamics. Nevertheless, such equation is not used throughout this research work, thus its derivation is not presented and the final form is given as reference. The compact forms of the conservation laws are:

$$\frac{\partial \rho}{\partial t}+\nabla\cdot(\rho\mathbf{u})=0 \tag{1.20}$$

$$\rho\Big(\frac{\partial \mathbf{u}}{\partial t}+\mathbf{u}\cdot\nabla\mathbf{u}\Big)=-\nabla p+\nabla\cdot\tau+\mathbf{f} \tag{1.21}$$

$$\rho c_v\Big(\frac{\partial T}{\partial t}+T\cdot\nabla T\Big)=\ -p\nabla\cdot\mathbf{u}+\nabla\cdot(k\nabla T)+\tau\cdot\nabla\mathbf{u} \tag{1.22}$$

where ρ is the density, t is the time, **u** is the fluid field velocity, p is the pressure, τ is the viscous stress tensor, **f** is the resultant of external forces acting on the control volume, T is the temperature and c_v is the specific heat at constant volume. The above equations are also known as continuity, momentum and energy equations respectively.

1.2.3. Bernoulli equation

Recalling the equations of motion for a fluid element 1.8, 1.9 and 1.10, the assumptions of irrotational, inviscid, steady and incompressible can be applied.

- the **irrotational** assumption:

  $$\nabla\times\mathbf{u}=0 \tag{1.23}$$

  make the crossed-derivatives vanish.
- the **inviscid** assumption $\mu=0$ leads to null shear stresses
- the steady-state flow implies the cancellation of all time derivative
- incompressible flow refers to the condition in which material density is constant within a fluid element

in the compact form, assuming the body force is solely due to gravity, the equations can be re-written as:

$$\rho\Big(\mathbf{u}\cdot\nabla\mathbf{u}\Big)=-\nabla p+\rho\mathbf{g} \tag{1.24}$$

Integrating the above equation along a streamline, the following is obtained:

$$\frac{\partial}{\partial s}\Big(\frac{u^2}{2}+\frac{p}{\rho}+gz\Big)=0\rightarrow\frac{u^2}{2}+\frac{p}{\rho}+gz=const. \tag{1.25}$$

which is the so-called Bernoulli equation. Note that in the last equation, g has replaced the vectorial form and stands for absolute value of gravity acceleration.

1.2.4. Analytical Models for the Flow within Microvalves

The direct simulation of the flow within microvalves by solving Navier-Stokes equation is not feasible due to complicated geometries, moving boundaries and peculiar unsteadiness of the flow [2]. Moreover, microvalves are the most dissipative element in any fluid system, hence an accurate estimation of head losses are required for reliable models. However, one common approach ([33], [34], [35], [36]) is to approximate microvalves as variable area orifices, in which inertial losses are dominating the process:

$$\Delta p\propto Q^2 \tag{1.26}$$

where p is the fluid pressure and Q is the volumetric flowrate. An important parameter when dealing with this modelling strategy is the *discharge coefficient* C_d, defined as:

$$C_d = \frac{1}{\sqrt{\zeta}} = \sqrt{\frac{1}{2}\frac{\rho u^2}{\Delta p}} \tag{1.27}$$

where

$$\zeta = \frac{\Delta p}{\frac{1}{2}\rho u^2} \tag{1.28}$$

is the loss coefficient [2]. Using the above parameters, the valve outflow rate Q can be calculated as:

$$Q = C_d A \sqrt{\frac{2\Delta p}{\rho}} \tag{1.29}$$

These models give, however, little insight to the flow sensitivity to valve geometry and Reynolds number and require experimental validation and/or numerical simulations for characteristic discharge coefficients. An order-of-magnitude model has been developed by Benignos [2] in which the loss coefficient is estimated using geometrical parameters only. The analyzed configuration (see Fig.1.2) is nicely adherent to those typical of MEMS-based microvalves, thus it is of strong interest for the purpose of this work. According to Benignos, the loss coefficient in the geometry represented in Fig.1.2 is:

$$\zeta = \frac{\Delta p}{\frac{1}{2}\rho u^2} = \frac{1}{2}\left(1 - \frac{A_0}{A1}\right)^{\frac{3}{4}} + \left(1 - \frac{A_0}{A2}\right)^2 \tag{1.30}$$

However the above strategy does not leave room for any transient analysis, which is critical for an accurate control process. An interesting approach has been used by Smal et al. [3] in fluidic modelling of a microvalve. The device has been divided into several *sectors* and analyzed according to different assumptions, being cylindrical channel, Bernoulli equation for pressure drop due to fluid deviation and flow between parallel disks as seen in Fig.1.3. In this research the flow in the restriction sector, the only part truly affected by the control-actuation, is modeled as a fluid flow between two parallel disks. Smal et al. neglected the unsteady-term in the derivation of the average velocity, however, it is not prohibitive to include it in a further analysis.

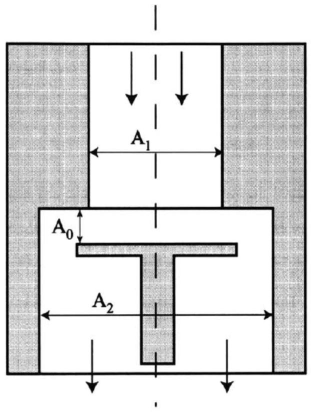

Figure 1.2: Valve schematic for the order-of-magnitude model in [2].

Another interesting, and often very effective, approach of fluid modelling in microvalves consists in the so called **lumped parameter** reduction, based on electric circuit analogy [37]. Due to the importance of such method, a brief summary paragraph is reserved below to explain better the electric analogy.

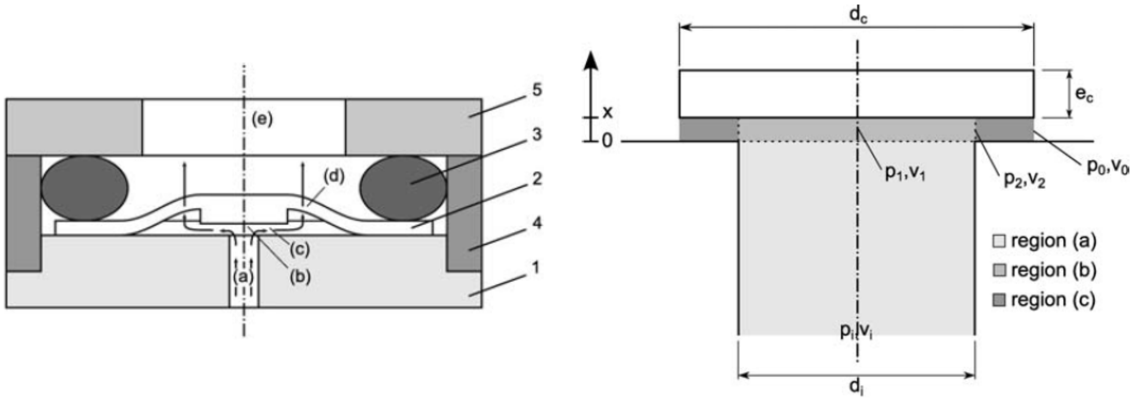

Figure 1.3: Valve sectors for fluidic analytical modelling [3].

Microfluidics Network using Electric circuit Analogy The application of circuit methods to microfluidic is based on the analogous behaviour of hydraulic and electric circuits [37]. In fluid mechanics, the pressure-driven flow through an infinitely long circular channel is described by the Hagen-Poiseuille law, which relates the pressure drop with the consequent volumetric flowrate across the channel. Similarly, Ohm's law relates the voltage drop with the current intensity through an ohmic electric conductor. From such analogy, one can deduce that pressure drop and voltage drop, hydraulic resistance and electric resistance, volumetric flowrate and electric current are somehow related, within the context of this approach. One key limitation of the analogy is that the flow must be **laminar**, **viscous** and **incompressible**. Furthermore, the electric circuit methods are not able to provide any transient results, nor do they provide information on the spatial distribution of fluid properties [37]. Let's consider again Eq.1.21, in the steady state of the fully developed flow, the time derivatives of the variables vanish and a perfect balance between pressure forces and viscous ones is set:

$$\nabla p = \mu \nabla^2 \mathbf{u} \tag{1.31}$$

applying the boundary conditions, namely u=0 when r=R (channel's radius), recalling that in the steady state of fully developed laminar flow the velocity field is unidirectional [37] and finally integrating:

$$u = \frac{R^2 - r^2}{4\mu}\Big(-\frac{dp}{dx}\Big) \tag{1.32}$$

which describes the parabolic profile of the velocity field throughout the cylindrical channel. The above flow is usually referred to as Poiseuile flow. In order to obtain the volumetric flowrate, the expression for the velocity field needs to be integrated on the cross-sectional area. Hence the volumetric flowrate can be expressed as:

$$Q = \frac{\pi R^4}{8\mu}\Big(-\frac{dp}{dx}\Big) \tag{1.33}$$

Eq.1.33 is commonly referred to as Hagen-Poiseuille's law. In principle, eq. 1.33 is only valid for a straight and infinitely long cylindrical channel [37]. Nevertheless, if the assumption that the pressure gradient is constant throughout a channel of finite length L, then equation 1.33 can be written as:

$$Q = \frac{\pi R^4}{8\mu}\frac{\Delta p}{L} \tag{1.34}$$

which is inherently analogous to the electric Ohm's law. Indeed, eq. 1.34 can be transformed into a compact form:

$$Q = \frac{\Delta p}{R_h}$$

where R_h is the hydraulic resistance, or more explicitly,

$$\Delta p = Q \cdot R_h$$

which resembles the famous Ohm's law $V = I \cdot R$ in which V is the voltage, I the current and R the electric resistance. Along the Ohm's law, several other features typical of circuit analysis are valid in microfluidics network. The application of circuit methods to microfluidics is based on the analogous behaviour of hydraulic and electric circuits with correlations of pressure to voltage, volumetric flow rate to current, and hydraulic to electric resistance. This type of analysis enables fast preliminary assessment of the behaviour of fluid flow and, above all, it linearizes the relationship between pressure drop and volumetric flow rate under certain assumptions. Namely:

$$\Delta p = R \cdot Q$$

Microvalves can be regarded solely as dissipative devices, hence their equivalent element are electric resistors. However, the assessment of the value of hydraulic resistance depends strongly on the assumption made in the type of flow within the microvalve (e.g. annular flow, flow between two infinite plates etc.). Carrozza et al. [4] assumed the flow through the needle microvalve as a variable area annular flow, in which the internal radius is to be controlled. This strategy led to an expression of the conductivity of the microvalve of:

$$\frac{1}{R} = \frac{\pi}{8\mu L} r_2^4 \left[1 - r_1^4 + \frac{(1-r^2)^2}{ln(r)} \right] \tag{1.35}$$

where with reference to Fig. 1.4 r_1 is the internal radius of the annular conduit, depending on the axial position y of the shutter, r_2 the external radius of the annular conduit, equal to the internal radius of the hollow frame, r = r_1/r_2 the function of the shutter axial position y, L the length of the conduit, and μ the dynamic viscosity of the fluid.

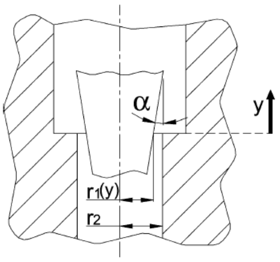

Figure 1.4: Geometric parameters required to calculate the equivalent resistance [4].

A similar approach has been used by Galambos et al. ([38],[18]) considering the flow being radial between two closely spaced parallel disks, i.e., the lid cover seat and the valve boss. The relationship they presented is:

$$Q = \frac{\pi h^3 \Delta p}{6\mu \; ln(\frac{R}{r})} \tag{1.36}$$

where R is the outer radius, r is the inner one and h is the gap height. Nevertheless, this approach as the previous one does not take into account the unsteady behaviour of the system. When the fluid flow is set stable, this might not be a big concern in performance prediction, whereas it is likely to have tremendous consequences whenever quick operations (fast on-off transition) need to be analyzed, as in micropropulsion application.

1.2.5. Ideal Rocket Equation for Thrust Estimation

The thrust within a rocket engine (same principle as microthruster) is generated by the rate of change of momentum associated with the exit velocity of the propellant flow and the differential pressure at the exit point with respect to the surrounding [39], [40]. The flow undergoes several different processes in the chamber, depending on the type of device used, namely combustion reactions (traditional engines), heating (VLM) or simply gas flow accelerated by geometric shape. The thrust is calculate as:

$$F = \dot{m} \cdot u_{exit} + (p_{exit} - p_{atm}) \cdot A_{exit} \tag{1.37}$$

where F is the thrust, $\dot{m}$ the mass flow rate, u_{exit} the exhaust velocity, p_{exit} and p_{atm} are the exit and atmospheric pressure respectively, A_{exit} is the exit area. In order to calculate pressure and velocity at nozzle outlet, an isentropic expansion is considered[40]. Note that for this derivation it is assumed that the fluid flowing through the nozzle is fully evaporated, in other words in gaseous state, and can be described using the ideal gas law [41]. Applying the energy balance to the gases flowing through the nozzle under isentropic assumption, neglecting storage term and potential energy change, the following expression is obtained:

$$h + \frac{1}{2}u^2 = h_{tot} = const. \tag{1.38}$$

where h is the specific enthalpy, which for an ideal gas can be re-written as:

$$c_pT + \frac{1}{2} = c_pT_c + \frac{1}{2}u_c = c_pT_{tot} \tag{1.39}$$

where c subscript refers to the chamber. If the velocity inside the chamber is considered negligible (stagnation condition), Eq.1.39 may turn into:

$$T_c = T + \frac{u^2}{2c_p} \rightarrow u = \sqrt{2 \cdot c_p \cdot (T_c - T)} \tag{1.40}$$

As isentropic flow is assumed, Poisson relations hold:

$$\left(\frac{T}{T_c}\right) = \left(\frac{p}{p_c}\right)^{\frac{\gamma-1}{\gamma}} = \left(\frac{\rho}{\rho_c}\right)^{\gamma-1} \tag{1.41}$$

where $\gamma = \frac{c_p}{c_v}$. Using Eq.1.40 and Eq.1.41, the exhaust velocity can be written as [40]:

$$u_{exit} = \sqrt{2 \cdot \frac{\gamma}{\gamma-1}\frac{R_a}{M} \cdot T_c\left(1 - \left(\frac{p_e}{p_c}\right)^{\frac{\gamma-1}{\gamma}}\right)} \tag{1.42}$$

where T_c is chamber temperature, R_a the universal gas constant, M the mean molar mass, γ specific heat ratio and p_c is the chamber pressure. The expression for the critical mass flow rate through the nozzle at which the nozzle flow becomes supersonic is:

$$\dot{m} = \frac{\Gamma \cdot p_c \cdot A_t}{\sqrt{R \cdot T_c}} \tag{1.43}$$

where A_t is the throat area and $\Gamma = \sqrt{\gamma} \cdot \left(\frac{2}{\gamma+1}\right)^{\frac{\gamma+1}{2(\gamma-1)}}$ is the Vandenkerckhove function.

For a convergent-divergent nozzle, the pressure ratio $\left(\frac{p_e}{p_c}\right)$ and the nozzle expansion ratio $\left(\frac{A_e}{A_t}\right)$ are related as follows [40]:

$$\frac{A_e}{A_t} = \frac{\Gamma}{\sqrt{2 \cdot \frac{\gamma}{\gamma-1}\left(\frac{p_e}{p_c}\right)^{\frac{2}{\gamma}}\left(1 - \left(\frac{p_e}{p_c}\right)^{\frac{\gamma-1}{\gamma}}\right)}} \tag{1.44}$$

The above derivation is based on one-dimensional fluid flow through the nozzle [39]. It can be easily seen that the thrust can be predicted if chamber conditions (T_c, p_c) are known as well as geometrical properties of the throat-nozzle configuration (A_t,A_e). Obviously propellant properties need to be known and the same holds for the atmospheric pressure in the location where the thruster is working.

1.2.6. Vaporizing Liquid Micro-Resistojet

The VLM-Vaporizing Liquid microthruster is a micromachined chamber which is heated by internal or external microheater to vaporize a liquid flow; the vapor flow is then ejected through a nozzle, producing thrust. Modelling the flow within the VLM may become truly complicated, due to the presence of two-phase flow. According to [41], most, if not all, of the authors neglect this physical phenomenon and just analyze single-phase flow. A schematic of the device is shown in Fig. 1.5.

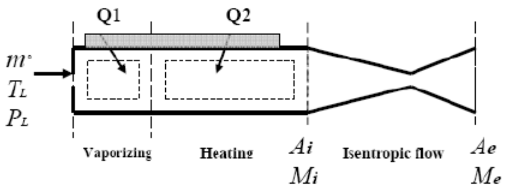

Figure 1.5: Schematic diagram of the VLM used in [5].

1.2.7. Fluidic Components for Thrust Control

Regardless of the applications, the main constituents of digital control loop are sensors, electronic-processing unit and actuators. The usual work-flow consists in the determination of the control variable by using the set of sensors; such measurement is then used, sometimes pre-processed, and compared with the commanded value in the processing unit. Finally the output of the processing unit controls the actuator in a way that the commanded value is as close as possible to the actual one. An important feature is the algorithm used to process the sensor signal to obtain the actuation command. The most widely used control-technique is the linear *PID controllers*; nevertheless, more sophisticated approaches are available to deal with system nonlinearities, such as the Nonlinear Dynamic Inversion (NDI). Rangsten et al. ([42],[43]) presented a very interesting design for a closed-loop thrust control for a MEMS-based cold gas microthruster, which comprises the following main components:

- ON/OFF normally-closed solenoid valve for pulse mode operation
- MEMS proportional flow control valve
- MEMS mass flow sensor
- MEMS chamber and nozzle
- Heaters and temperature sensors
- Front-end electronics to read mass flow sensor signal

The task of continuous thrust regulation in the range from zero to maximum level is accomplished by using the proportional flow control valve ([42],[44]). Real-time measurements from the mass flow-sensor are processed in the feedback path to determine the required actuation within the valve.

An important hint in designing such integrated system is reported by Kvell et al. [44]: to obtain a short response time, the internal volume needs to be reduced as much as possible. To this purpose, the strategy of a fully chip-integrated microthruster (valve/chamber and nozzle at least) seems to be the most performing one [44]. Nevertheless the complete propulsion module is suitable for Cubesat integration, hence its size exceed the dimension that this research and the future work will pursue.

1.2.8. Current Results and Performance Level

In order to acquire knowledge and sensitivity on the performance level of closed-loop thrust control systems, here results from literature are presented and evaluated in light of what has been discussed throughout the previous analysis. The most significant parameters to assess the performance of a controlled system are the thrust range, step response and the related impulse-response time and finally the thrust resolution.

Thrust range The thrust range is the operating limits in which the thruster can work. The most straightforward experimental approach to assess such range is to use the proportional valve as a simple ON/OFF valve, or if an isolation valve is present, to open the entire path. The challenging aspect of the optimization process of the thrust range lies in the adaptability of the system (valve - flow sensor - thruster itself) to a large range of operation, regarding mass flow rate, pressure and many other varying parameters, keeping response time and overshoot, and other control parameters, within given requirements. Rangsten et al. [42] and Matticari et al. [10] both claim a thrust range of over 3 order of magnitude, namely 1/650 μN for the former and 1/500 μN for the latter.

Step response and impulse-response time A step response is the behaviour of the system to a sudden non-null commanded input. The response time at a thruster level for the design of Rangsten ([42],[43]) is around 500 ms, whereas Matticari et al.[9] state that the response time to achieve 63% of commanded thrust is below 300 ms. Again, in this discussion the importance of a fast response time of all the components integrated in the system is underlined.

Thrust resolution Thrust resolution is the minimum commanded-thrust variation that produces an observable change in the output thrust. To perform delicate orbital or attitude maneuvers a high accuracy is needed, therefore a sophisticated closed-loop controlled propulsion system needs to achieve a very high thrust resolution, enabling the spacecraft to make very fine corrections. A high resolution is achieved by high manufacturing accuracy in the actuators as well as a fine sensitivity in the sensors. According to the literature ([42],[43],[9],[10]) thrust resolution below 1 μN are achievable.

1.3. Thesis Outline

The thesis report is divided into three main chapters. Hereby, a description of its outline is given to help the reader to retrieve relevant information.

- **Chapter** 2 deals with all the theoretical software-based analysis that have been performed. The chapter starts with the derivation of the analytical model to describe the dynamics of a electromagnetic solenoid actuated micro-valve. A novel approach to treat the fluid flow within the valve is derived and integrated to the set of equations describing the dynamics. A numerical model is then developed using the simulation software COMSOL Multiphysics. All the domains, namely fluid-mechanical-electromagnetic, are integrated in the same model and their interaction is simulated. The results delivered by the analytical and numerical model are compared and discussed.

  A sensitivity analysis is performed on the analytical model to assess the influence of each parameter on the output of the system. The adopted approach is the global sensitivity analysis, where the parameters are varied stochastically with a uniform distribution. This allows a more meaningful analysis with much less sample points with respect to the classic gridded parameters distribution.

  The control concepts are developed using the derived analytical model. A frequency analysis is performed to determine the suitable actuation frequency the PWM signal. The continuous PID control is presented and the strategy to determine the best-performing gains is described. The discontinuous SMC control is also developed and a modified-SMC control is derived based on insights from the experimental tests.

  Finally the analytical models for the main components of the micro-propulsion system, namely the propellant tank, the micro-valve and the VLM thruster, are combined into the comprehensive model. The simulation results for the complete system, with and without the control scheme, are presented and discussed in light of the considerations made throughout the chapter.

- **Chapter** 3 deals with the experimental part of the work, in which most of the showcases analyzed in the previous chapter are reproduced in the laboratory. The validation of the analytical model is done by characterizing the available ON/OFF solenoid valve. The characterization is performed both to determine the discharge coefficient of the valve and, most importantly, the behaviour for different duty cycle and PWM frequencies. A strategy to measure the mass flowrate out of the valve from the depressurization of the tank is developed and adopted in the tests of the closed-loop control system. The closed-loop control to regulate the output flowrate of the valve is tested and the results are analyzed in light of a potential integration with the complete system.

  Finally, the complete system comprising the propellant tank, the micro-valve, the VLM device and the required electronics is tested in blowdown mode. First, the uncontrolled configuration has been tested, to which the closed-loop control system has later been integrated. The results of the different tests are analyzed in terms of typical control parameters, such as response time, steady-state error and output resolution.

- **Chapter** 4 is a conclusive section where the results are summed up and compared. The first section presents the comparison between the experimental results and the simulated ones. The last section summarize the main achievements of the presented work and lists the recommendation for the follow-up research projects.

2

Modelling and Simulations

The development of a control system, of whichever nature, starts from the mathematical characterization of the dynamic behaviour of the process [8]. The equations to simulate the behaviour of the system represent the baseline for the development of the control concepts, such as the frequency analysis and the design of the control scheme itself. The analytical model, which is based on several assumptions, has to be validated with the aid of more sophisticated tools, such as numerical simulations. Since the the actuation and flow establishment takes place in the micro-valve, such device is the central key-point of the analysis. The solenoid-actuated electromagnetic micro-valves make use of electromagnetic field induced by a current-carrying coil to move a plunger. Several different physics are inherently involved in the aforementioned process, thus COMSOL Multiphysics has been chosen to perform the numerical simulations due to its high suitability in solving problems with different interfacing physics.

The following chapter is structured in several sections: section 2.1 describes the equations that build up the analytical state-space model, whereas section 2.2 presents the critical concepts and key settings for the numerical simulation. Section 2.3 deals with the comparison between the two different modeling approaches. Section 2.5 presents the design of the controllers, both PID based on PWM duty cycle and Sliding Mode Control (SMC). Section 2.6 shows the results of the simulation of the complete model, with and without the closed-loop control system. Finally, section 2.7 summaries the findings of the chapter.

2.1. Analytical Model

The analytical model is a mathematical representation of the the behaviour of the system. It is necessary to run simulations and develop control concepts without performing time-consuming experiments. Furthermore, a generic analytical model, namely regardless of the particular chosen device, is a very useful tool for design purposes since it provides preliminary results on the effectiveness of different design strategies. Future plans at TU Delft potentially concern the realization of a miniaturized micro-valve for micro-propulsion purposes, thus the effort put in the development of an accurate, but easy to adjust in the meantime, is more than justified.

The analytical model serves as a state-space representation of the dynamics of the system given a certain input. As already mentioned, there are several non homogeneous physical processes occurring in the actuation of a valve. When the actuation voltage is delivered to the valve coil, an electromagnetic interaction occurs between the coil and the moving plunger; the plunger is then set into motion subject to the electromagnetic force generated by the above-mentioned interaction, the fluid force pushing from the inlet, the elastic spring counteracting force and the inherent viscous damping force. Finally, the fluid flow is established as soon as the valve starts opening. Given the above description, it is possible to group the processes into three different domains:

1. Electromagnetic
2. Fluid

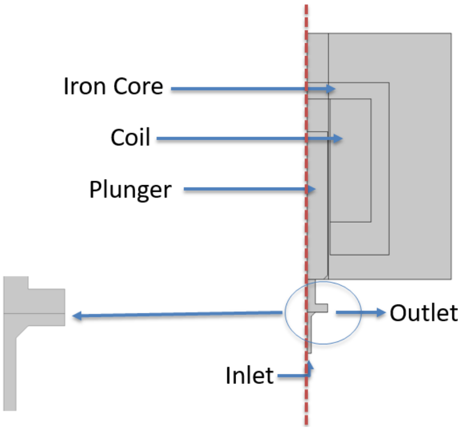

Figure 2.1: Schematics of the micro-valve geometry used to develop the analytical model. Radial symmetry is exploited.

3. Mechanical

Mathematical modeling and control of solenoid-operated valves is reported by few researchers. Furthermore, most of the models make use of hybrid analytical-empirical models and, above all, they neglect the transient fluid flow establishment as part of the dynamic of the system [45]. In the following sections, every domain is described and analyzed in detail.

2.1.1. Geometry Definition

The geometry definition is kept as simple as possible to be representative of the physical processes rather than of particular design configurations. The solenoid-actuated micro-valve is operated by energizing a coil, which in turns set into motion a plunger in direct contact with the flow. The fluid flow is usually squeezed by an adjustable valve cap, actuated by the plunger.

The geometry has been schematized as in Fig. 2.1, based on an extended literature survey of existing components off-the-shelf.

Fig. 2.1 inherently shows all the components, whose physics will be treated in the analytical model, namely the inlet-outlet fluid flow, the moving plunger and the electromagnetic circuit established through the coil.

2.1.2. Electromagnetic Domain

The internal coil of a solenoid-actuated valve is connected to an external actuating circuit. Fig. 2.2 shows a simple representation of the electromagnetic circuit.

When the coil is energized the current *i* starts flowing through the coil. The time-dependent behaviour of the current *i* is ruled by a simple Kirchoff's voltage law (KVL) that can be expressed as according to [46]:

$$v = Ri + \frac{d\lambda}{dt} \tag{2.1}$$

where v is the applied voltage, R is the coil resistance and $\lambda(x, i)$ is the flux linkage, defined as $N\Phi$, where Φ is the magnetic flux. In order to determine an expression for the flux linkage, a simple representation of the magnetic circuit is used. If the solenoid is considered to be operating in the linear region, the flux linkage, with reference to Fig. 2.2, can be expressed as follows according to [46]:

$$Ni = \Phi \mathrm{P} \tag{2.2}$$

where P is the magnetic reluctance of the system. Eq. 2.2 can be further developed in:

$$Ni = \Phi\left(\frac{d_{g0} - x}{\mu_0 A_{sol}} + \frac{g}{\mu_0 \pi d_{sol} a}\right) \tag{2.3}$$

where *Ni* is the so-called magneto-motive force, which is the product between number of coil turns and electric current, μ_0 is the magnetic permeability of air, A_{sol} and d_{sol} are solenoid cross-sectional

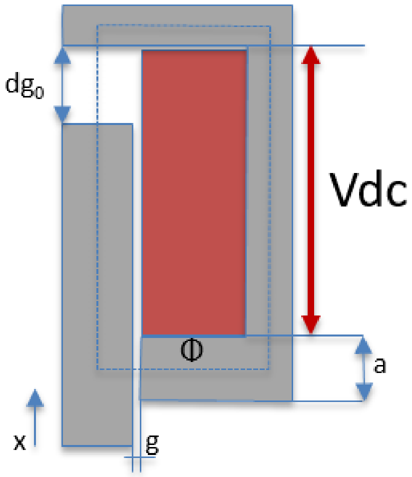

Figure 2.2: Simple representation of the electromagnetic circuit and interaction between coil and moving plunger.

area and diameter respectively. It is important to note that only air gaps reluctances, namely the one on top of the plunger and the one on its side, have been considered in Eq. 2.3, since the reluctance of the metal structure is negligible compared to them. According to the above considerations, the flux linkage can be expressed as follows according to [46]:

$$\lambda(x,i) = \frac{N^2 \mu_0 A_{sol} a}{a(d_{g0} - x) + \frac{d_{sol} g}{4}} i \tag{2.4}$$

If Eq. 2.1 is manipulated, the differential equation describing current behaviour in time can be derived:

$$v = Ri + \frac{\partial \lambda}{\partial i}\frac{di}{dt} + \frac{\partial \lambda}{\partial x}\frac{dx}{dt} \tag{2.5}$$

The first term is the resistive voltage drop, the second is the inductive voltage due to the change in current and the last one is representative of the motion of the plunger, which is also known as *back electromagnetic-force* or *motion electromagnetic-force* [45]. The partial derivative of the flux linkage with respect to the current is nothing more than the inductance $L(x)$ of the system, dependent on the position *x* of the plunger [45] [46]. Hence, Eq. 2.5 can be finally written as:

$$\frac{di}{dt} = \frac{1}{L(x)}\Big(v - i\Big(R + \frac{dx}{dt}\frac{dL(x)}{dt}\Big)\Big) \tag{2.6}$$

Eq. 2.6 represents the state-space representation of electric current dynamics, for a given input voltage. The electromagnetic circuit analysis is helpful in determining the time-dependent behaviour of the electric current. Nevertheless, the magnetic flux, which is established when the coil is energized, generates a force on the plunger. The magnetic force can be calculated from the co-energy, which can be expressed as the integral of the flux linkage against the current according to [45][46]:

$$F_{mag} = \frac{\partial W'(x,i)}{\partial x} = \frac{\partial}{\partial x}\int_0^i \lambda(x,i)di = \frac{\partial}{\partial x}\Big(\frac{L(x)}{2}i^2\Big) = \frac{i^2}{2}\frac{N^2 \mu_0 A_{sol} a^2}{(a(d_{g0} - x) + \frac{d_{sol} g}{4})^2} \tag{2.7}$$

where i is the electric current, N number of coil turns, A_{sol} the solenoid cross-sectional area, a is the side iron strips length with reference to Fig. 2.2, d_{g0} is the initial top air gap.

2.1.3. Fluid Domain

The fluid flow is established as soon as the valve is actuated. With respect to the simplified geometry selected in this work, the valve could be regarded as a variable orifice, where its area depends on the position of the plunger. The pressurized fluid flow at the inlet pushes against the plunger in turn, exerting a coupled static and dynamic force on it.

The most common approach to describe the flowrate through a valve is to use the *orifice equation*, described again in the next paragraph to stress its importance. Nevertheless, if Eq. 2.11 is analyzed in detail, it is rather straightforward to realize that the fluid flow behaviour is proportional to the plunger displacement. This means that there is no additional dynamics in the flow establishment for a given plunger motion or, in other words, that the fluid flow follows the time-dependent behavior of the plunger, which is set into motion. Neglecting the transient behaviour of the fluid flow could be a valid approach if the focus is indeed on the steady-state behaviour of the system. Whereas, to develop a good model for control purposes, the transient description of the flow establishment needs to be described. According to the above considerations the fluid flow is described in two different ways: one using solely the *orifice equation* and the other in which transient equations are derived to come up with a valid differential equation.

Orifice Equation The direct simulation of the flow within micro-valves by solving Navier-Stokes equation is not feasible due to complicated geometries, moving boundaries and peculiar unsteadiness of the flow [2]. Moreover, micro-valves are the most dissipative element in any fluid system, hence an accurate estimation of head losses are required for reliable models. However, one common approach ([33], [34], [35], [36]) is to approximate micro-valves as variable area orifices, in which inertial losses are dominating the process:

$$\Delta p \propto Q^2 \tag{2.8}$$

where p is the fluid pressure and Q is the volumetric flowrate. An important parameter when dealing with this modelling strategy is the *discharge coefficient* C_d, defined as:

$$C_d = \frac{1}{\sqrt{\zeta}} = \sqrt{\frac{1}{2}\frac{\rho u^2}{\Delta p}} \tag{2.9}$$

where

$$\zeta = \frac{\Delta p}{\frac{1}{2}\rho u^2} \tag{2.10}$$

is the loss coefficient [2]. The volumetric flowrate Q can be expressed using the *orifice equation*:

$$Q = C_d A_{out}\sqrt{\frac{2\Delta p}{\rho}} \tag{2.11}$$

where C_d is the discharge coefficient, which is based on empirical calculation or given by the device's manufacturer. As already mentioned the outlet area is linearly related to the plunger displacement, see Fig. 2.3.

As already mentioned, these models give, however, little insight to the flow sensitivity to valve geometry and Reynolds number and require experimental validation and/or numerical simulations for characteristic discharge coefficients.

Transient Modelling of Fluid Flow between two Infinite Parallel Plates Smal et al. [3] made the assumption of fluid flow between two parallel plates to model the behaviour within the region of squeezed flow (valve seat-plunger). However, the authors neglected the unsteady term, preventing the model to be suitable for modelling transient state. In the parallel-plates approximation the pressure drop across the valve has to be modelled separately as an abrupt geometrical change, see Fig.2.4.

In Fig.2.4 a schematic of fluid parameters for the derivation is shown. The fluid is considered **incompressible**, **isothermal** and **unidirectional** as in [32].

The continuity equation becomes:

$$\nabla \cdot \mathbf{u} = 0 \rightarrow \frac{\partial u}{\partial x} + \frac{\partial v}{\partial y} + \frac{\partial w}{\partial z} = 0 \tag{2.12}$$

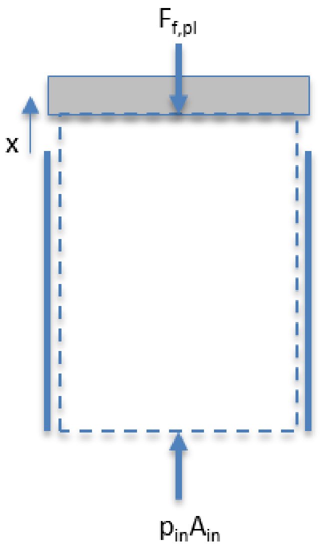

Figure 2.3: Schematics of the fluid domain.

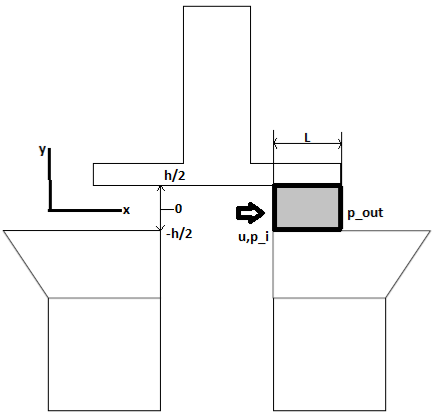

Figure 2.4: Simplified geometry for modelling transient phase within a micro-valve. The flow is assumed to occur between two infinite parallel plates.

where u, v, w are x, y, z component of the velocity field respectively. Assuming unidirectional flow means setting v=w=0. Then the continuity equation becomes:

$$\frac{\partial u}{\partial x} = 0 \tag{2.13}$$

Since the two plates are considered infinitely extended, the velocity u is not a function of z. Thus, the velocity field is solely a function of y, namely u=f(y). The x-component of Navier-Stokes momentum equation (eq. 1.21) can be written as: [1]:

$$\rho\frac{\partial u}{\partial t} = -\frac{\partial p}{\partial x} + \mu\frac{\partial^2 u}{\partial y^2} \tag{2.14}$$

Using the same approach as in the previous section, the pressure term can be transformed in the same fashion:

$$\frac{\partial p}{\partial x} = C_1$$

$$P = C_1 x + C_2$$

then, setting the following boundary conditions:

$$\begin{cases} x = 0 \rightarrow p = p_{in} \rightarrow C_2 = p_{in} \\ x = L \rightarrow p = p_{out} \rightarrow C_1 = \frac{p_{out} - p_{in}}{L} \end{cases}$$

Consequently eq. 2.14 becomes:

$$\rho \frac{\partial u}{\partial t} = \frac{\Delta p}{L} + \mu \frac{\partial^2 u}{\partial y^2} \tag{2.15}$$

Integrating eq. 2.15 twice over *y*:

$$\frac{\rho y^2}{2\mu} \frac{\partial u}{\partial t} = \frac{y^2}{2\mu} \frac{\Delta p}{L} + u + C_3 y + C_4 \tag{2.16}$$

To determine the two constants C_3 and C_4, the following boundary conditions are applied [1] (*no-slip* flow at both walls would produce the same results):

$$\begin{cases} \frac{\partial u}{\partial y}\rvert_{y=0} = 0 \\ u\rvert_{y=h/2} = 0 \end{cases} \tag{2.17}$$

$$\begin{cases} C_3 = 0 \\ C_4 = \frac{h^2}{8\mu}\left(\rho \frac{\partial u}{\partial t} - \frac{\Delta p}{L}\right) \end{cases} \tag{2.18}$$

Substituting the coefficients, Eq. 2.16 becomes:

$$\frac{\partial u}{\partial t}\left[\frac{\rho y^2}{2\mu} - \frac{h^2 \rho}{8\mu}\right] = \frac{\Delta p}{L}\left(\frac{y^2}{2\mu} - \frac{h^2}{8\mu}\right) + u \tag{2.19}$$

Then taking the integral average (integrating the function on $y = \pm h/2$ and dividing by h) over the *y* axis to get the mean values, the system equation finally becomes:

$$\frac{\partial u}{\partial t} = -\frac{12\mu}{\rho h^2} u + \frac{\Delta p}{\rho L_{plates}} \tag{2.20}$$

The pressure drop is obviously related to the segment shown in Fig. 2.5. In order to express the pressure drop between points $2 - out$ with respect to Fig. 2.5, the generalized Bernoulli equation is used and the final form can be written as [3]:

$$p_2 = p_{in} + (1 - \zeta)\rho \frac{u_1^2}{2} - \rho \frac{u_2^2}{2} \tag{2.21}$$

where ζ is derived from Eq. 2.9. The fluid velocities are calculated using the relation $Q = u \cdot A$ that links the volumetric flowrate to the cross sectional area of the flow.

Finally, the volumetric flowrate can be easily estimated using the continuity equation:

$$Q = u \cdot A_{out}(x) \rightarrow \dot{m} = \rho Q \tag{2.22}$$

Fluid Load The fluid flow exerts a load on the valve seat. Such force influences the dynamic behaviour of the plunger. The fluid flow load can be described by using the momentum conservation of *Reynolds Transport Theorem* within the closed volume represented in Fig. 2.5 [47]. Taking into account the time-derivative of the momentum within the control volume and the total flux, the following equation can be written:

$$\frac{d}{dt}\int_{CV} (\rho u) dV + \oint_A \rho u (\mathbf{u} \cdot \mathbf{n}) dA = p_{in} A_{in} - F_{f,pl} \tag{2.23}$$

where CV stands for control volume, whereas the surface integral is limited to the boundary area. $F_{f,pl}$ is the force that the plunger exerts on the fluid, opposite to the one that the flow exerts on the

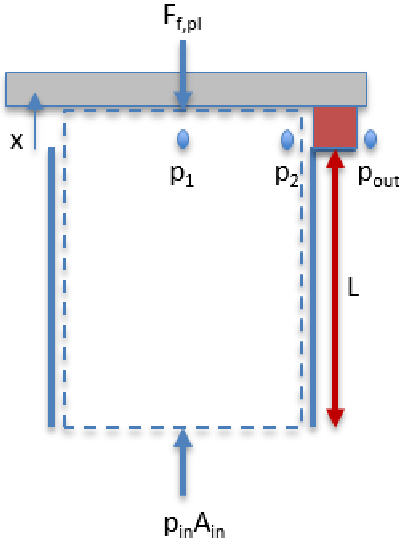

Figure 2.5: Schematics of the fluid domain when flow between parallel plates is assumed. The red section shows the region of interest.

plunger according to Newton's 3^{rd} law. The inlet and outlet velocity is assumed to be orthogonal to the reference cross-sectional area, thus it is possible to simplify Eq. 2.23 into to obtain an expression for the fluid load:

$$F_{f,pl} = p_{in}A_{in} + \rho u^2 A_{in} - \rho \frac{dQ(x)}{dt}(x + L_0) \tag{2.24}$$

where $F_{f,pl}$ is the fluid-plunger interaction load, A_{in} is the inlet area, L_0 is the minimum height of the variable control volume and x is the displacement of the plunger. The first two terms of Eq. 2.24 are representative for the steady-state fluid loads [47], [48]. The last term, instead, is related to the transient behavior of the fluid flow. In particular, the derivative of the volumetric flowrate in time governs such load term: hence, in order to use such expression, an accurate model of the transient phase of the volumetric flowrate evolution would be critical. Nevertheless, according to numerical simulations to investigate its influence, the transient term is found to be negligible compared to the steady-state loads.

2.1.4. Mechanical Domain

The valve plunger is subject to several forces exerted by different components of the valve itself. The ferromagnetic plunger is constrained to move along the inner structure of the coil. Whenever the coil is energized by current *i*, a magnetic flux is set up. The magnetic field pulls the plunger upward, changing the relative position with respect to the coil. The motion results in the decrease of the gap between the top structure and the plunger, as well as an increase of the side area between the plunger and the cylindrical iron core [45]. These processes are driven by the tendency of the electromagnetic circuit to decrease the equivalent reluctance and hence increase the inductance of the coil. The motion of the plunger is also influenced by the fluid load as well as by the elastic and viscous damping forces. The dynamic equation, which describes the motion of the plunger, is obviously Newton's 2^{nd} law and can be written as follows:

$$M\ddot{x} + c\dot{x} + k(x - x_0) = F_{mag} + F_{f,pl} - p_{out}A_{in} \tag{2.25}$$

where *c* is the viscous coefficient, *k* is the elastic constant of the spring, x_0 is the spring pre-load, F_{mag} is the magnetic force and $F_{f,pl}$ is the fluid-plunger interaction load. Eq. 2.25 has been derived with respect to the free body diagram in Fig. 2.6.

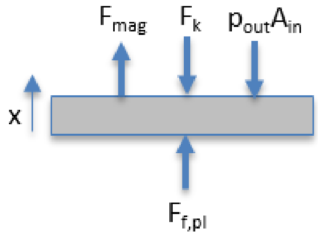

Figure 2.6: Free body diagram for the moving plunger.

2.1.5. State-Space Model

The sets of differential equations that are included in the mathematical model are of different orders and, above all, include many variables and parameters other than the the inputs and outputs. The state variables are a set of independent variables that completely determine the behavior of the system, given their initial condition. In order to develop the systematic analysis of the system dynamics, the standard form is to represent the model in the state-space form. The state-space representation consists of a set of first-order differential equations plus an algebraic equation representing the output. The higher-order differential equations can always be turned into a set of first order differential equation by inserting $n-1$ additional state variable, where n is the order of the differential equation [49].

For the considerations made in section 2.1.3, two different state-space models have been developed. The major difference lies in the number of state variables, in particular whether the fluid outlet velocity is considered or not. If the the fluid flow is described by the *orifice equation*, the state variables are those listed below:

- $x = x_1$ = displacement of the plunger
- $\dot{x} = x_2$ = velocity of the plunger
- $i = x_3$ = electric current trough the coil

and the group of equations describing the dynamics of the system can be expressed as follows:

$$\dot{\mathbf{x}} = \left\{ \begin{array}{c} x_2 \\ \\ \frac{1}{M}\Big(-cx_2 - k(x_1 - x_0) + F_{mag}(x_1, x_3) + F_{f,pl}(x_1) - p_{out}A_{in} \Big) \\ \\ \frac{1}{L(x_1)}\Big(u(t) - x_3\Big(R + x_2 \frac{dL(x_1)}{dx_1} \Big)\Big) \end{array} \right\} \tag{2.26}$$

$$y = \dot{m} = \rho Q(x_1) \tag{2.27}$$

where the input actuation voltage symbol has been changed into $u(t)$ to comply with standard control symbols. The output of the system is the mass flowrate and it is easy to see that the system is described by non-linear differential equations.

A few remarks are necessary upon the validity of the above model. First of all, the fluid flow is assumed to establish following the dynamics of the moving plunger, hence it is expected that the model delivers inaccurate results for the transient behaviour of the flow. This issue has been solved, as already mentioned, by inserting an additional state variable capable of describing the time derivative of the fluid velocity. Furthermore, the model makes use of several other assumptions such as neglecting the transient fluid loads and setting the frictional viscous forces linearly proportional to the velocity of the plunger and the coefficient c. Moreover, the effect of magnetic reluctance of the metal surrounding the coil or in the plunger is neglected. This, in turns, allows the use of the model to simulate different devices without knowing perfectly the composition of the inner structure, both in terms of materials and geometry.

The reason why all these assumptions have been made is to keep the model more easily solvable, and more, to allow the model to disregard the actual hardware. The twofold objective of developing a model capable of yielding good performance predictions and at the same time be simple to handle to develop control concepts finds a compromise in the adoption of the above-mentioned assumptions. Nevertheless, to improve the accuracy of the model, one could always investigate the real behaviour of a particular device and upgrade the model to a more realistic representation of the physical processes. For instance, although very small, the magnetic reluctance of the metal structure may be included if the geometry is perfectly known, yielding a more accurate representation of the establishment of the magnetic actuation force. Furthermore, the transient fluid loads were contributing only in a minor percentage but nothing can be said if the geometry changed or the micro-valve was further miniaturized.

The second state-space model that has been derived is able to describe the transient flow by introducing a differential equation describing the time derivative of the fluid velocity. The state variables are those listed below:

- $x = x_1$ = displacement of the plunger
- $\dot{x} = x_2$ = velocity of the plunger
- $i = x_3$ = electric current trough the coil
- $u_{fluid} = x_4$ = fluid velocity in the region between parallel plates

and the group of equations describing the dynamics of the system can be expressed as follows:

$$\dot{\mathbf{x}} = \left\{ \begin{array}{c} x_2 \\ \\ \frac{1}{M}\left(-cx_2 - k(x_1 - x_0) + F_{mag}(x_1, x_3) + F_{f,pl}(x_1) - p_{out}A_{in} \right) \\ \\ \frac{1}{L(x_1)}\left(u(t) - x_3\left(R + x_2 \frac{dL(x_1)}{dx_1} \right) \right) \\ \\ -\frac{12\mu}{\rho(x_1+x_{u0})^2} x_4 + \frac{\Delta p_\zeta}{\rho L_{plates}} \end{array} \right\} \tag{2.28}$$

$$y = \dot{m} = \rho x_4 A_{out}(x_1) \tag{2.29}$$

In the fourth equation of 2.28, the denominator of the first term has been modified with respect to the derivation proposed in section 2.1.3. The reason lies in the fact that if no initial offset is put in the height of the parallel plates channel, there would be a singularity for $x_1 = 0$, namely the rest position of the valve.

In section 2.3, insights on the advantages and disadvantages of the two models are presented. From now on, the words *analytical model* and *state-space model* will be used interchangeably.

2.2. Numerical Model

The analytical model developed in section 2.1 is a powerful tool for simulating the system and designing the controllers. Nevertheless, it needs validation due to the fact that many assumptions have been made throughout the derivation. Once again, the purpose of this work, in particular within the modelling task, is to develop a tool regardless of the specific device, which will then be used. To this extent, the validation process should not be done experimentally as a first step but rather by making use of sophisticated software that perform numerical computations. Hence, it is possible to select which physics to solve for as well as to employ the simplified geometry, which has been the baseline to develop the analytical model in section 2.1.

The most critical processes that need to be validated are the following:

- The motion of the plunger for a given input voltage. Basically, this implies the validation of the electromagnetic coupling between the energized coil and the plunger.
- The mass flowrate for a given plunger displacement. In other words, the fluid flow transient behaviour needs to be checked inasmuch the parallel plates is a strong assumption.

The work-flow has been organized in a step-wise approach. Firstly, the modelling has focused on the electromagnetic coupling, which has later been linked with the fluid domain. The description of the adopted methods will be presented as a whole, thus with reference to the complete simulation. COMSOL Multiphysics was selected to perform the above-mentioned analysis.

2.2.1. Geometry

As already described in section 2.1.1, the geometry is generic and representative of a large number of actual devices. The geometry components, mainly rectangles, are defined directly in COMSOL geometry builder. The 3D simulation has been carried with the aid of the *axisymmetric* functionality within COMSOL. Such feature allows the user to define the simulation object as a planar structure but extends the result to a 3D domain by applying the axisymmetric condition. The geometry utilized for simulations is shown in Fig. 2.1. The main dimensions are summarized in Tab. 2.1.

An important option to select is the *form an assembly* feature at the end of the geometry creation. The software then treats the geometry as a collection of the geometry objects instead of uniting them. To connect different boundaries that belong to the same continuous field, the *create pairs* option needs to be used. However, the identity pairs are usually created automatically by the software. The assembly feature allows to model physics where different geometry domains move or slide with respect to each other. Furthermore, by forming an assembly, it is possible to use different meshes for different geometries independently.

Table 2.1: Comprehensive list of the electromagnetic parameters and values used to set the simulation.

Parameter	**Value**
Inlet Diameter [mm]	1
Solenoid Diameter [mm]	5
Solenoid Height [mm]	20
Initial Outlet Height [mm]	0.001

2.2.2. Electromagnetic Coupling Physics

To simulate the electromagnetic coupling between the coil, the iron case and the plunger the *Magnetic Fields Interface*. According to the user manual [50], the module is particularly suitable for computing magnetic field and induced current distributions in and around coils, conductors, and magnets. Maxwell's equations are solved in the domains to which the physics is assigned. The formulation of the laws makes use of the magnetic vector potential and other dependent variables for particular domains, such as electric coils for which the scalar electric potential is employed.

For the transient study, clearly the most relevant for this analysis, the set of equations that are solved in the *Magnetic Fields Interface* are:

$$\nabla \times \mathbf{H} = \mathbf{J} \tag{2.30}$$

where **H** is the magnetic field and **J** the current density;

$$\mathbf{B} = \nabla \times \mathbf{A} \tag{2.31}$$

where **B** is the B-magnetic field or total magnetic field and **A** is the magnetic potential;

$$\mathbf{J} = \sigma \mathbf{E} + \sigma \mathbf{v} \times \mathbf{B} + \mathbf{J_e} \tag{2.32}$$

where **E** is the electric field, **v** is the velocity of the conductor and $\mathbf{J_e}$ is an externally generated current density;

$$\mathbf{E} = -\frac{\partial \mathbf{A}}{\partial t} \tag{2.33}$$

The simulation is run assuming linear magnetic properties, for this reason the constitutive relation is built using the relative permeability in the following fashion:

$$\mathbf{B} = \mu \mu_r \mathbf{H} \tag{2.34}$$

where μ is the vacuum magnetic permeability and μ_r is the relative magnetic permeability. Equation 2.34 is applied to the plunger, the iron core and obviously the air environment. The coil parameters are defined through the a specific node in the simulation. The input voltage is user-defined and inserted in the following equation to determine the current density:

$$\mathbf{J_e} = \frac{N(V_{coil} + V_{ind})}{AR_{coil}} \mathbf{e_{coil}} \tag{2.35}$$

where N is the number of turns in the coil, V_{coil} is the applied voltage, V_{ind} is the induced voltage, A is the coil cross section area, R_{coil} is the coil resistance and $\mathbf{e_{coil}}$ is the direction vector.

A comprehensive list of the input parameter needed for the *Magnetic Fields interface* module is shown in Tab. 2.2. The parameters are set to be representative of the hardware that will then be employed in the tests. Even though precise data on the inner geometry and structure of the micro-valve are not available, the dimensions are plausible and derived from indirect measurement, such as the coil equivalent resistance. The inner materials are chosen after the literature review upon typical materials adopted for electro-magnetic actuated valves.

Table 2.2: Comprehensive list of the electromagnetic parameters and values used to set the simulation.

Parameter	**Value**
Coil Turns [-]	1000
Input Voltage [V]	12-6
Coil Diameter [mm]	5

Object	**Material**
Coil	Copper
Case	Iron
Cavities	Air

The software enables the automatic calculation of the Lorentz force within a predefined domain. The Lorentz force gives the force distribution which is sensed by a conductor that carries electric current in a region where a magnetic flux **B** is present. The Lorentz force can be expressed as:

$$\mathbf{F} = \mathbf{J} \times \mathbf{B} \tag{2.36}$$

The Lorentz force is valid for conducting materials, whereas for non-conducting domains a different method, based on the Maxwell stress tensor is used. The Maxwell stress tensor variable, which is available as a boundary variable, is integrated over the boundaries of the object domain taken as reference. The equations to calculate the force on the plunger is:

$$\mathbf{F} = \int_{\partial\Omega} 2\pi r \mathbf{n} T dS \tag{2.37}$$

A snapshot of the solved model is shown in Fig. 2.7.

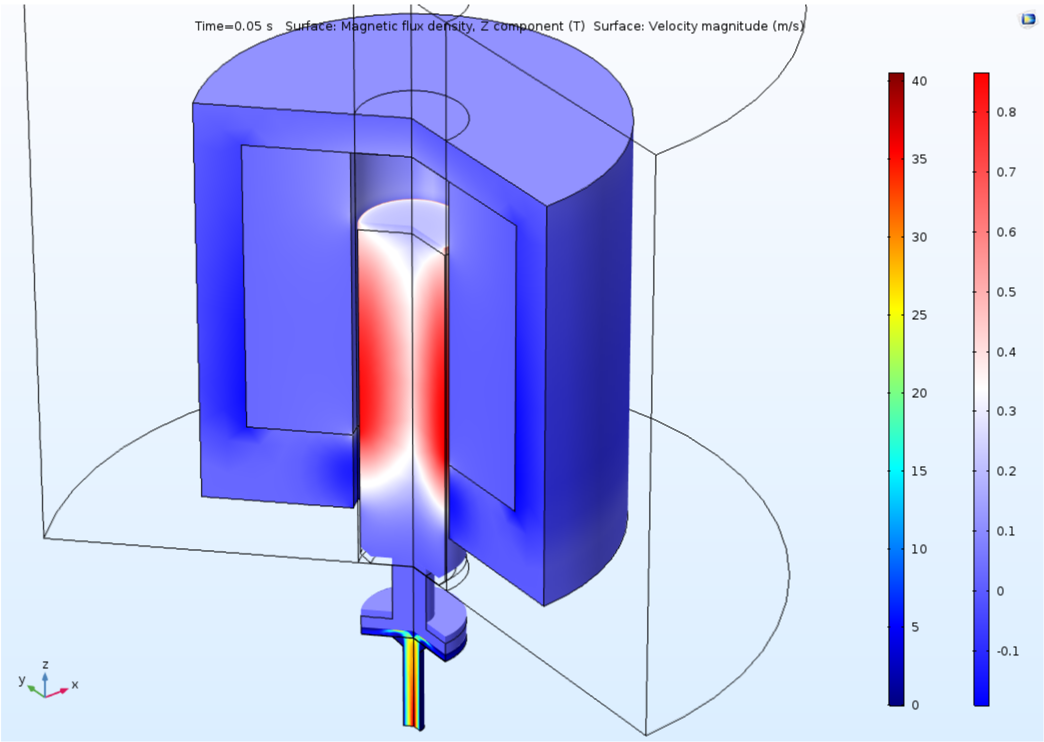

Figure 2.7: Detail of the solved model. The magnetic flux for the revolved geometry is shown for the coil, the iron core and the plunger. The fluid flow is shown for the fluid channel below the plunger.

2.2.3. Laminar Flow Physics

To model the fluid flow within the micro-valve, the *Laminar Flow* interface within the built-in COMSOL *Single-phase Flow* module was chosen. The limited dimension of the fluid channel (below 1 mm in its maximum size) allows the introduction of the laminar assumption. Indeed, the Reynolds number, defined as follows according to [1]:

$$Re = \frac{\rho u d}{\mu} \tag{2.38}$$

where ρ is fluid density, u is fluid bulk velocity and d is a characteristic dimension, are all below the limit of 2000, which represents the transition between laminar and turbulent flow [1], see Fig. 2.8. The *Single-Phase Flow* module solves the Navier-Stokes equations that in the general form read:

$$\frac{\partial \rho}{\partial t} + \nabla \cdot (\rho \mathbf{u}) = 0 \tag{2.39}$$

$$\rho\left(\frac{\partial \mathbf{u}}{\partial t} + \mathbf{u} \cdot \nabla \mathbf{u}\right) = -\nabla p + \nabla \cdot \tau + \mathbf{f} \tag{2.40}$$

$$\rho c_v\left(\frac{\partial T}{\partial t} + T \cdot \nabla T\right) = -p\nabla \cdot \mathbf{u} + \nabla \cdot (k\nabla T) + \tau \cdot \nabla \mathbf{u} \tag{2.41}$$

where ρ is the density, t is the time, **u** is the fluid field velocity, p is the pressure, τ is the viscous stress tensor, **f** is the resultant of external forces acting on the control volume, T is the temperature and c_v is the specific heat at constant volume. The above equations are also known as continuity, momentum and energy equations respectively. The Navier-Stokes equations have been derived in Chapter 1. Since water is used in the system, its incompressibility yields a further simplification of Eq. 2.39:

$$\rho \nabla \cdot \mathbf{u} = 0 \tag{2.42}$$

Additionally, *no-slip* wall boundary condition is used. The inlet-outlet condition is determined by the entrance and exit pressure respectively. A comprehensive list of the parameters used in the fluid domain is given in Tab. 2.3.

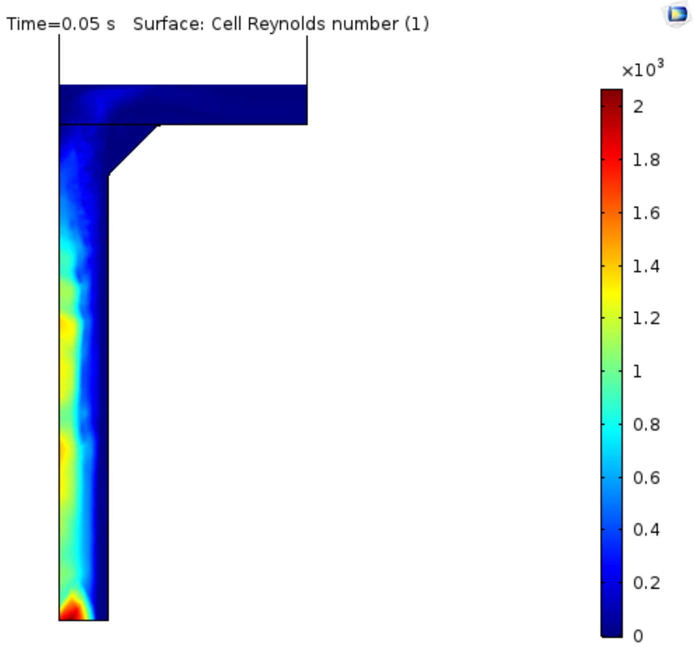

Figure 2.8: Cell Reynolds number simulation output. Steady-state instant at t = 0.05 s.

Table 2.3: Comprehensive list of the fluid parameters and values used to set the simulation. Water is used as fluid.

Parameter	**Value**
Density [$\frac{kg}{m^3}$]	1000
Temperature [K]	298.15
Inlet Gauge Pressure [bar]	5
Outlet Gauge Pressure [bar]	0

2.2.4. Dynamics

The motion of the plunger is determined by Newton's 2^{nd} law, expressed as a global differential equation. In order to integrate such differential equation the *Global ODEs and DAEs* module is employed. In particular the state variables that are determined are the displacement and the velocity of the plunger. To solve for both of these, the second-order differential equation $F = m\ddot{x}$ is decoupled into two first-order differential equations, namely:

$$\dot{x}_{pl} - v_{pl} = 0 \tag{2.43}$$

$$M\dot{v}_{pl} + cv_{pl} + kx_{pl} - F_{tot} = 0 \tag{2.44}$$

where x_{pl} is the plunger displacement, v_{pl} is the plunger velocity, c is the viscous coefficient, k is the spring elastic coefficient and F_{tot} is the total force load acting on the plunger. The two state variables, namely x_{pl} and v_{pl} are fundamental to determine the behaviour of the moving mesh, as explained in the next section. A comprehensive list of the parameters used in the fluid domain is given in Tab. 2.4.

Table 2.4: Comprehensive list of the dynamics parameters and values used to set the simulation.

Parameter	**Value**
Plunger Mass [mg]	0.8
Elastic Spring Constant [$\frac{N}{m}$]	10^4
Viscous Coefficient [$\frac{N \cdot s}{m}$]	500

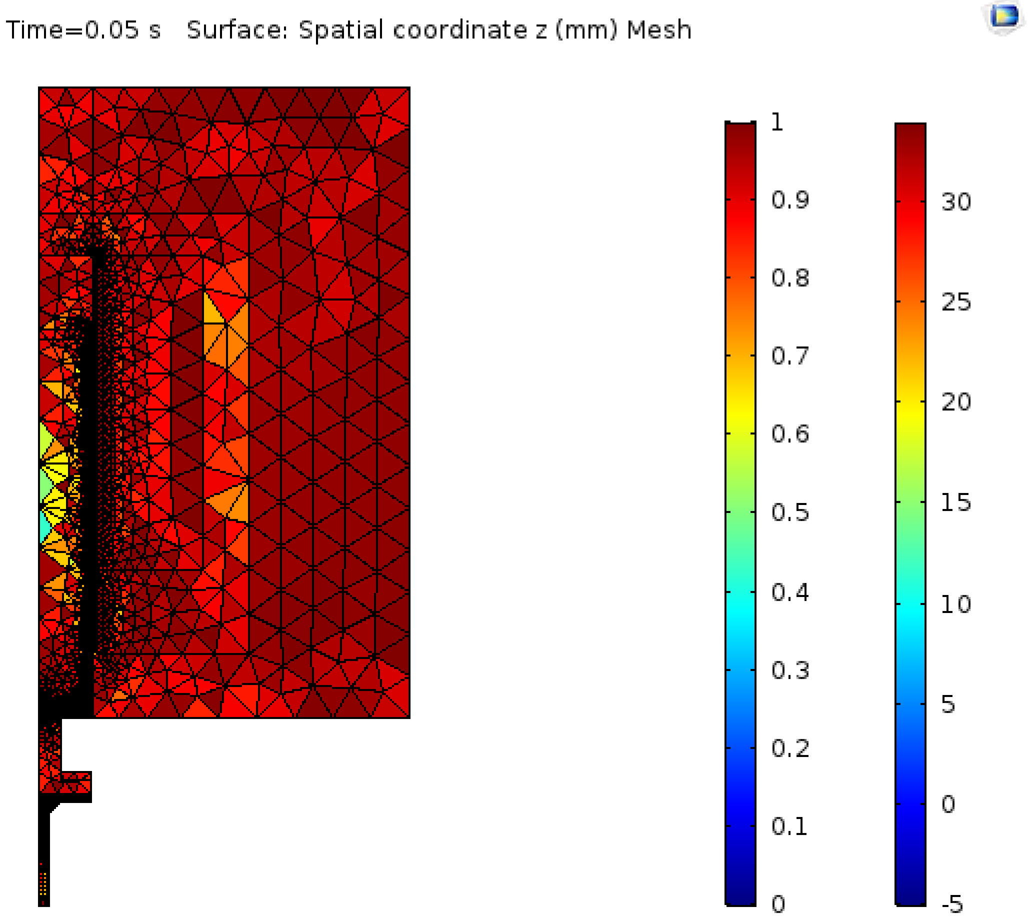

Figure 2.9: Detail of the mesh.

2.2.5. Moving Mesh

The relative position of the plunger changes with respect to the rest of the structure whenever a voltage is applied to the coil. To simulate this mechanism, a moving mesh is needed with the consequent complexity added to the model. The *Moving Mesh* interface is used when the geometry changes shape due to physical phenomenon without material being removed or inserted. The *Moving Mesh* interface is used when a displacement of the spatial frame occurs relative to the material frame. The spatial frame is the usual, fixed, global, Euclidean coordinate system, whereas the material frame is a coordinate system that identifies material points by their spatial coordinates (X, Y) in some reference configuration. Fig. 2.9 shows the overall mesh used. The Laplace smoothing type is used to reconstruct the mesh every subsequent time step. In Fig. 2.10 and 2.11, the mesh in the fluid region squeezed by the plunger is shown at the initial and final instant. The time-dependent moving mesh is set to follow the displacement of the plunger, x_{pl} derived from the set of differential equations described in section 2.2.4, namely Eq. 2.43 and 2.44.

In order to validate the mesh, a very simple mesh convergence analysis has been carried out. Such analysis, although very basic, allows the user to understand whether the results are influenced by numerical artifacts derived by the particular mesh or they are representative of the true physical processes. The mesh is generated automatically by the software, based on the physics and the desired level of refinement. The mesh has been built as *fine* throughout the whole project, as shown in Fig. 2.9. To carry out the convergence analysis, another mesh generated as *normal* refinement has been employed, yielding compatible results with the simulation results of the finer mesh. The limitations on the computing power forced the mesh convergence analysis to be performed with a less fine mesh rather than a more refined one.

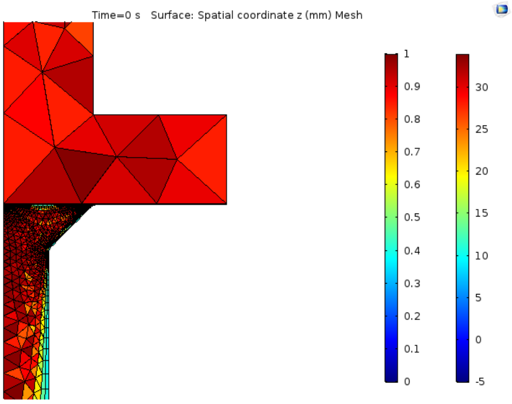

Figure 2.10: Parallel plates region mesh at initial time t = 0 s.

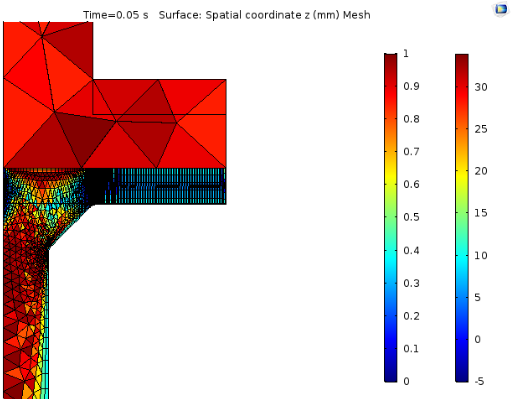

Figure 2.11: Parallel plates region mesh at initial time t = 0.05 s.

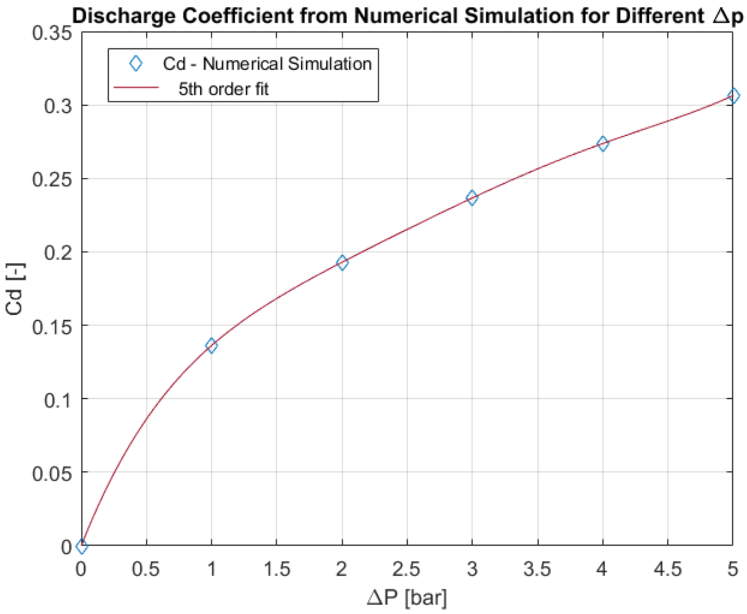

Figure 2.12: Discharge coefficient calculated using the numerical simulation together with a 5^{th} order fitting.

2.3. Analytical and Numerical Model Comparison

In this section, the comparison between the analytical and numerical model is presented. In light of the two main processes to investigate, namely the plunger displacement for a given input voltage and the flowrate for a given displacement, the discussion will focus on such particular results out of the simulations. Before proceeding with the real comparison, the results from the numerical simulations are used to calculate the discharge coefficient for different pressure at the inlet and outlet. Such coefficient is very hard to estimate theoretically, hence a numerical simulation is needed. This does not imply that the analytical model is tuned to yield the same results because all the differential equations are developed regardless of the discharge coefficient. For instance, the flowrate would match exactly the result from the numerical equation only if the plunger displacement matches as well, which does not depend in any way to the discharge coefficient. Fig. 2.12 shows the discharge coefficient calculated using the numerical simulation together with a 5^{th} order fitting. However, if the purpose is to decouple the two models to predict the performances a real device, the discharge coefficient for the determining the pressure loss can be derived from the actual datasheet. Indeed, when the models are validated experimentally, hence with an actual hardware, the pressure loss for the analytical model is calculated by the datasheet value for the discharge coefficient, using Eq. 2.9.

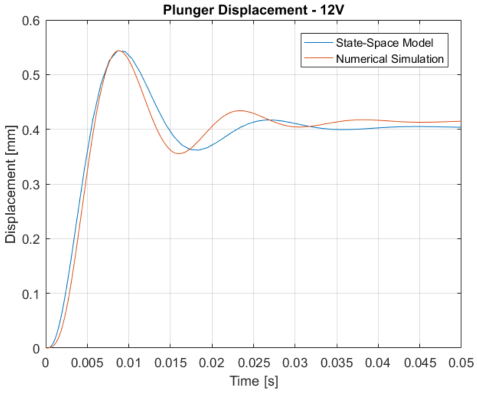

Figure 2.13: Comparison between numerical and analytical simulation for the plunger displacement for 12 V input voltage.

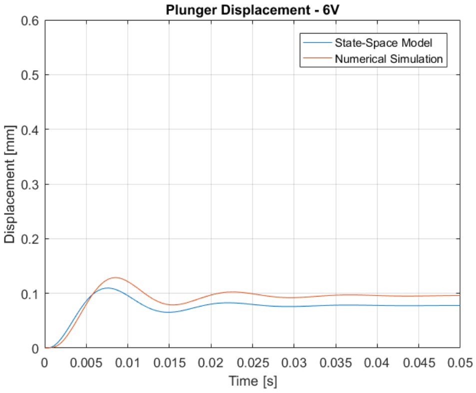

Figure 2.14: Comparison between numerical and analytical simulation for the plunger displacement for 6 V input voltage.

In order to validate the electromagnetic coupling between the energized coil and the consequent plunger motion, two input voltage have been used, namely 12 V and 6 V. The choice of investigating the behavior for two different input voltages is driven by two main reasons: on one hand, the high non-linearity of the model requires the validation to be carried for different amplitudes of the input voltage, since no linear behavior may be expected and hence nothing can be said for input voltages far from those simulated; on the other hand, regarding the real implementation, the micro-valves suitable for the Delfi-PQ implementation are solenoid actuated micro-valve with input voltage of 6 or 12 V. Even though the selected hardware for the experimental implementation in Chapter 3 is actuated by a 12 V signal, future developments of the project may employ devices that require 6 V signal.
The results are shown in Fig. 2.13 and 2.14 respectively. The transient behaviour of the plunger is very well resembled, in particular in the case of 12 V input voltage. The difference in the steady-state value is within 10% in both situations. The analytical model underestimates the displacement throughout the entire time span, but the oscillatory transient behaviour is comparable. Indeed, the overshoot peak occurs at the same instant in time, which represents a good predicting result. Furthermore, the rise time and settling time are $\sim 5\ ms$ and $\sim 40\ ms$ for both cases.

The electric current flowing into the coil is responsible for the magnetic force generation. Thus, it is important to investigate whether the simplified electromagnetic circuit, analyzed in section 2.1 represents correctly the electric behaviour. Fig. 2.15 shows the comparison between the current obtained from the analytical model and the one from the numerical simulation for two different input voltages, namely 6 V and 12 V. The major difference between the two results is the rise time. Indeed, the current curve from the state-space model presents a steeper region from 0 to $\sim 5\ ms$ with respect to the result of the numerical simulation. Nevertheless, the steady-state values are compatible. This is not surprising since it is determined solely by the equivalent resistance of the coil, see Eq. 2.1.

The mass flowrate for a given plunger displacement and, consequently, for a given input voltage is a fundamental parameter, since it represents the output of the system. For this reason a comparison between the analytical and numerical model has been performed. At this point, it is important to recall what has been discussed in section 2.1.3. If the *orifice equation* is used, the settling evolution of the fluid flow follows the dynamics of the plunger linearly. The proportionality constant is indeed the discharge coefficient. On the other hand, the plunger displacement and the fluid velocity can be decoupled by introducing a state variable representative of the fluid velocity at the outlet. Figure 2.16 shows the results from the numerical simulation regarding the plunger displacement as well as the outlet flowrate. It is clear how the mass flowrate evolution on time significantly differs from the dynamics of the plunger. Thus, it is more appropriate to consider a dedicated differential equation to describe the fluid flow. However, the complexity of Navier-Stokes equations leads to the need of making strong assumptions regarding the flow, which might alter the effectiveness of predicting the real physics occurring within the valve. Fig. 2.17 shows the comparison between the numerical model and the analytical one, which includes the fluid outlet velocity as state variable. One remarkable achieve-

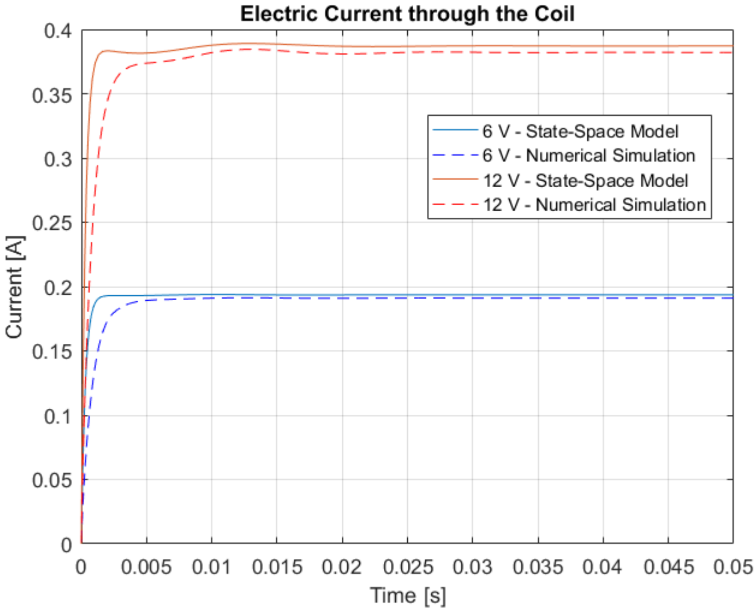

Figure 2.15: Comparison between numerical and analytical simulation for the electric current flowing through the coil for two different input voltages, namely 6 V and 12 V.

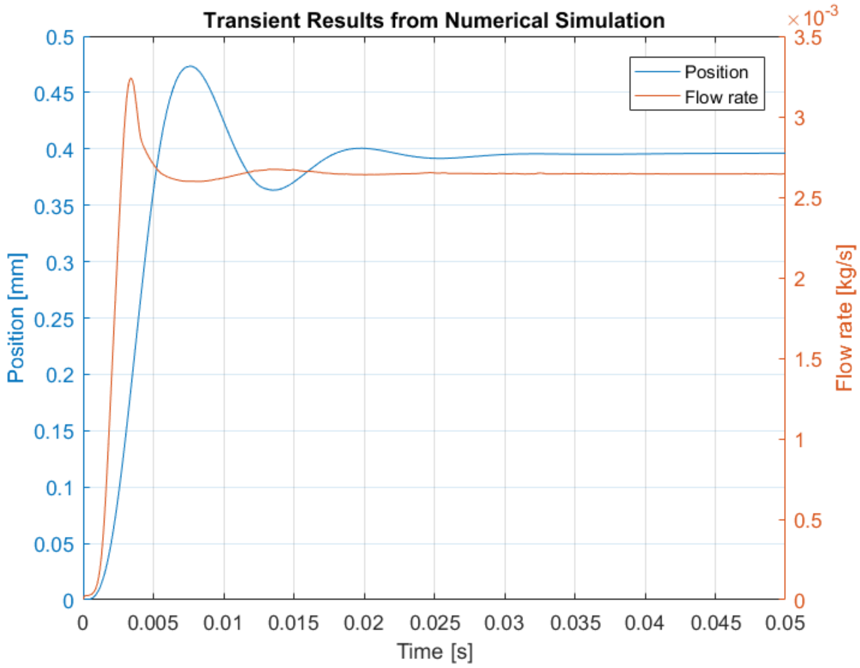

Figure 2.16: Plunger displacement and mass flowrate obtained as results of the numerical simulation

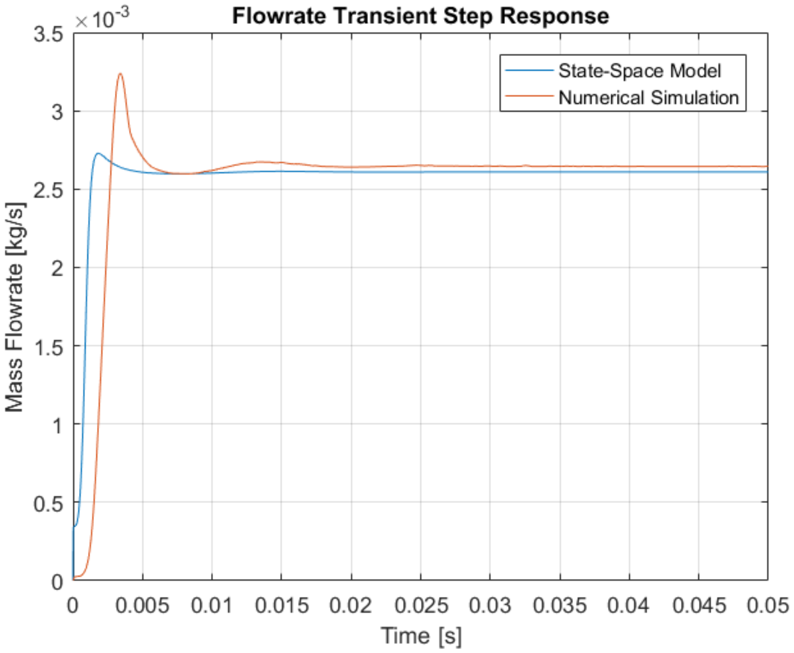

Figure 2.17: Transient behaviour of the fluid flowrate within the valve. The state-space model includes the fluid velocity as state variable. The curve from the analytical model has a step during the initial phase: this is due to the initial gap height x_{u0}, which is added to avoid the singularity at $x = 0$. Lowering x_{u0} reduces the step without changing the dynamic response.

ment is that the steady-state flowrate is compatible with the results from the numerical simulation. Moreover, by implementing a differential equation dedicated to the fluid flow, it is possible to resemble the overshoot occurring when the valve is actuated. However, there is still a difference in the time instant when the peak occurs and, above all, in the amplitude of the peak. The state-space model delivers a faster rise and settling time with respect to the numerical model and the difference is within $\sim 30\%$. Although there might be room for improvements in the analytical model, it is important to note that using the *orifice equation*, being the most adopted in literature, such difference would increase to nearly 110%. As said, the amplitude of the initial peak differs significantly between the numerical and analytical model. There are several potential reasons why this discrepancy occurs. First of all, even if negligibly, the transient fluid loads contributes in the opening of the valve during the initial phase; hence, the brief transient where the overshoot occurs is larger if the additional transient fluid loads are taken into account. The description of the transient loads in Eq. 2.24 is a simplified one and influences only slightly the outcome of the analytical model; nevertheless, a more accurate description of such contribution could, in principle, resemble better the real case scenario. In addition, the assumption of fluid flow between two infinite parallel plates may lack in accuracy for the transient phase when the flow is established. The flow can be assumed to be radial to resemble the real scenario more realistically, however one needs to take into account that the derivation from Navier-Stokes equation become somewhat cumbersome.

The parameters used in the analytical model simulations are summarized in Tab. 2.5.

Table 2.5: Comprehensive list of the parameters set in the analytical model to run the simulations for the comparison.

Parameter	Value
Plunger Mass [mg]	0.8
Elastic Spring Constant [$\frac{N}{m}$]	10^4
Viscous Coefficient [$\frac{N \cdot s}{m}$]	500
Voltage [V]	6-12
Coil Resistance [Ω]	31
Coil Turns [-]	1000
Δp [bar]	1-5

Parameter	Value
Inlet Diameter [mm]	1
Solenoid Diameter [mm]	5
Solenoid Length [mm]	20
Initial Gap Height [m]	10^{-8}
ρ_{H2O} [$\frac{kg}{m^3}$]	1000
μ_{H2O} [$Pa \cdot s$]	0.001

2.4. Sensitivity Analysis

The model developed in chapter 2 is based on equations derived for a generic solenoid-actuated micro-valve. Consequently, several parameters were introduced to specify geometric features, electric and magnetic coupling and dynamics feature. Tab. 2.6 lists the main parameters that need to be set for the simulation to run. However, most of the parameters are unknown for COTS component and need to be smartly set in order to produce reasonable results. In order to study how uncertainty in the output of a model can be attributed to different sources of uncertainty in the model input, a *sensitivity analysis* is required. The sensitivity analysis is performed taking the mass flowrate as output reference variable. The mass flowrate is the process variable that determines the dynamics of the complete micro-propulsion dynamics, hence it is regarded as the most suitable choice for working out the analysis.

The *local sensitivity* analysis relies on gridded discretized variation of each parameter. It is often referred to *one-at-a-time* technique, insofar it investigates the influence of one parameter on the output variable at a time, keeping the rest of the parameters constant. In this way, a minor fraction of the design space is investigated, in particular when the number of parameters increase. Moreover, the required test cases scales exponentially with the amount of values that the parameters may assume. Another effective approach is the *global sensitivity* analysis, which is often implemented using Monte Carlo methods. Such approach uses a set of samples, based on a defined stochastic distribution for each parameter, to explore the design space extensively.

The work flow is as follows:

- Perform the global sensitivity analysis
- Calculate the correlation between output variable and parameters

The sensitivity analysis can be regarded as a tool to assess how uncertainties in the model output can be related to different sources of uncertainty in the input parameters [51]. Hence, it includes the analysis of the model inputs, model output and obviously the model itself. For simplicity, we call $\mathbf{p}$ the set of r parameters taken into account in the analysis and Y the output of the model.

Basically, there are two different approaches to perform the above-mentioned analysis: the *local* sensitivity analysis and the *global sensitivity* analysis. The former is based on the analysis of the derivative of the output $\frac{\partial Y}{\partial p_i}$ with respect to each parameter, given that the derivative is, in essence, the measure for the sensitivity of the output with respect to the parameter p_i. The drawbacks of such method are several, especially in the application presented in this thesis. First of all, the derivative of the output is complex and definitely time-consuming to calculate for each parameter in the state-space model, given the large number of parameters present in the micro-valve system. In addition, the derivative is calculated in baseline points, which are not representative of the entire design space, due to the non-linearity of the model.

The latter approach is based on a statistical approach and on the intuition that a restricted amount of sampling points, picked using a statistical approach, can produce much more relevant insights than the previous analysis. The *global* sensitivity analysis often uses Monte Carlo methods, which are based on sampling the values for each parameter from their distribution. The distribution for each parameter is uniform, given that no reasons are present to adopt any other statistical distribution. Again, given r parameters with their uniform distribution, N samples are taken to create the so-called input matrix $\mathbf{I}$:

$$\mathbf{I} = \begin{bmatrix} p_1^{(1)} & p_2^{(1)} & \dots & p_r^{(1)} \\ p_1^{(2)} & p_2^{(2)} & \dots & p_r^{(2)} \\ \vdots & \vdots & \ddots & \vdots \\ p_1^{(N)} & p_2^{(N)} & \dots & p_r^{(N)} \end{bmatrix} \tag{2.45}$$

The model is run for each of the N sets of input parameters, producing N-by-1 solution output vector:

$$\mathbf{Y} = \begin{bmatrix} y^{(1)} \\ y^{(2)} \\ \vdots \\ y^{(N)} \end{bmatrix} \tag{2.46}$$

The number of samples is recommended to be at least equal to *10r* in order to perform a correct correlation analysis [52]. The most effective way to visualize the results of the sensitivity analysis is the scatter plot. Given the boundary of the problem, r scatter plots can be created showing the different simulation output for the chosen parameter's range. The key in analyzing the scatter plots is defining the shape of the points cloud. The more "shaped" the cloud is, the more influential the parameter. Two opposite examples are shown in Fig. 2.18 and 2.22.

The quantitative analysis is carried out using statistical correlation. The correlation coefficient R can be calculated as follows:

$$R(i,j) = \frac{C(i,j)}{\sqrt{C(i,i)C(j,j)}} \tag{2.47}$$

where $C = cov(I,Y)$, in which I contains N samples of r parameters and Y contains N rows, related to the output for each sample. The data used in the analysis are selected according to the following three types of approach:

1. *Linear*: the analysis is performed using the raw data.
2. *Ranked*: the analysis is based on a ranked arrangement of the data.
3. *Kendall-Ranked*: the method is derived from the simple ranked one with an additional analysis on concordant pairs of data, namely data whose elements has the same rank.

To perform such analysis, Matlab *Sensitivity Analysis Toolbox* was used.

As shown in Tab. 2.6, the parameters belong to different domains (geometry, electric, magnetic and dynamics); hence it is reasonable to perform several limited sensitivity analysis on sub-groups beside the comprehensive one using all the parameters.

2.4.1. Geometry Parameters

As already mentioned, the geometry parameters are the following:

- $\mathbf{L_{plates}}$: the length of the region where the parallel plates assumption is used to describe the fluid flow, see Fig. 2.4. The range is $1 \cdot 10^{-4} - 1.5 \cdot 10^{-3}\ m$ with a uniform distribution.
- $\mathbf{d_{In}}$: diameter of the inlet fluid channel. The range is $5 \cdot 10^{-4} - 2 \cdot 10^{-3}\ m$ with a uniform distribution.
- $\mathbf{d_{Sol}}$: diameter of the internal solenoid. The range is $1 \cdot 10^{-3} - 8 \cdot 10^{-3}\ m$ with a uniform distribution.

With reference to the description presented above, the number of parameters is set to *r=3* and the number of samples consequently. The samples are drawn randomly from the probability distribution for each parameter, which is set as uniform in this case. The results from the sensitivity analysis, namely the overview results and the results from the correlation analysis, are presented in Fig. 2.18 and 2.19.

Name	Description
Geometric	
L_{plates}	Length of the parallel plates fluid region.
d_{In}	Inlet diameter of the fluid channel.
d_{Sol}	Diameter of the solenoid plunger.
Electric	
N	Number of coil turns.
R	Equivalent coil electric resistance.
Magnetic	
a	Bottom iron strips length.
dg_0	Initial upper air gap.
g	Side air gap.
Dynamics	
M	Mass of the moving plunger.
c	Viscous coefficient.
k	Elastic spring coefficient.

Table 2.6: List of input parameters analyzed in the sensitivity study.

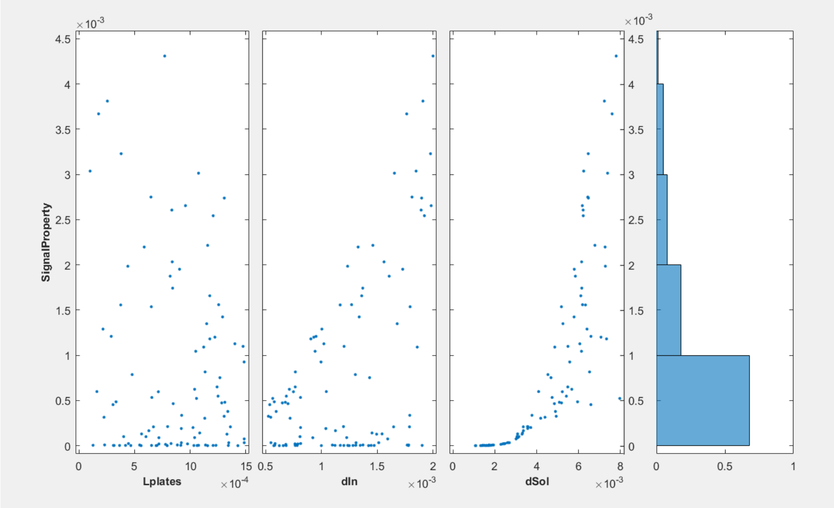

Figure 2.18: Overview of the scatter plots for different geometric parameters. On the right the number of results for different ranges of mass flowrate are reported.

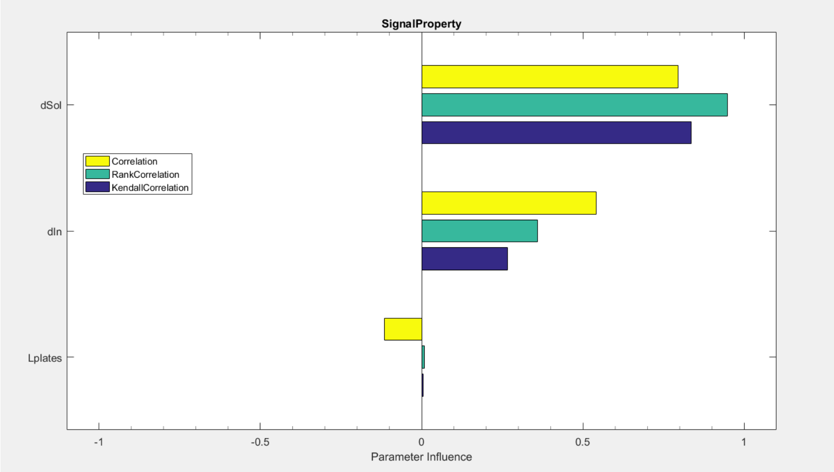

Figure 2.19: Parameters influence assessed by correlation analysis.

The scatter plots clearly shows that the solenoid diameter is the prominent parameter. This was expected, since the magnetic force, on which the plunger movement is based, is highly dependent on the solenoid diameter, according to Eq. 2.7. In particular both magnetic reluctances that are taken into account in the analysis of section 2.1.2 contain such factor. Nevertheless, intuitively, the inlet diameter plays an important role on the model and on its results. Indeed it is used to determine the flow within the valve and to eventually calculate the mass flowrate at the outlet. The results of the correlation analysis demonstrates how the most influential parameters are indeed the solenoid diameter and the inlet diameter. The length of the parallel plates is not significantly related to outlet mass flowrate, but it should not be excluded that it may affect other aspect of the simulation, such as the rise time.

2.4.2. Electric Parameters

The electric parameters that play a role in the simulation are:

- $\mathbf{N}$: number of coil turns. The range is $50 - 2 \cdot 10^3$ with uniform distribution.
- $\mathbf{R}$: equivalent electric resistance of the coil. The range is $10 - 200\ \Omega$ with a uniform distribution.

With reference to the description presented above, the number of parameters is set to *r=2* and the number of samples consequently. The samples are drawn randomly from the probability distribution for each parameter, which is set as uniform in this case. The parameters mainly affect the transient behaviour of the electric current, which in turns influences the magnetic force and thus the dynamic behaviour of the moving plunger, as shown in Eq. 2.28. The results from the sensitivity analysis, namely the overview results and the results from the correlation analysis, are presented in Fig. 2.20 and 2.21.

The scatter plots show a clear dependence of the simulation outcome upon both the number of coil turns and the equivalent coil resistance. The trend in Fig. 2.20 appears to be influenced for a variation in the number of turns between 500 to 1500, in which the scatter plot shows that increasing the number of coil turns affects the resultant mass flow rate. On the other hand, the electric resistance has a strong influence on the overall simulation result, leading to an almost null output for values above 100 Ω. This might be explained by a close look to Eq. 2.6. The resistance term is responsible for one voltage drop and more importantly on the steady-state electric current, which determines the magnetic force at the equilibrium. Nevertheless the majority of the terms in the equation are linked to the magnetic reluctance, which in turns contains the number of turns. It can be deduced the the number of turns in the coil affects the transient behaviour of the electric current and hence of the motion of the plunger. It is interesting to note that the two parameters have opposite correlation coefficient, positive and negative, meaning that the effects of increasing both tend to counterbalance.

2.4.3. Magnetic Parameters

The magnetic parameters are critical, being responsible for the actuation of the valve itself. Specifically, the magnetic parameters under analysis are with reference to Fig. 2.2:

- $\mathbf{a}$: bottom iron strips length. The range is $1 \cdot 10^{-3} - 5 \cdot 10^{-3}\ m$ with a uniform distribution.
- $\mathbf{dg_0}$: initial upper air gap. The range is $5 \cdot 10^{-4} - 5 \cdot 10^{-3}\ m$ with a uniform distribution.
- $\mathbf{g}$: side air gap. The range is $1 \cdot 10^{-4} - 1 \cdot 10^{-3}\ m$ with a uniform distribution.

With reference to the description presented above, the number of parameters is set to *r=3* and the number of samples consequently. The samples are drawn randomly from the probability distribution for each parameter, which is set as uniform in this case. Basically, the above parameters define the magnetic reluctance that is taken into account in the model. Indeed, if a close look at Eq. 2.3 is given, all the parameters can be identified in the magnetic reluctance definition. The results from the sensitivity analysis, namely the overview results and the results from the correlation analysis, are presented in Fig. 2.22 and 2.23. The scatter plots show a significant dependence of the simulated mass flowrate upon the initial air gap between the plunger and the upper part of the metal case. Such trend can be explained by looking again to Eq. 2.3, where the initial air gap dg_0 is employed. The bigger the parameter is, the weaker the magnetic force is. The equilibrium position, given by the balance of the elastic force and the magnetic one, is hence moved closer to the fluid channel, delivering a lower

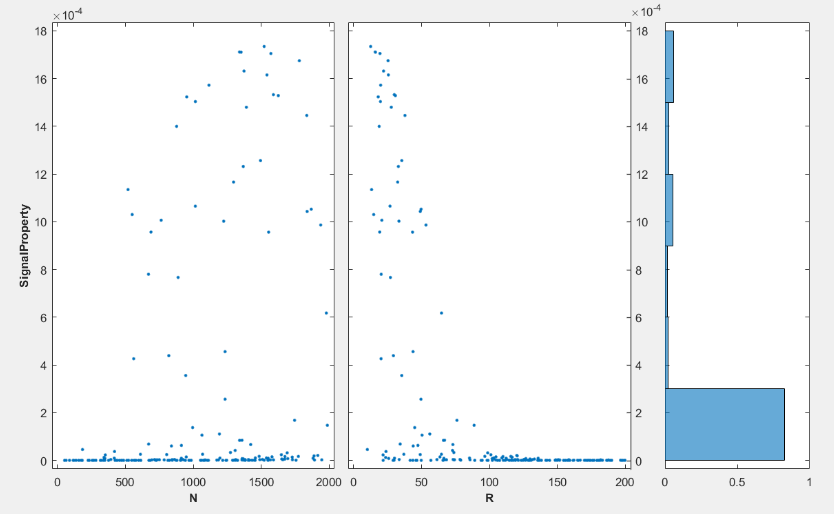

Figure 2.20: Overview of the scatter plots for different electric parameters. On the right the number of results for different ranges of mass flowrate are reported.

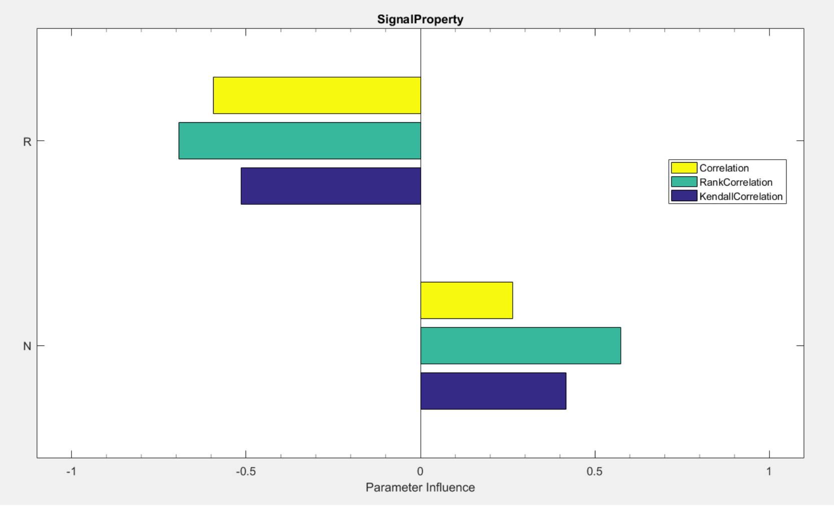

Figure 2.21: Parameters influence assessed by correlation analysis.

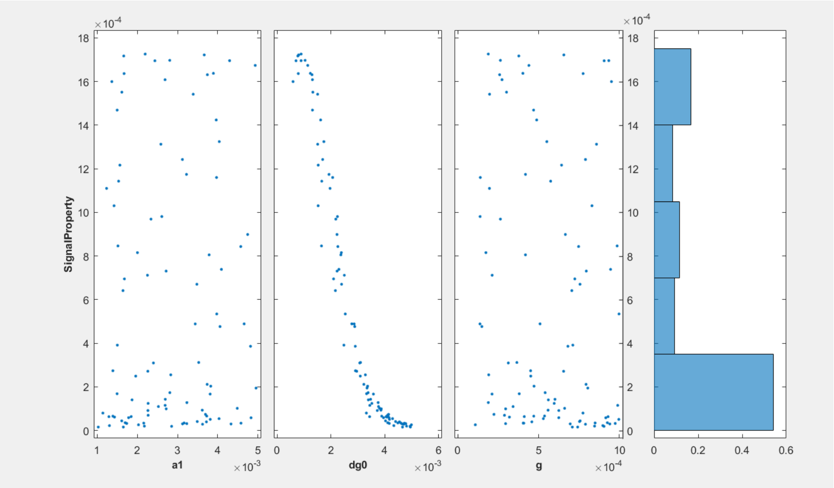

Figure 2.22: Overview of the scatter plots for different magnetic parameters. On the right the number of results for different ranges of mass flowrate are reported.

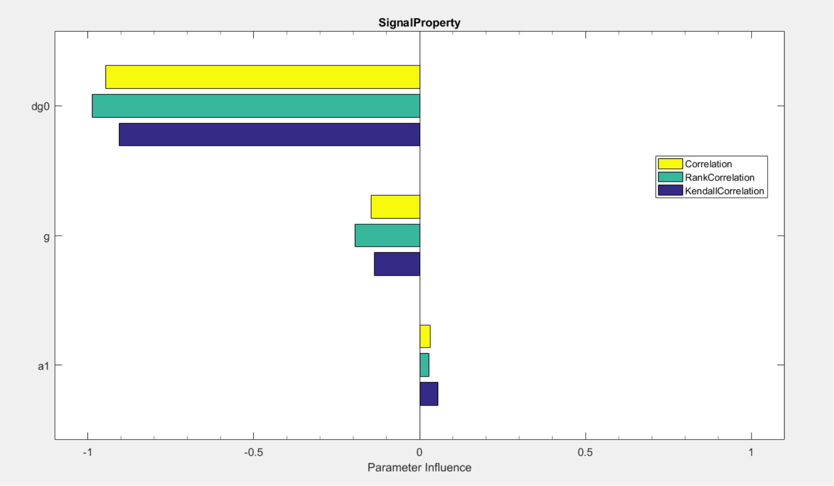

Figure 2.23: Parameters influence assessed by correlation analysis.

flowrate. On the contrary, the side configuration, namely the iron strip length and the air gap, is not impacting severely the outcome of the simulation being independent of the position of the plunger. Indeed the term of Eq. 2.3 comprising a and g parameters is a constant throughout the simulation.

2.4.4. Dynamics Parameters

The dynamics parameters are responsible for the dynamic behaviour of the moving plunger. Following the traditional approach of Newton 2^{nd} law, the parameters are linked to the displacement and its first and second derivative. Specifically, the parameters are:

- $\mathbf{M}$: mass of the plunger. The range is $1 \cdot 10^{-6} - 1 \cdot 10^{-3}\ kg$ with a uniform distribution.
- $\mathbf{c}$: viscous coefficient of the environment surrounding the plunger. The range is $1 - 1100\ \frac{N \cdot s}{m}$ with a uniform distribution.
- $\mathbf{k}$: elastic spring coefficient. Range: $1 \cdot 10^{3} - 1.5 \cdot 10^{-4}\ \frac{N}{m}$ with a uniform distribution.

With reference to the description presented above, the number of parameters is set to *r=3* and the number of samples consequently. The samples are drawn randomly from the probability distribution for each parameter, which is set as uniform in this case. The results from the sensitivity analysis, namely the overview results and the results from the correlation analysis, are presented in Fig. 2.24 and 2.25. The most influential parameter is the elastic spring coefficient. This is not surprising as it determines

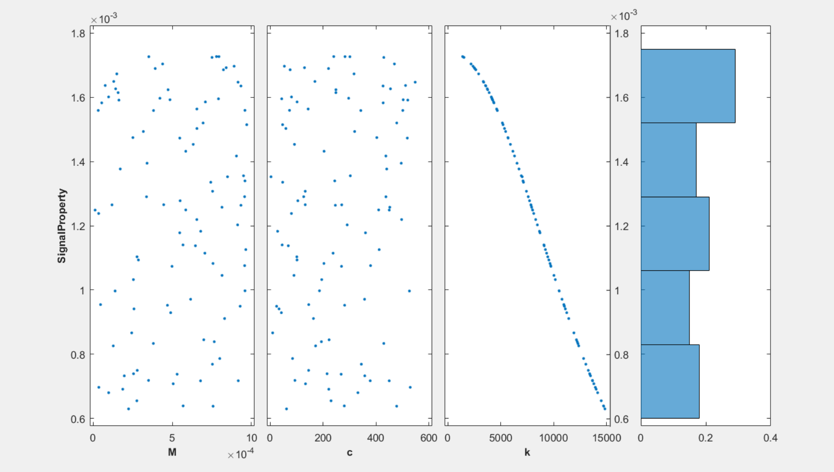

Figure 2.24: Overview of the scatter plots for different dynamics parameters. On the right the number of results for different ranges of mass flowrate are reported.

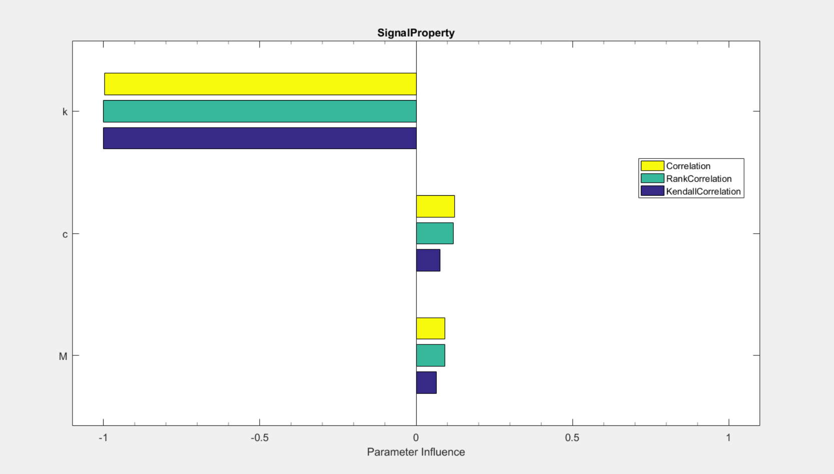

Figure 2.25: Parameters influence assessed by correlation analysis.

the steady-state behaviour of the moving plunger dynamics. Again, the ultimate position of the plunger is determined by the equilibrium between the magnetic force and the elastic force. The stronger the spring, the more the plunger is moved toward the fluid channel, squeezing the equivalent outlet area and delivering a lower flow rate. The other parameters are not influencing the final flowrate, but they might play an important role in the transient phase, determining for instance the rise and settling time.

2.4.5. Comprehensive Sensitivity Analysis

As mentioned above, the sensitivity analysis has been split into different relevant parameters subgroups to better understand the dependency for each domain. Nevertheless, it is important to put the above results into the general perspective of a model dependent on all the listed parameters in Tab. 2.6. The approach is exactly the same as described above and the input samples are generated with the same criteria. Fig. 2.26 summarizes the results for the comprehensive analysis.

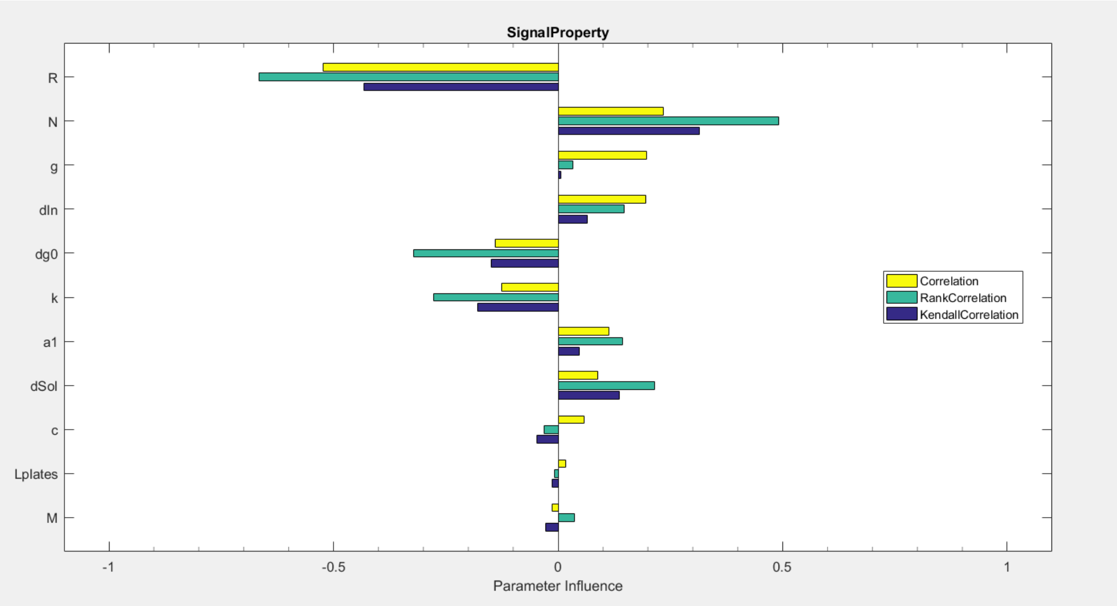

Figure 2.26: Correlation results for the sensitivity analysis comprising all the input parameters present in the model.

With reference to the description presented above, the number of parameters is set to *r=11* and the number of samples consequently. The samples are drawn randomly from the probability distribution for each parameter, which is set as uniform in this case. The results of the correlation analysis show how the set of parameters presents both positive and negative correlation. The intermediate results from the sensitivity analysis for each sub-group is respected in the hierarchy. It is interesting to note that the electric parameters are the most influential in the comprehensive analysis. The reason lies in the fact that the two electric parameters contribute to determine the actuation current of the valve. The current is responsible for establishing the magnetic force that pulls the plunger and opens the valve. Given that the magnetic force is the real actuation force, and that the mass flowrate is linked to the aperture of the valve, the considerable influence of the electric parameters is justified.

The sensitivity analysis was performed to assess the influence of each parameter on the output of the model. On one hand, the influence of each parameter is investigated and analyzed in light of the uncertainty that the chosen value may have. For instance, it is really hard to determine the inner structure of the micro-valve and the magnetic parameters are set based on reasonable considerations. Since the correlation between, for example, the solenoid diameter and the output mass flowrate is low, one can safely assume that there is not much improvement in the overall accuracy by determining accurately its size. Even by changing the diameter by one order of magnitude, namely from *1 mm* to nearly *10 mm* the overall output mass flowrate is not influenced significantly. Furthermore, the analysis represents also a reliable tool to define the guidelines to tune the model to resemble as adherently as possible the behaviour of a real device. For example, the elastic spring constant of the device is usually not found in the datasheet and it is hard to determine it from inspection. Hence, given its significant correlation, as shown in Fig. 2.24, with the simulation outcome and the uncertainty of its value, it could be used to tune the model to meet as much as possible the experimental data. For instance, by changing the elastic constant by a factor of *10*, the output mass flowrate is reduced by a factor of *2*.

Another important remark is that for the less influential parameters the correlation delivers different results, namely positive and negative, depending on the type of data ranking utilized. This means that the true impact of the parameter is not determined and its influence should be neglected.

2.5. Controller design

The design of the controllers is a fundamental task in order to be able to control the mass flowrate within the feeding channels, and hence the thrust. Two controllers, namely PID (proportional-integral-derivative) and SMC (sliding mode control), are designed and tested using the models developed.

The ON/OFF micro-valves are not designed to allow the regulation of the outlet flowrate. Nevertheless, whenever the switching between ON/OFF is faster than the system's dynamics, the system reacts to the average of the discretized output, yielding a value of the flowrate dependent on the ratio between ON time and OFF time. For this reason, the ON/OFF micro-valve is actuated using PWM voltage signal, which indeed actuates and de-actuates the valve at high frequency. This allows a continuous control, where the signal duty cycle is adjusted continuously to meet the commanded set-point. An important concept in PWM actuation is the *duty cycle*. It is defined as the ratio between the ON time and the PWM period:

$$DC = \frac{t_{ON}}{t_{ON} + t_{OFF}} = \frac{t_{ON}}{T_{PWM}} = t_{ON} \cdot f_{PWM} \tag{2.48}$$

where t_{ON} is the time the valve is actuated, t_{OFF} is the time the valve is de-actuated and f_{PWM} is the frequency of the PWM signal. The selection of the frequency is bounded by two different phenomena: the upper limit is set by the hardware and the physical limitations at which the valve can be switched ON and OFF, the lower depends on the dynamics of the system and in particular on the time scale of it. The slower the system reacts, the easier the averaging process is, hence preventing the system to work with a discretized variable, the flowrate in this case. Based on the analysis shown in section 2.5.1 and the considerations above, the frequencies selected for the study are $f_1 = 250\ Hz$ and $f_2 = 500\ Hz$.

The simplest control strategy is based on PID (*Proportional-Integral -Derivative*) controllers. The standard form of the control can be expressed as follows according to [53], where *e(t)* is the error in time:

$$u(t) = k_p e(t) + k_i \int_0^t e(\tau) d\tau + k_d \frac{de(t)}{dt} \tag{2.49}$$

in the time domain. By considering the Laplace representation of the controller C:

$$C(s) = K_P \cdot \left(1 + \frac{1}{T_I s} + T_D s\right) \tag{2.50}$$

where K_P is the proportional gain, T_I is the integral time constants and T_D is the derivative time constant.

Another option to perform the control with a ON/OFF device, such as the valve used in this work, is the SMC (*Sliding Mode Control*). The SMC consist on a discontinuous control that brings the system dynamics to a sliding surface, which sets the reference for the control action. A thorough description of the method is given in section 2.5.7.

The following section presents the control concepts developed and analyzed in the controller design phase. Section 2.5.1 deals with a preliminary frequency response analysis to characterize the system response to signal of different frequencies. Even though the valve is generally driven by DC power supply, such analysis is critical in light of PWM control, since it is a periodic non-continuous signal. Section 2.5.2 introduces a useful mathematical tool used to design the PID controllers. Section 2.5.3 shows the simulated dependency of the mass flowrate on the duty cycle. Sections 2.5.4, 2.5.5 and 2.5.6 describe the approaches adopted for gain tuning and the comparison between the different tuning methods. Finally, section 2.5.7 describes the SMC control strategy.

2.5.1. Frequency Response

A standard approach to analyze the behavior of a dynamical system is to assess the different responses to harmonic input signals at various frequencies fed into the system. In case the system is linear, the response is fully described by the frequency response transfer function, which allows to determine analytically the behaviour of the system for all the input frequencies. The theory, on which such analysis is based on, is the existence of the Laplace representation of a general linear system and, in particular

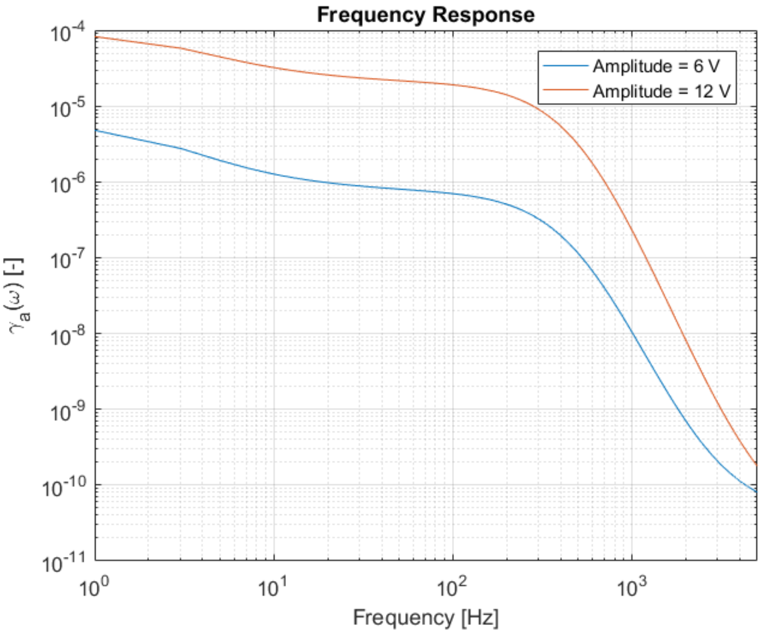

Figure 2.27: Bode plot for frequency response analysis for two amplitudes of the input voltage signal. The analysis is based on Pavlov work [6].

of its transfer function [6]. The transfer function allows to determine the steady-state solution of any complex harmonic input signal. An effective way to visualize the results of the frequency analysis is the *Bode* plot. Such plot is basically a graphical representation of the amplification that an input signal experiences through the system at different frequencies [6].

Nevertheless, this method is not suitable for nonlinear systems, since the Laplace transformation is generally not valid for such systems [6]. However, several researchers have investigated methods to overcome this shortcoming. According to Pavlov [6], it is possible to extend the frequency response functions of linear systems to nonlinear systems. In particular, a method to obtain the equivalent Bode diagram for nonlinear systems is presented. Given an harmonic input signal $a \cdot sin(\omega t)$ with amplitude a and angular frequency ω, the maximum absolute value of the steady-state output can be denoted as $B(\omega, a)$. The *amplification gain* is introduced as:

$$\gamma_a(\omega) := \frac{B(\omega, a)}{a} \tag{2.51}$$

which is a function of both the frequency and the amplitude, unlike in the linear case where the system gain is independent of the input signal amplitude. Eq. 2.51 represents the analytic expression of the Bode plot for nonlinear systems. Indeed, in a simulation-based analysis, the system is excited with harmonic signals and the steady-state output is registered. The values for different frequencies and one amplitude are gathered to reconstruct the Bode plot. Using such plot, insights on the stability and frequency-dependent behaviour of the system can be drawn.

The voltage signal fed into the system represents the input of the micro-valve system. For the frequency response analysis two amplitude are used, namely $6\ V$ and $12\ V$. Again, the objective of this section is to assess the frequency range that can be used when the micro-valve is operated with PWM. Fig. 2.27 shows the results for both the amplitudes. Fig. 2.27 shows a similar behavior between the two cases, beside the absolute value of the amplification gain. The curve resembles the case of a 1^{st} order linear system. A cut-off frequency around $\sim 800\ Hz$ is present. The cut-off frequency is a boundary value in the frequency response of a system at which the response starts reducing with respect to the unobstructed output. For this reason, the available frequencies that can be adopted shall be below the cut-off. In the following analysis, two PWM frequencies are selected, namely $f_1 = 250\ Hz$ and $f_2 = 500\ Hz$. The frequencies have been chosen exactly as these two values due to an experimental consideration: the board used to generate the PWM voltage signal has two built-in frequencies, *250* and *500 Hz* available at the so-called ”PWM pins”. This does not mean that no other frequencies can be generated, as explained in Chapter 3, but that the most stable signal can be generated at these two frequencies, hence the analysis is carried out for such values. The reason why low frequencies are not taken into account is only regarding the PWM actuation and the objective of having the system reacting solely to the averaged output. Nevertheless, if a chattering behaviour is accepted, lower frequencies may be accepted. The result shown in Fig. 2.27 is compatible to what Cajetinac reports in his research [54]. The comprehensive list of parameters used to perform the frequency response analysis is shown in Fig. 2.7.

Table 2.7: Comprehensive list of the parameters set in the analytical model to run the simulations for frequency analysis.

Parameter	Value
Plunger Mass [mg]	0.8
Elastic Spring Constant [$\frac{N}{m}$]	10^4
Viscous Coefficient [$\frac{N \cdot s}{m}$]	500
Coil Resistance [Ω]	31
Coil Turns [-]	1000
Δp [bar]	5
Inlet Diameter [mm]	1

Parameter	Value
Solenoid Diameter [mm]	5
Solenoid Length [mm]	20
Initial Gap Height [m]	10^{-8}
ρ_{H2O} [$\frac{kg}{m^3}$]	1000
μ_{H2O} $[Pa \cdot s]$	0.001
Voltage Amplitude[V]	6-12
Frequency Range [Hz]	0-5000

2.5.2. Linearization

Before proceeding with the controller design, an important mathematical process is worth to be explained. The controller design, especially if PID-based, takes much advantage from the linearity of the system. Indeed, many tuning methods for the PID gains are developed based on the knowledge of the transfer function in the Laplace domain. For nonlinear systems, such analysis cannot be performed and tuning the simple PID gains can be done solely by experimental methods. Nevertheless, if the process to be controlled has a limited output range with respect to the model overall output space, linearization around the operating point can be used to be able to apply all the theory developed for the linear systems. According to Qiu [49], a point $(u_0, \mathbf{x}_0, y_0)$ is said to be an operating point of the system if:

$$
\begin{aligned}
0 &= f(\mathbf{x_0}, u_0) \\
y_0 &= g(\mathbf{x_0}, u)
\end{aligned}
\tag{2.52}
$$

which means that, if the system has $\mathbf{x_0}$ initial condition and a constant input u_0 then the output will stay constantly at y_0. If a modified set of variables is introduced:

$$
\begin{aligned}
\tilde{u} &= u(t) - u_0 \\
\tilde{\mathbf{x}} &= \mathbf{x}(t) - \mathbf{x_0} \\
\tilde{y} &= y(t) - y_0
\end{aligned}
\tag{2.53}
$$

the equivalent linearized system can be written as:

$$
\begin{aligned}
\dot{\tilde{\mathbf{x}}} &= \mathbf{A}\tilde{\mathbf{x}}(t) + \mathbf{b}\tilde{u}(t) \\
\tilde{y}(t) &= \mathbf{c}\tilde{x}(t) + d\tilde{u}(t)
\end{aligned}
\tag{2.54}
$$

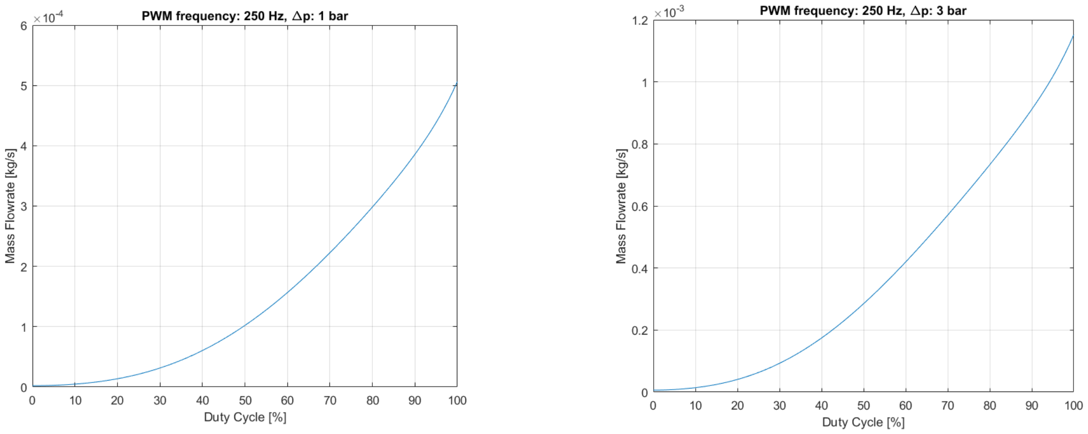

Figure 2.28: Outlet mass flowrate for different duty cycle. PWM frequency is set to 250 Hz and the pressure drop across the valve is 1 bar and 3 bar.

where the matrices can be calculated:

$$
\begin{aligned}
\mathbf{A} &= \frac{\partial f}{\partial \mathbf{x}}\bigg|_{\substack{\mathbf{x}=\mathbf{x_0}\\ u=u_0}} = \begin{bmatrix} \frac{\partial f_1}{\partial x_1} & \cdots & \frac{\partial f_1}{\partial x_n} \\ \vdots & \ddots & \vdots \\ \frac{\partial f_n}{\partial x_1} & \cdots & \frac{\partial f_n}{\partial x_n} \end{bmatrix}, \\
\mathbf{b} &= \frac{\partial f}{\partial u}\bigg|_{\substack{\mathbf{x}=\mathbf{x_0}\\ u=u_0}} = \begin{bmatrix} \frac{\partial f_1}{\partial u} \\ \vdots \\ \frac{\partial f_n}{\partial u} \end{bmatrix}, \\
\mathbf{c} &= \frac{\partial g}{\partial \mathbf{x}}\bigg|_{\substack{\mathbf{x}=\mathbf{x_0}\\ u=u_0}} = \begin{bmatrix} \frac{\partial g}{\partial x_1} & \cdots & \frac{\partial g}{\partial x_n} \end{bmatrix}, \\
d &= \frac{\partial g}{\partial u}\bigg|_{\substack{\mathbf{x}=\mathbf{x_0}\\ u=u_0}}
\end{aligned}
\tag{2.55}
$$

2.5.3. Parametric Study for different DC

In order to characterize the micro-valve's behaviour for different duty cycle and different frequencies, a simulation-based parametric study was performed. Specifically, simulations have been made sweeping the operating duty cycle from 0 to 100 %, for a given frequency. Moreover, simulations for 1 bar and 3 bar pressure drop across the valve have been performed to check whether they had a strong influence on the system output. Fig. 2.28 shows the results for $f_1 = 250\ Hz$, whereas Fig. 2.29 for $f_2 = 500\ Hz$. All the plots show a similar trend, which might be approximated with a parabolic curve. This behaviour makes it harder for the controllers to regulate the flowrate by adjusting the duty cycle, given that the sensitivity to a change in the duty cycle is dependent on the actual state of the control variable. Not many research paper have investigated and characterized valves' behaviour for different duty cycles, Pipan and Herakovic [55] analyzed the air volume flow of a PWM-controlled fast-switching pneumatic valve. The differences with the work hereby presented are multiple, starting from the operating mean and the actuation principle is that of a pneumatic valve. Although not fully compliant with the system studied in this thesis, it is possible to understand how the relationship between output flowrate and duty cycle is nonlinear and that the pressure drop across the valve affects the response of the system.

2.5.4. Experimental Gain Tuning

The process of tuning the controllers' gain may become complex when the system presents nonlinearities [7]. Indeed, when the transfer function cannot be written, the analytic methods to tune the closed-loop PID gains are no longer valid. One solution, as described in section 2.5.2 is to linearize the system around an operating point and work out the analysis on the linearized transfer function.

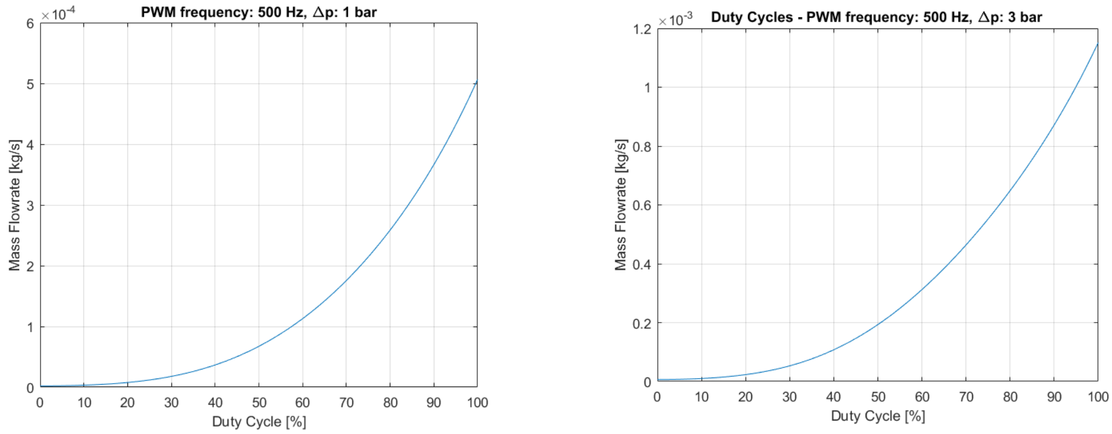

Figure 2.29: Outlet mass flowrate for different duty cycle. PWM frequency is set to 500 Hz and the pressure drop across the valve is 1 bar and 3 bar.

On the other hand, experimental methods have been developed since the early years of control engineering. The most famous and effective approach is the one proposed by Ziegler and Nichols. Actually, Ziegler and Nichols developed two slightly different methods: one based on the step response of the system, whereas the second deals with the characterization of the closed-loop process dynamics. However, given the peculiar actuation method of the system, the frequency method, or closed-loop method [7] [49], is not suitable for tuning the gains in this scenario. There have been many modifications to these experimental methods: an effective approach to deliver a better damped closed-system has been proposed by Chien, Hrones and Reswick [7] and relies on the step response of the open-loop system.

Ziegler - Nichols: Step Response Method The first Ziegler-Nichols method is based on the analysis of the open-loop step response of the system [7] [49]. The response is described by two parameters a and L. L is found by drawing the tangent to the curve at the point where the slope has its maximum and intersecting such line with the horizontal axis. The parameter a, on the other hand, is the intersection between the vertical axis and the same tangent line. Two auxiliary parameters are introduced to make the graphical identification of the features. The parameter K is the steady-state value of the output, whereas τ is the time coordinate correspondent to the intersection between the steady-state line and the tangent. The relationship between the listed parameters is:

$$a = \frac{KL}{\tau} \tag{2.56}$$

Fig. 2.30 shows a schematic of the parameters. The controller gains can be derived according to Tab. 2.8. In order to develop the concepts described above, a representative dynamics needs to be generated. Simulations for the step response are run for a prescribed duty cycle, the experimental gain tuning procedure is then worked out. Given the large flowrate operating range and the inherent nonlinearities present in the model, it is hard to define a unique representative dynamics for the process. The flowrate range used in the micro-thruster is in the order of milligram-per-second, however, as extensively treated in the experimental Chapter 3, several issues were found in achieving such flowrate with the available hardware. Since the main objective of the thesis is developing a set of methodologies,

Table 2.8: Controller gains for the step response Ziegler-Nichols method [7].

Controller	K_P	T_I	T_D
P	$\frac{1}{a}$	-	-
PI	$\frac{0.9}{a}$	3L	-
PID	$\frac{1.2}{a}$	2L	$\frac{L}{2}$

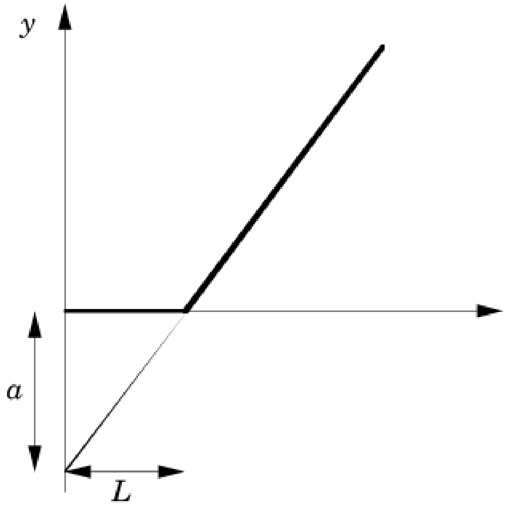

Figure 2.30: Characterization and relevant parameters of the step-response Ziegler-Nichols method [7].

simulations and concepts for controlling the flowrate, it is not critical to develop the controllers just for the required design flowrate for the micro-thruster. Moreover, to validate the concept of controlling the flowrate by adjusting the operational duty cycles, the tests will be made with higher mass flowrates. For this reason, the gains are tuned based on two representative duty cycles for the PWM input voltage signal, namely 20 % and 75 %, which cover a wide range.

The work-flow for determining the PID gains is as follows:

1. Step response simulation is run;
2. Maximum slope point is identified;
3. Tangent line is drawn;
4. The parameters are determined.

The outcome of the simulation is in Simulink and needs to be averaged to remove the inherent scatter behavior due to the PWM actuation. This is done solely to make the determination of the relevant parameters for tuning the gains easier. The identification of all the parameters is rather straightforward and is presented in Fig. 2.31. To test the controllers, a stair-case is commanded as input set-point. Fig. 2.32 and 2.33 show the results for both the gains set. The average of the simulated flowrate follows satisfactorily the commanded input. Nevertheless, the significant variance of the signal around the commanded input is large. This is linked both to the PWM actuation, which is inherently discretized (completely open or completely closed), and also to the large proportional gain, which degrades the stability of the system [7] [53]. In addition the control variable, namely the duty cycle, has a significant oscillatory behaviour in both cases, which may lead to instability of the controller. The overshooting behaviour is nearly absent. The settling time ranges between 10 and 15 ms for both cases. A summary of the PID gains is given in Tab. 2.9.

Table 2.9: PID gains tuned using Ziegler-Nichols step response method.

Tuning	k_p	k_i	k_d
$\frac{mg}{s}$	$1.1 \cdot 10^6$	$3.2 \cdot 10^7$	$9.4 \cdot 10^3$
$10^{-4}\frac{kg}{s}$	$1.1 \cdot 10^4$	$3.1 \cdot 10^5$	87.3

Chien-Hrones and Reswick Method The procedure for tuning the gain according to the Chien-Hrones and Reswick method is very similar to the one proposed by Ziegler-Nichols. In particular, the

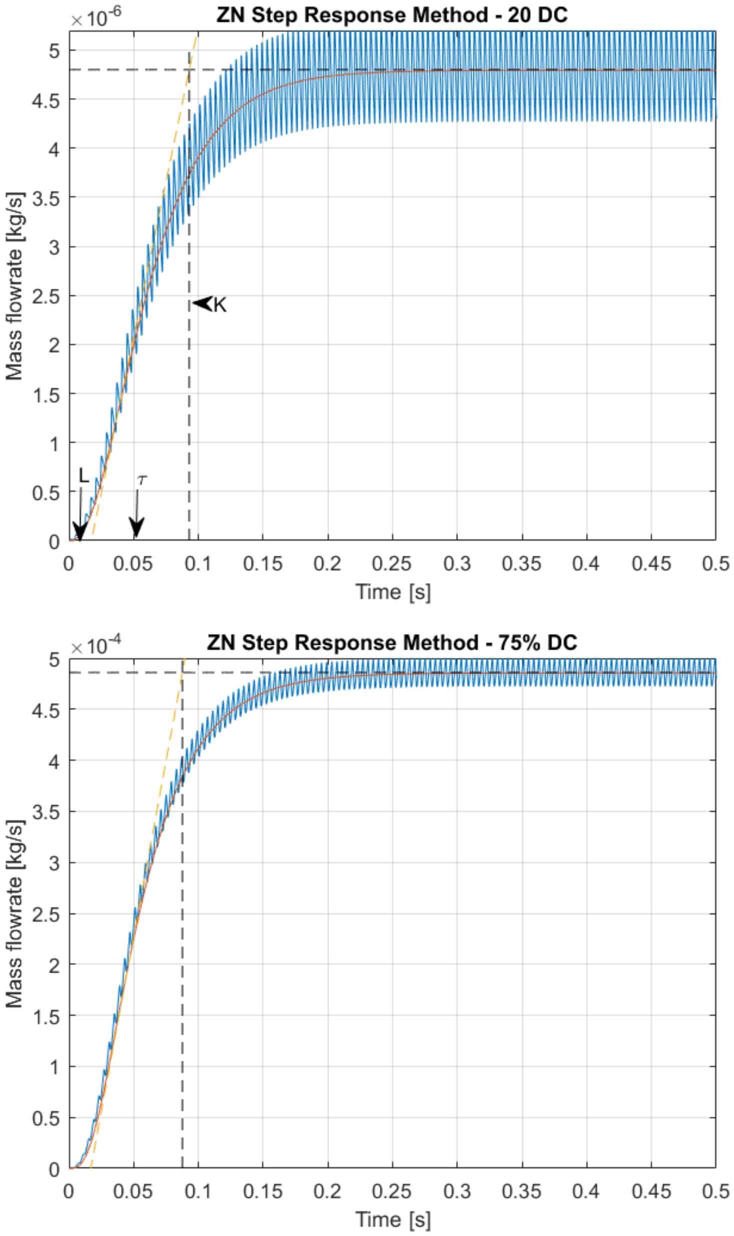

Figure 2.31: Step response for PWM actuation DC = 20 % and DC = 75 %. The parameters for tuning the gains are shown.

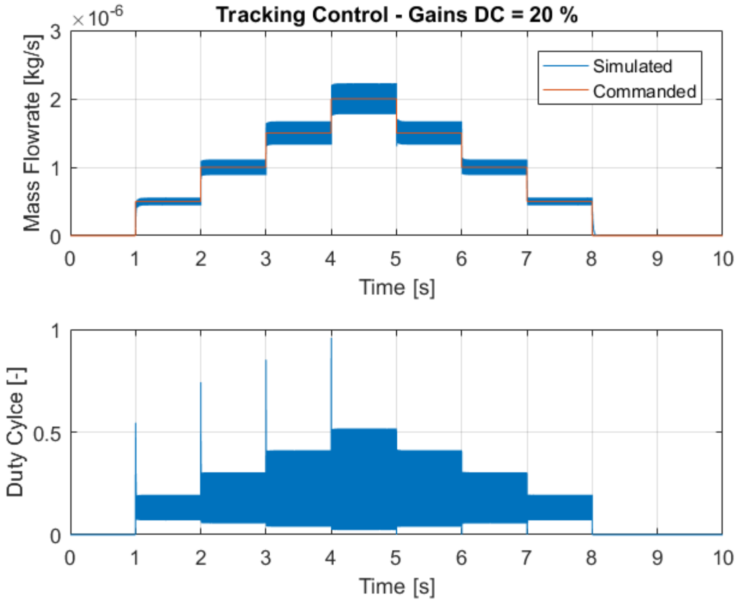

Figure 2.32: Performance of the PID controllers tuned using Ziegler-Nichols method. The flowrate range is [0:2] $\frac{mg}{s}$

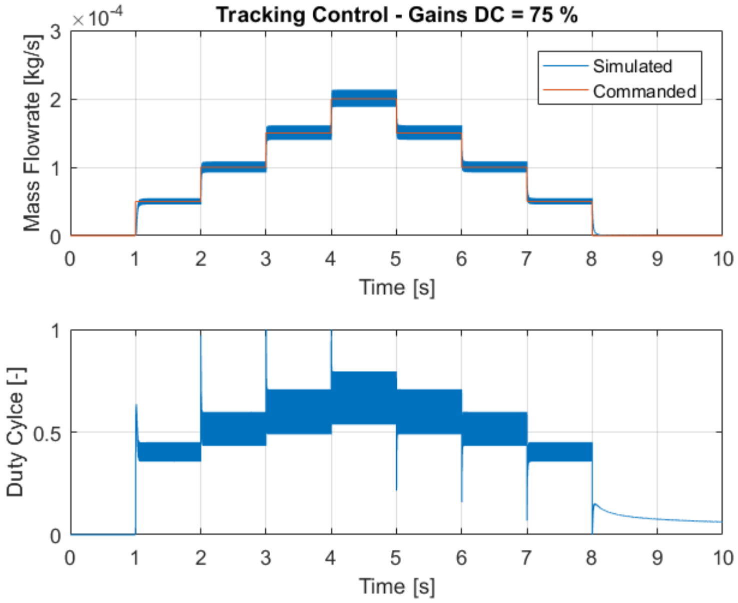

Figure 2.33: Performance of the PID controllers tuned using Ziegler-Nichols method. The flowrate range is [0:0.2] $\frac{g}{s}$

Table 2.10: Controller gains for the step response Chien, Hrones and Reswick method [7].

Controller	K_P	T_I	T_D
P	$\frac{0.3}{a}$	-	-
PI	$\frac{0.6}{a}$	4L	-
PID	$\frac{0.95}{a}$	2.4L	0.42

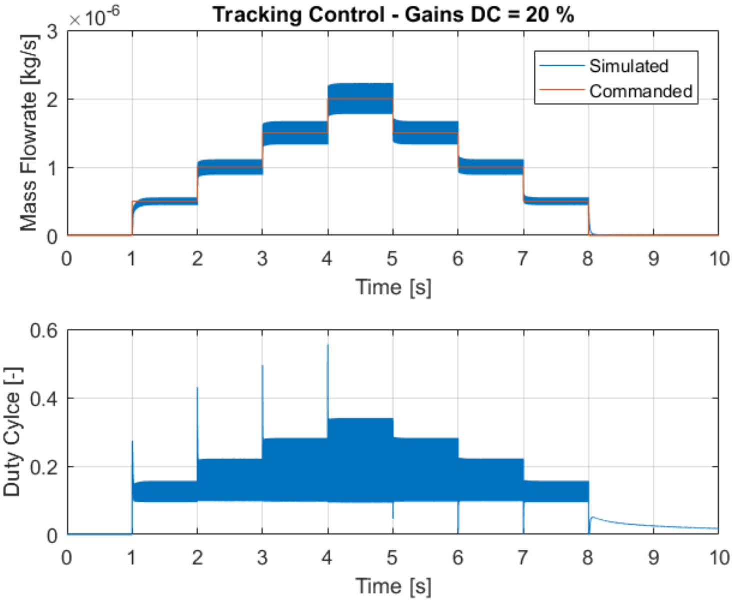

Figure 2.34: Performance of the PID controllers tuned using Chien, Hrones and Reswick method. The flowrate range is [0:2] $\frac{mg}{s}$

parameters necessary for calculating the gains are the same, with the only difference that for this second method a third parameter needs to be determined. T can be calculated as the time difference between the instant at which the output reaches 67% of the steady-state value and the parameter L previously described. Based on these parameters, Tab. 2.10 can be used to determine the gains: The results for the stair-case command are shown in Fig. 2.34 and 2.35. The settling time for both cases increases up to $50\ ms$. However, the proportional action, the integral part as well as the derivative contribution are smaller. Accordingly, the control variable is more stable, reducing the oscillations with respect to the Ziegler-Nichols tuning. The summary of the PID controllers is shown in Tab. 2.11.

Table 2.11: PID gains tuned using Chien, Hrones and Reswick method.

Tuning	k_p	k_i	k_d
$\frac{mg}{s}$	$5.5 \cdot 10^5$	$9.0 \cdot 10^6$	$4.7 \cdot 10^3$
$10^{-4}\frac{kg}{s}$	$5.2 \cdot 10^3$	$9.8 \cdot 10^4$	43.6

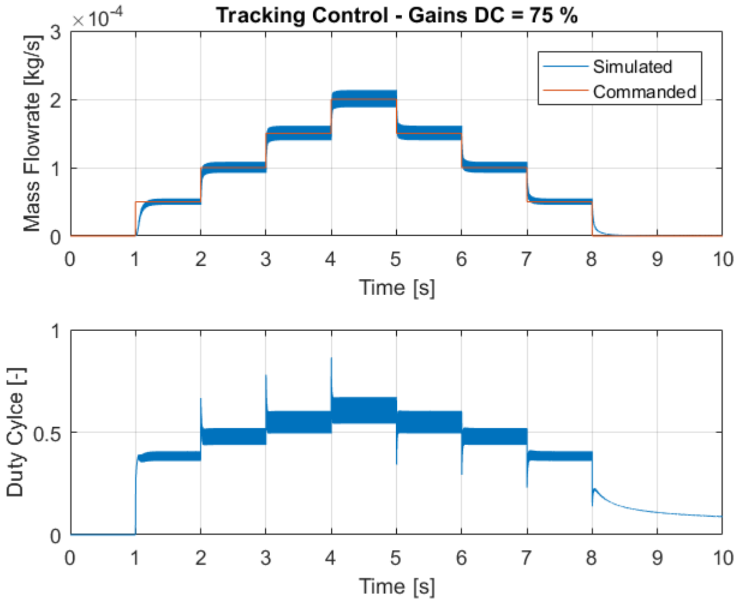

Figure 2.35: Performance of the PID controllers tuned using Chien, Hrones and Reswick method. The flowrate range is [0:0.2] $\frac{g}{s}$

2.5.5. Averaged model

The design of the controller for a PWM-driven micro-valve presents some peculiar challenges. Above all, the system is discontinuous in the input given that the valve is either completely open or closed. A very effective approach, often adopted in literature [56] [57] [58], is to derive an averaged analytic model to create an equivalent model continuous in time of the PWM-controlled valve. This operation yields a system model that is both continuous and affine in the control, making the controller design much simpler.

Consider a nonlinear system as the one presented in Eq. 2.28, which we write in the compact form:

$$\dot{\mathbf{x}} = f(\mathbf{x}, u) \tag{2.57}$$

where $\mathbf{x}$ is the state vector and u is the control input. The control input in a PWM-controlled valve is the voltage, which switches from 0 V to 12 V. To make the analysis easier, consider that the constant $V_{DC} = 12\ V$ does not belong to the control variable but it is indeed a multiplicative constant. Hence, the control input is discontinuous with a binary value of 1 or 0. Since the control is binary, it is possible to distinguish between two different modes, which in turns select a subset of the system dynamics. The dynamics of the system in each mode can be written as:

$$u = 1 \rightarrow \dot{\mathbf{x}} = f_1(\mathbf{x}) \tag{2.58}$$

$$u = 0 \rightarrow \dot{\mathbf{x}} = f_2(\mathbf{x}) \tag{2.59}$$

During each PWM period, the control variable switches between the two modes and the ratio between each mode duration and the PWM period is described by the duty cycle, introduced in Eq. 2.48. Consequently the time-averaged model can be written as:

$$\dot{\mathbf{x}} = \frac{f_1(\mathbf{x}) \cdot t_{ON} + f_2(\mathbf{x}) \cdot t_{OFF}}{T_{PWM}} = f_1(\mathbf{x}) \cdot DC + f_2(\mathbf{x}) \cdot (1 - DC) \tag{2.60}$$

Eq. 2.60 can be further rearranged to make it affine in the new continuous control input variable DC:

$$\dot{\mathbf{x}} = a(\mathbf{x}) + b(\mathbf{x}) \cdot DC \tag{2.61}$$

where $a(\mathbf{x}) = f_1(\mathbf{x})$ and $b(\mathbf{x}) = f_1(\mathbf{x}) - f_2(\mathbf{x})$. The control input, as mentioned, is bounded in the range [0,1]. For the state-space model developed in Eq. 2.28, the two terms are:

$$f_1(\mathbf{x}) = \left\{ \begin{matrix} x_2 \\ \\ \frac{1}{M}\Big(-cx_2 - k(x_1 - x_0) + F_{mag}(x,i) + F_{f,pl}(x) - p_{out}A_{in} \Big) \\ \\ \frac{1}{L(x)}\Big(V_{DC} - x_3\Big(R + x_2 \frac{dL(x)}{dx} \Big)\Big) \\ \\ -\frac{12\mu}{\rho(x_1+x_{u0})^2} x_4 + \frac{\Delta p_{\zeta}}{\rho L_{plates}} \end{matrix} \right\} \tag{2.62}$$

$$f_2(\mathbf{x}) = \left\{ \begin{matrix} 0 \\ \\ 0 \\ \\ \frac{1}{L(x)} \cdot V_{DC} \\ \\ 0 \end{matrix} \right\} \tag{2.63}$$

Using the continuous and affine system, the design process for the controllers is simplified especially if the linearization is performed. As for the experimental methods, a representative dynamics has to be chosen to perform the linearization, namely the control input u_0 described in section 2.5.2. For reasons that will be explained in chapter 3 two operating points are taken into account, or rather, two order of magnitude for the outlet flowrate are considered as operating points. The linearization of the averaged system could be worked out analytically, in principle. Nevertheless, it is much more effective to work out the linearization using the iterative approach implemented in Matlab/Simulink. The PID gains are then estimated by setting the requirements on the response time and the transient behaviour using the *Control System Toolbox* of Matlab/Simulink.

This method is expected to deliver the best results, at least in terms of the simulation. For the dynamics delivering a flowrate in the order of $1\ \frac{mg}{s}$, the system is linearized using a PWM duty cycle of 35%. Note that the duty cycle used hereby is different from that use in the experimental gain tuning approach. The reason is the difference in the model itself, which is now averaged and linear and affine in the control input. If the results from the experimental tuning are taken as baseline, the requirement on the response time can be determined as within the range $[10 - 20]\ ms$. The major concern that was left from the experimental tuning was the robustness of the control, given that the control variable experienced large oscillations. The PID gains yielded by the analysis are shown in Tab. 2.12. Fig. 2.36 shows the tracking behaviour of the simulated outlet flowrate. The settling time is $\sim 7\ ms$, which is satisfactorily. Yet the control variable is not stable and sweeps a large oscillation around the nominal values that reaches up to 10 % in the worst case scenario.

For the dynamics delivering a flowrate in the order of $10^{-4}\ \frac{kg}{s}$, the system is linearized using a PWM duty cycle of 75%. The requirement on the response time is set identically to the previous case, namely $[10 - 20]\ ms$. The PID gains yielded by the analysis are shown in Tab. 2.12. Fig. 2.37 shows the tracking behaviour of the simulated outlet flowrate. The behaviour is more robust than the cases shown in the experimental tuning. This comes with a shortcoming, namely the increase of the settling time. Indeed, in Fig. 2.37 the settling time is $\sim 30\ ms$. On the other hand, the control variable has a stable behaviour and nearly no oscillations are found in it. For all the simulations regarding the PID tuning,

Table 2.12: PID gains tuned using the averaged model.

Tuning	k_p	k_i	k_d
$\frac{mg}{s}$	$2.8 \cdot 10^5$	$2.1 \cdot 10^7$	114.6
$10^{-4}\frac{kg}{s}$	$3.9 \cdot 10^2$	$2.9 \cdot 10^4$	0.15

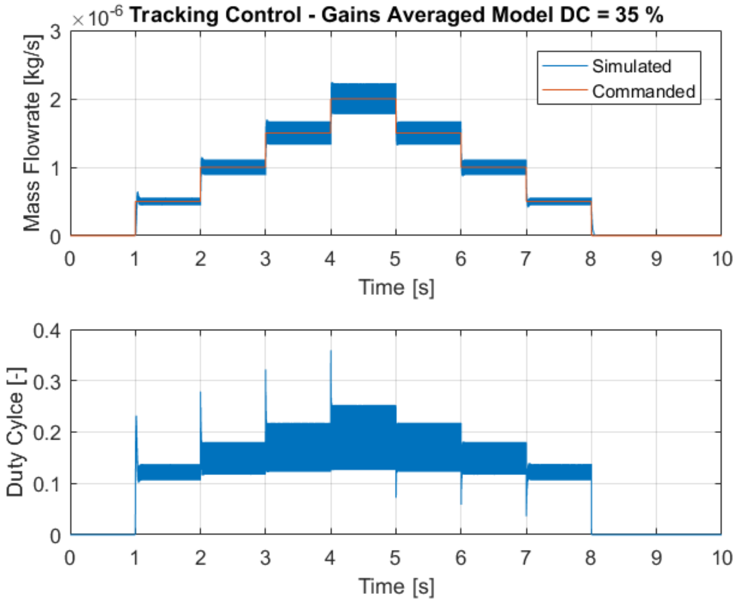

Figure 2.36: Performance of the PID controllers tuned using the averaged model. The flowrate range is [0:2] $\frac{mg}{s}$

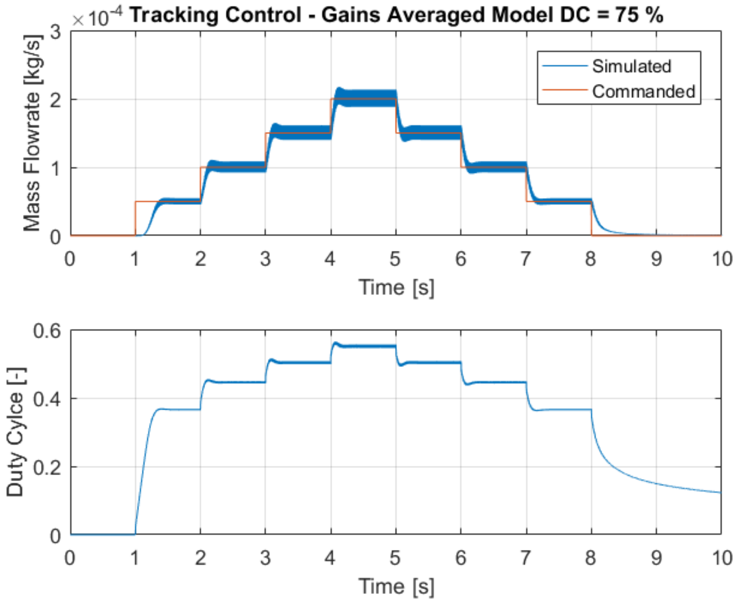

Figure 2.37: Performance of the PID controllers tuned using the averaged model. The flowrate range is [0:0.2] $\frac{g}{s}$

the parameters are set following Tab. 2.13.

Table 2.13: Comprehensive list of the parameters set in the analytical model to run the simulations for the PID tuning.

Parameter	Value
Plunger Mass [mg]	0.8
Elastic Spring Constant [$\frac{N}{m}$]	10^4
Viscous Coefficient [$\frac{N \cdot s}{m}$]	500
Voltage [V]	12
Coil Resistance [Ω]	31
Coil Turns [-]	1000
Δp [bar]	5

Parameter	Value
Inlet Diameter [mm]	1
Solenoid Diameter [mm]	5
Solenoid Length [mm]	20
Initial Gap Height [m]	10^{-8}
ρ_{H2O} [$\frac{kg}{m^3}$]	1000
μ_{H2O} $[Pa \cdot s]$	0.001
f_{PWM} [Hz]	250

2.5.6. PID Gains Tuning Comparison

The different methods to tune the PID gains have been presented and discussed in the relevant sections. The methods have been split into experimental and numerical, as the former, namely Ziegler-Nichols method and Chien-Hrones-Reswick, require a simulation to determine the gains, whereas the latter is based on the mathematical model of the system.

A typical strategy to compare the efficiency of different controllers, or different tuning laws for the same controller, consists in defining indices, which are representative of the controller's performance in terms of the error variable. The three idices are:

- The *Integral Squared Error* (ISE) integrates the square of the error over time:

  $$ISE = \int e^2 dt \tag{2.64}$$

  the effect of the integral is to enlarge those errors that are already significant.

- The *Integral Absolute Error* (IAE) integrates the absolute value of the error:

  $$IAE = \int |e| dt \tag{2.65}$$

- The *Integral Time-weighted Absolute Error* (ITAE) integrates the absolute error multiplied by the time over time:

  $$ITAE = \int t \cdot |e| dt \tag{2.66}$$

  the effect of the integration is that errors distant in time from the start of the response are valued more than those at the beginning.

The indices must be calculated in the same exact simulation conditions, namely the commanded set-point and the time span: the test-case used in sections 2.5.4 and 2.5.5 is taken as reference. However, beside the above-mentioned indices, the behaviour of the control variable is fundamental to monitor, especially in light of the experimental implementation.

Tab. 2.14 reports the three indices for the different PID tuning laws and operating point.

Table 2.14: Comparison between PID controllers: ISE, IAE, ITAE for the different tuning laws. On the left, the reference order of magnitude is $\frac{mg}{s}$, whereas on the right $10^{-4}\frac{g}{s}$.

$\frac{mg}{s}$	ISE	IAE	ITAE
ZN	$6.15 \cdot 10^{-14}$	$5.23 \cdot 10^{-7}$	$2.37 \cdot 10^{-6}$
CHR	$6.38 \cdot 10^{-14}$	$5.36 \cdot 10^{-7}$	$2.43 \cdot 10^{-6}$
Avg	$6.41 \cdot 10^{-14}$	$5.31 \cdot 10^{-7}$	$2.36 \cdot 10^{-6}$

$10^{-4}\frac{g}{s}$	ISE	IAE	ITAE
ZN	$3.27 \cdot 10^{-10}$	$3.66 \cdot 10^{-5}$	$1.65 \cdot 10^{-4}$
CHR	$4.70 \cdot 10^{-10}$	$4.21 \cdot 10^{-5}$	$1.90 \cdot 10^{-4}$
Avg	$1.37 \cdot 10^{-9}$	$6.46 \cdot 10^{-5}$	$2.84 \cdot 10^{-4}$

The results of the analysis for the different PID tuning strategies shows that they are compatible in terms of the indices introduced above. For the lower order of magnitude, namely $\frac{mg}{s}$, the integral errors are close with the largest difference of $3\ \%$ between the averaged model method and the Ziegler-Nichols in the ISE. Overall the smallest errors are achieved by the averaged model and the Ziegler-Nichols strategy: nevertheless, the average model is preferred since the control variable is much more stable throughout the simulation, see Fig. 2.36 compared to Fig. 2.32.

The results of the tuning for the higher order of magnitude, namely $10^{-4}\frac{g}{s}$, show that the Ziegler-Nichols method delivers the most performing controller, in terms of the above-mentioned indices. Indeed, the ISE, IAE and ITAE for the average model method are $76\ \%$, $43\ \%$ and $42\ \%$ higher, respectively. Such result is rather countertrend with respect to the considerations made in section 2.5.4 and 2.5.5. However, the reason why the average model method gives a poor performance in terms of the indices is linked to the larger response time, hence slower response, that the system has. With reference to Fig. 2.33 and 2.37, the response time is clearly faster in the first case and the oscillations of the process variable are comparable. Nevertheless, the major concern with the Ziegler-Nichols tuned PID is that the control variable, namely the duty cycle, has a truly unstable behaviour. In the experimental tests, the oscillations of the control variable were critical for the effectiveness of the control-loop; hence, the averaged model method was taken as reference for the PID gains in the actual set-up, at the cost of a reduced performance in terms of response time.

2.5.7. Sliding Mode Control

Sliding mode control (SMC) is a very effective control strategy, due to its simplicity in the design and invariance to process dynamics characteristics [59]. It is beyond the scope of this text to describe the method mathematically, thus it is suggested to refer to specialized book to obtain more information [59]. However, a brief outline of the procedure is given.

SMC control drives the state of the system onto a prescribed surface within the state space, which is called *sliding surface*. At the time the surface is reached by the system, the controller guarantees that the system stays close to the sliding surface. Thus, the SMC is a controller that comprises two parts:

- Design of the sliding surface;
- Selection of the control law to keep the system onto the sliding surface.

Given the averaged state space model in Eq. 2.61, 2.62 and 2.63, the control objective is to track a commanded set-point. The most significant variable is, obviously, the output error $e = \dot{m} - \dot{m}_{comm}$ that we want to vanish in a reasonable transient time. As explained in Chapter 3, the process variable can be changed to the thruster pressure. Nevertheless, the process error is taken as reference for building the sliding surface.

Sliding Surface Many researchers in literature used SMC to control pneumatic actuators [57] [60] [61] [62]. Very often the sliding surface σ_{SMC} is built on the error variable and its derivatives:

$$\sigma_{SMC} = \sigma_{SMC}(e, \dot{e}, \ddot{e}, ..., e^{(k)}) \tag{2.67}$$

The vanishing of the sliding surface $\sigma = 0$ should yield a stable differential equation, whose solution all tend to zero. A typical choice for the sliding surface is given by:

$$\sigma_{SMC} = \left(\frac{d}{dt} + p\right)^{k} \cdot e \tag{2.68}$$

where p is chosen arbitrarily, whereas $k = r - 1$ where r is the relative degree between input-output in Eq. 2.28. For such system state-space model, the relative degree is 3, hence $k = 2$.

Control Law There are several different approaches to design the control law. They can be categorized into:

- first-order (standard) sliding mode control
- high-order sliding mode control

The most simple design is the first-order sliding mode control, and in particular a discontinuous control across the manifold $\sigma = 0$ written as follows [59]:

$$u = -|U| sign(\sigma_{SMC}) = -|U| sign\left(\ddot{e} + 2p\dot{e} + p^2 e\right) \tag{2.69}$$

The implementation is suitable for actuators that can be switched ON and OFF very fast, similarly to PWM applications. Nevertheless, the discontinuous control is significantly affected by the sampling time, the rate at which the controller is updated. Hejrati [57] claims good results using a sampling time of $1\ ms$. As explained in Chapter 3, such sampling period is not achieved. Theoretically, the performance of the sliding mode controller are superior with respect to PID control, as can be derived from the good results in Fig. 2.38. However, when a finite sampling time is introduced the controller is unable to perform the task successfully, as shown in Fig. 2.39. The sampling time has been set to 40 ms, based on the results described in Chapter 3. The tracking of the commanded input is not reached due to the fast dynamics of the micro-valve; the sampling time is too large to prevent the system to react to the fully open-closed condition that occurs in Fig. 2.39.

To overcome such shortcoming, a continuous control should be implemented in the same fashion of the PID controllers. The duty cycle can be varied continuously within the operating range of 0 to 100%.

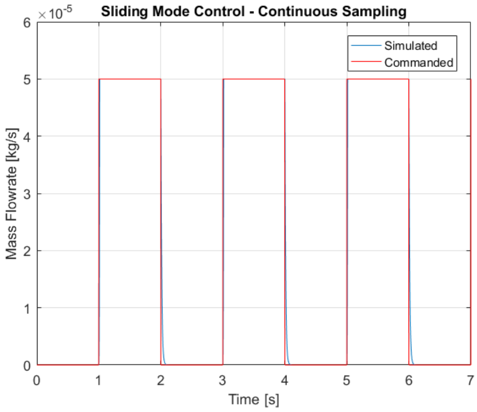

Figure 2.38: Sliding mode control using the control law in Eq. 2.69. The simulation is run assuming no hardware limitations, both in sampling time and switching frequency.

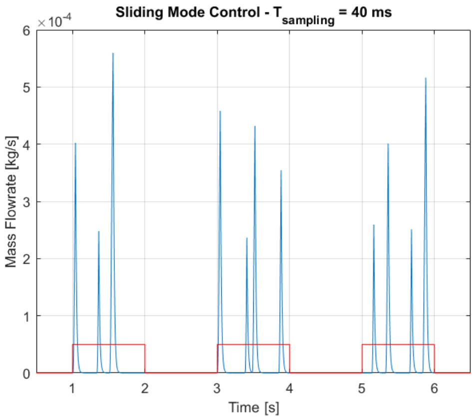

Figure 2.39: Sliding mode control using the control law in Eq. 2.69. The simulation is run assuming a maximum switching frequency of 500 Hz and a sampling rate of 40 ms.

If the duty cycle was used as control variable, it would have a constant value during the sampling period, before being updated by the controller. Although the controller is updated at the same sampling frequency as before, the valve would be operated with a certain PWM duty cycle for one sampling period and it would prevent the valve to react directly to a fully open-fully closed behavior, enabling a successful control. Nevertheless, most algorithms that yield a continuous sliding mode control are valid only for systems with relative degree equal to one. For such system, it is rather straightforward to manipulate the equations and the state-space model to obtain the control law [59].

As said, the shortcoming of opening the valve for a long time, namely the sampling period of the sensors signal, may be solved by the continuous control based on the sliding surface. Nevertheless, as explained in Chapter 3, even the minimum duty cycle yields a sufficient flowrate to bring the thruster to the maximum operating point. An hybrid method is developed based on the insights that the first tests with the complete systems gave. The opening of the valve causes the pressure to rapidly increase, unlike the opposite process, occurring when the valve is closed. The difference between the rise and fall of pressure inside the thruster, for the opening and closing of the valve respectively, enables the use of a modified ON/OFF control strategy based on the sliding mode surface. The opening time of the valve should be limited to the minimum, whereas the time the valve is closed should be extended as much as possible to reduce the averaged flowrate flowing through the micro-thruster. In this way, the discretization is much more relevant and the packages of fluid are delivered at a lower rate. Even though the frequency is reduced, the pressure inside the thruster still react to the averaged flowrate. The minimum opening time of the valve is limited by the hardware to $t_{min} = 0.1\ ms$. The control is then computed at the next reading from the sensors, yielding a control frequency equal to the sampling one. The control law is then developed as follows:

$$\begin{aligned}&\text{if } sign(\sigma_{SMC}) < 0 \ \rightarrow \begin{cases} u = 1, \ 0 < t < t_{min} \\ u = 0, \ t_{min} < t < t_s \end{cases} \\ &\text{if } sign(\sigma_{SMC}) > 0 \rightarrow u = 0\end{aligned} \tag{2.70}$$

where t_{min} is the minimum spike time, t_s the sampling rate of the sensors and the control variable indicates a binary value in reference to the actuation or de-actuation. The control scheme is repeated with a period equal to the sampling one. The control law is based on experimental results and is suitable solely for the control of the complete micro-propulsion system, using the thruster pressure as a process variable and the DC voltage signal as the control variable. The results of the simulation of the control law is compared to the experimental data in Chapter 4.

All the parameters used in the simulation of the SMC scheme are listed in Tab. 2.15.

Table 2.15: Comprehensive list of the parameters set in the analytical model to run the simulations for the SMC control law.

Parameter	Value
Plunger Mass [mg]	0.8
Elastic Spring Constant [$\frac{N}{m}$]	10^4
Viscous Coefficient [$\frac{N\cdot s}{m}$]	500
Voltage [V]	12
Coil Resistance [Ω]	31
Coil Turns [-]	1000
Δp [bar]	5

Parameter	Value
Inlet Diameter [mm]	1
Solenoid Diameter [mm]	5
Solenoid Length [mm]	20
Initial Gap Height [m]	10^{-8}
ρ_{H2O} [$\frac{kg}{m^3}$]	1000
μ_{H2O} [$Pa \cdot s$]	0.001
p [-]	1000
t_s [ms]	0-40
t_{min} [ms]	0.1

2.6. Complete Model Simulation

The micro-propulsion system comprises several parts: the propellant tank, the micro-valve, the micro-thruster and the driving electronics as well as the control system, currently implemented on the computer. The purpose of this thesis, as explained in Chapter 1 is to regulate the thrust by controlling the flowrate flowing in the feeding lines. For this reason, the major part of the work focused on developing analytic models for the micro-valve, which will serve for future reference in manufacturing and design, as well as in testing the actual hardware currently available. However, the micro-valve model needs to be integrated in the complete model of the micro-propulsion system in order to simulate its comprehensive behaviour. Fig. 2.40 shows the Simulink model of the complete system used in the comprehensive simulation.

Propellant Tank The propellant tank is a pressurized tank containing a given fraction of water. During operation, water is ejected and the pressurized gas, N_2, expands lowering its pressure. The mathematical model puts these two quantities into relation starting from the ideal gas law:

$$pV_{N2} = m_{N2}RT \tag{2.71}$$

where p is the pressure, V is the volume, m_{N2} is the gaseous mass, R is the specific gas constant and T is the temperature. Assuming an isothermal process and taking the derivative in time:

$$\dot{p}V = -p\dot{V} \tag{2.72}$$

where $V = V_{tot} - \frac{m_{H20}}{\rho_{H2O}}$, in which V_{tot} is the total tank volume, m_{H2O} is the mass of water and ρ_{H2O} is the density of the water. Manipulating Eq. 2.72, the derivative of pressure may be written as:

$$\dot{p} = p\frac{\dot{m}_{H2O}}{(V_{tot}\rho - m_{H2O})} \tag{2.73}$$

where $\dot{m}_{H2O}$ is the water mass flowrate flowing in the feeding lines. Eq. 2.73 describes the depressurization of the propellant tank used in blowdown mode, which is most likely to happen in an actual realization for nano-satellites integration.

Vaporizing Liquid Micro-Resistojet The VLM-Vaporizing Liquid Micro-Resistojet is a micromachined chamber which is heated by internal or external microheater to vaporize a liquid flow; the vapor flow is then ejected through a nozzle, producing thrust. Several analytical models have been investigated during the preparatory literature study for this project, as described in Chapter 1. Nevertheless, the model that is used in the simulation simply relies on the ideal gas and rocket equation. This model serves to gather the complete system's equations, hence it is a simple representation of the real VLM device.

The water flows out of the valve with a certain rate, once in the micro-thruster the water is vaporized and builds up the pressure within the chamber. The chamber pressure determines the mass flowrate that is accelerated through the nozzle, according to ideal rocket theory. In the model, three different flowrates are identified:

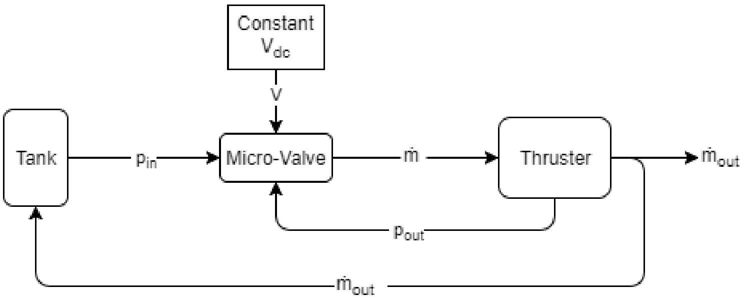

Figure 2.40: Block diagram of the complete uncontrolled micro-propulsion system. The figure shows the key blocks implemented in the Simulink model, which is not reported here for helping the visualization of solely the important blocks.

- $\dot{\mathbf{m}}_1$: water mass flowrate out of the valve
- $\dot{\mathbf{m}}_2$: rate of water vaporization
- $\dot{\mathbf{m}}_3$: vapor flowrate through the nozzle

The difference between $\dot{m}_2$ and $\dot{m}_3$, called $\dot{m}_x$ is the excessive vapor that is trapped inside the chamber and contributes to the building of pressure. The rate of vaporization $\dot{m}_2$ is assumed to be equal to the mass flowrate $\dot{m}_1$ flowing out of the valve. Such assumption neglects the vaporization process, where there can be an unbalance between the water flowing into the micro-thruster and the rate of vaporization, especially during the initial phase. Nevertheless, the steady-state condition should follow closely the above-mentioned assumption, yielding good predictions of the VLM operating conditions. The water vapor inside the microthruster is in saturation condition, thus the process can be considered isothermal and hence the temperature constant in the derivation.

Applying the ideal gas law to the water vapor dwelling inside the microthruster, after some manipulations, the pressure derivative can be written as:

$$\dot{p} = \dot{m}_x \frac{RT_c}{V} \tag{2.74}$$

where p is the pressure, m_x the accumulated vapor in the chamber, T_c the chamber temperature and V its volume. The volume available for the water vapor to expand is assumed to be constant. Nevertheless, visual results of simulations show that liquid water level changes throughout the experiment, slightly varying the volume allocated to the water vapor. Based on the pressure inside the chamber, the mass flowrate through the nozzle can be calculated using the ideal rocket theory, according to Eq. 1.43. Eq. 1.43 becomes:

$$\dot{m}_3 = A_t \frac{\Gamma p}{\sqrt{RT_c}} \tag{2.75}$$

Micro-valve The micro-valve model is here reported just for completeness. The main inputs-outputs of the model are the mass flowrate for a given voltage signal and pressure drop across the valve itself. The pressure at the inlet is delivered by the propellant tank mode. The output mass flowrate is fed into the micro-thruster as explained in the previous paragraph.

2.6.1. Simulation Results - Uncontrolled System

The first simulation has been run without the control system to assess the interfacing between the different blocks of the system. The actuation of the valve is made by a 12 V voltage input. The delivered thrust is calculated from the specific impulse of the micro-thruster $I_{sp} = 100s$ [63]. Furthermore, the simulations are useful to determine the behaviour of the micro-propulsion system to thrust pulses, at which the thruster can be operated. This is done by switching ON/OFF the valve; for this particular objective, the pressure in the tank is considered constant.

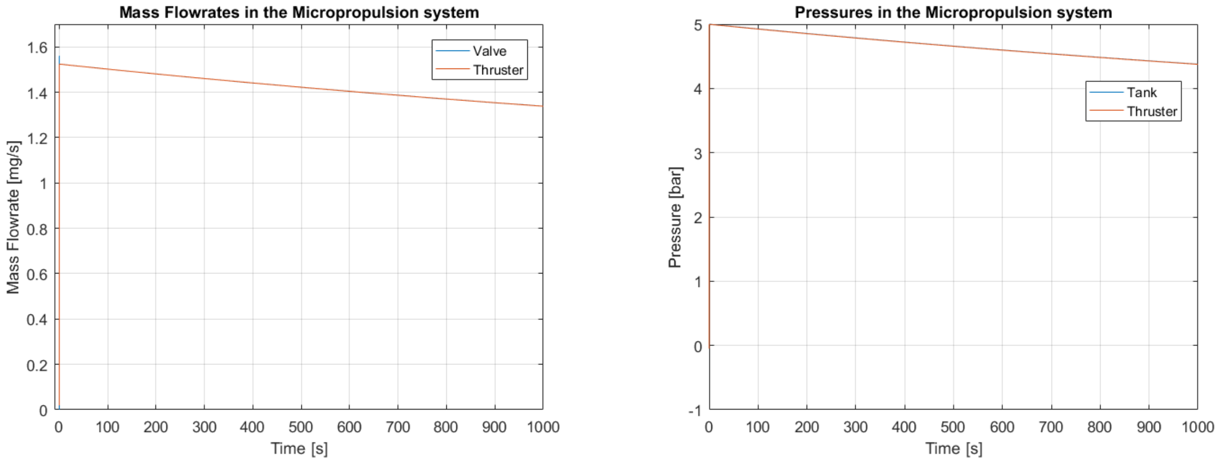

Figure 2.41: Results of the simulation for the blowdown micro-propulsion system. The variables shown are the the mass flow through the valve and the flowrate through the nozzle for the plot on the left. The tank pressure and the pressure in the thruster on the right.

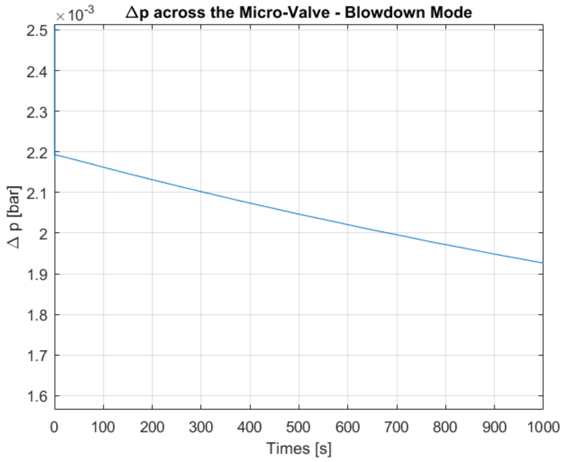

Figure 2.42: Pressure drop across the micro-valve. The initial pressure drop is ~ 5 bar but it quickly reaches the low value shown in the plot.

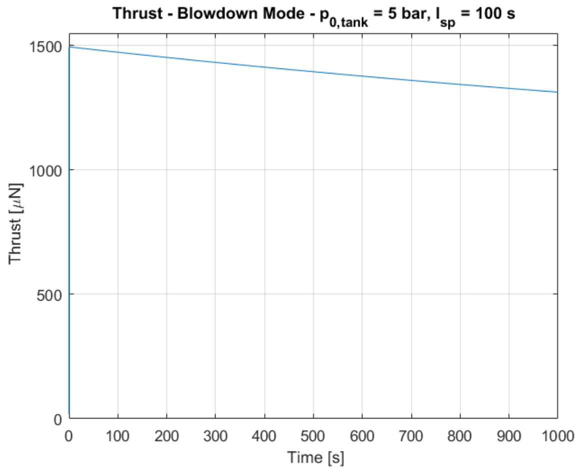

Figure 2.43: Thrust level for blowdown model. The thrust is calculated from the specific impulse, set to 100 s.

Blowdown Mode The simulation for the blowdown mode represents the most simple implementation of the micro-propulsion system. The tank is pressurized at a pressure $p_0 = 5\ bar$ and the valve is subsequently switched on. The simulation shows that the pressure builds up immediately in the micro-thruster, yielding a small pressure drop across the valve and consequently a very low mass flow rate, see Fig. 2.41 and 2.42. The thrust is calculated directly from the mass flowrate ejected through the nozzle, thus it resembles identically its transient, as seen in Fig. 2.43.

The mass flowrate through the system is low and the pressure in the tank decreases only slightly. Nevertheless, the rapid transient may be explained by the lack of representation of the vaporization process. Indeed, as mentioned earlier, the vaporization rate is kept equal to the outlet flowrate from the micro-valve. This is not realistic, due to the heating time required to increase water temperature and subsequently vaporize it. By neglecting the transient heating time, the response time is basically driven by the dynamics of the micro-valve and the pressure building process within the micro-thruster, for a given vaporization rate. Tab. 2.16 summarizes the main parameters used in the blowdown simulation. The parameters are chosen to simulate a realistic and representative case of the operation of the micro-propulsion system. The pressure in the tank is set to *5 bar* to meet the typical value used in the experimental tests. The value for the pressure is somehow justified by the literature, where a

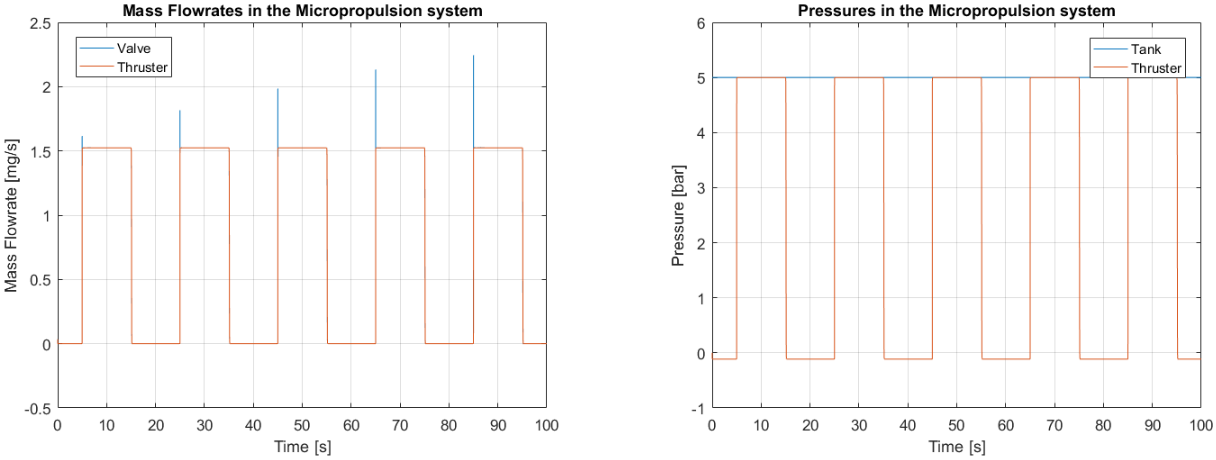

Figure 2.44: Results of the simulation for the regulated micro-propulsion system. The variables shown are the the mass flow through the valve and the flowrate through the nozzle for the plot on the left. The tank pressure and the pressure in the thruster on the right.

chamber pressure of *5 bar* is used in the chamber for simulations [11]. An analogous reasoning was made for the selection of the specific impulse, the aim of the VLM design is to achieve such value [63] [11], hence $I_{sp} = 100\ s$ was chosen for the simulation of the complete system and the calculation of the thrust magnitude. The specific impulse is dependent on the power of the heater and consequently the wall temperature of the chamber; nevertheless, the value chosen is close to those found for other temperatures [11] and hence representative for the purpose of this work. The volume of the tank is the first approximation of the value used in the experiments. Naturally, the results are highly influenced by the selection of the values for the parameters listed in Tab. 2.16. In particular, the pressure in the tank defines the maximum pressure achieved in the thruster and hence the generated thrust. The specific impulse can be regarded as a post-process parameters, since it basically turns the mass flowrate results into thrust values. The absolute values of the results would strongly be affected by a variation of these two parameters but the considerations on the control performances would not vary, e.g the response time.

Table 2.16: Parameters used in the blowdown simulation. The rest of parameters are set according to Tab. 2.5.

Parameter	**Value**
$p_{tank,0}\ [bar]$	5
$m_{H2O}\ [g]$	30
$V_{tank}\ [mL]$	40
$p_{th,0}\ [Pa]$	100
$I_{sp}\ [s]$	100
$t_{simulation}\ [s]$	1000

Thrust Pulse To perform a set of firing pulses, the pressure is assumed to be constant as in a regulated system. Although the pressure decreases slowly, as seen in Fig. 2.41, a regulated system is more appropriate to determine the maximum thrust that can be achieved repeatedly. The model of the thruster is still not extremely accurate, in addition the I_{sp} is based on a preliminary characterization of the device. Consequently, the thrust level may not be representative of the actual operating values. The simulation is run switching the valve on and off in a pulse pattern with a large period, $T_{switch} = 20s$.

The transient behavior at the actuation of the valve follows the micro-valve dynamics. Its response time is $\sim 10ms$. The overshoot in Fig. 2.44 is given by the mass of water accumulating in the micro-thruster. The pressure drop across the micro-valve in Fig. 2.45 decreases down to $\sim 2 \cdot 10^{-3}\ bar$ when the valve is switched off. The small pressure drop across the valve yield a very low mass flowrate even though the valve is completely open. The mass flowrate is $\sim 1.5\frac{mg}{s}$ during steady-state; the

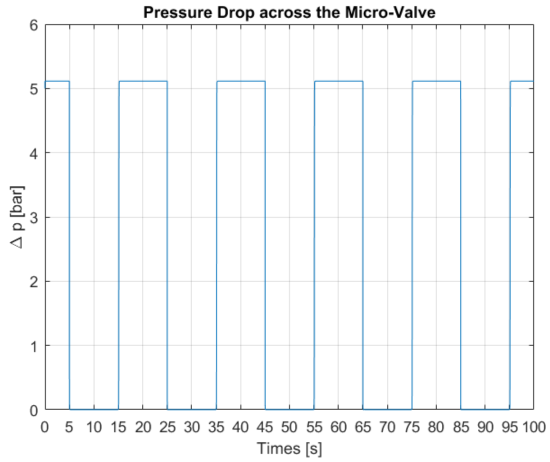

Figure 2.45: Pressure drop across the micro-valve. When the valve is closed it reaches 5 bar, whereas when the valve is switched on the pressure drop decreases to $\sim 2 \cdot 10^{-3}\ bar$.

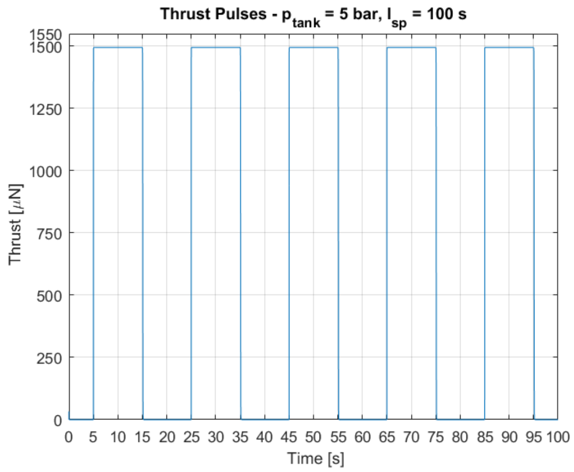

Figure 2.46: Thrust pulses for the micro-propulsion system. The thrust is calculated from the specific impulse, set to 100 s.

thrust is calculated from the I_{sp} and ranges from $0\ \mu N$ to $\sim 1.5\ mN$. It is important to note that these results are referred to the conditions set in the simulation. Above all, the pressure in the tank drives the maximum operating level of the thruster. However, the values used in the simulation are realistic for the operation of the micro-propulsion system anc represents the range of thrust values that can be achieved by the control system in this particular operting conditions. Tab. 2.17 summarizes the main parameters used in the simulation to determine the thrust range.

Table 2.17: Parameters used in the simulation to determine the thrust range.The rest of parameters are set according to Tab. 2.13.

Parameter	**Value**
$p_{tank,0}\ [bar]$	5
$m_{H2O}\ [g]$	30
$V_{tank}\ [mL]$	40
$p_{th,0}\ [Pa]$	100
$I_{sp}\ [s]$	100
$t_{simulation}\ [s]$	100
$T_{switch}\ [s]$	20
$DC_{pulse}\ [\%]$	50

2.6.2. Simulation Results - Controlled System

The task of regulating the thrust in the micro-propulsion system is performed by adjusting the mass flowrate flowing through the system. In the actual system, the pressure that builds up in the micro-thruster is dependent on the power of the heaters also. However, in the current model, the power is assumed to be sufficient to entirely vaporize the mass flowrate from the micro-valve at every instant in time. As already mentioned, the transient behaviour of the system is consequently driven by the valve dynamics and the pressure derivative in the thruster.

The PID controllers are implemented as derived in section 2.5.5. Since the mass flowrate is relatively low, as shown in the previous simulations, the gains are selected to perform a satisfactory control for a mass flowrate in the order of $\frac{mg}{s}$. The commanded input is the desired thrust, from which the real process variable, namely the mass flowrate, is calculated:

$$\dot{m} = \frac{F}{I_{sp} \cdot g} \tag{2.76}$$

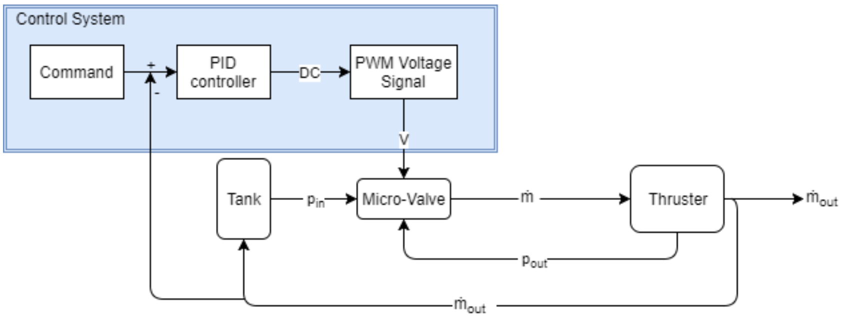

Figure 2.47: Block diagram of the closed-loop control system for thrust magnitude regulation. The figure shows the key blocks implemented in the Simulink model, which is not reported here for helping the visualization of solely the important blocks.

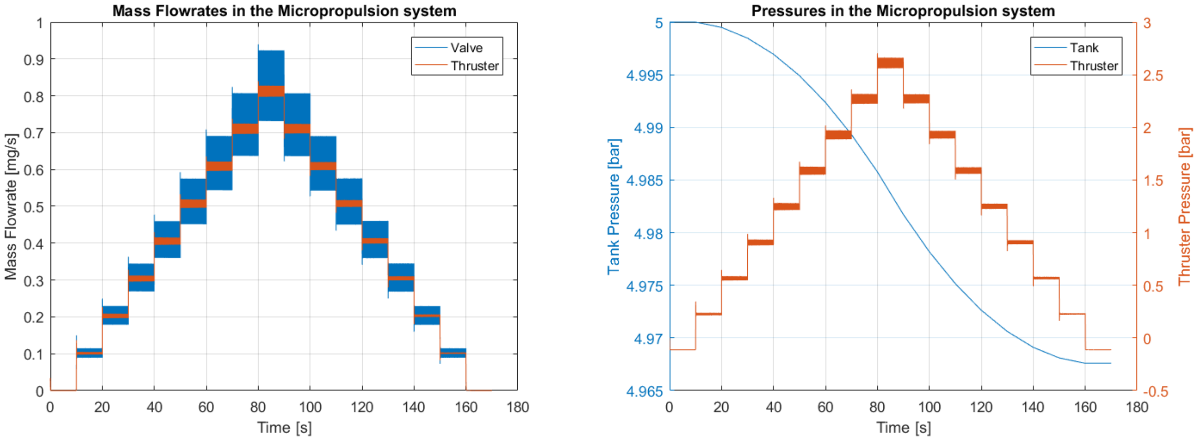

Figure 2.48: Results of the simulation for the blowdown micro-propulsion integrated with the closed-loop control system. The variables shown are the the mass flow through the valve and the flowrate through the nozzle for the plot on the left. The tank pressure and the pressure in the thruster on the right. Note that the axis scale for the pressure is different to enable the visualization of the trend in the tank pressure.

where F is the thrust, I_{sp} the specific impulse and g the gravitational acceleration. The block diagram is shown in Fig. 2.47. To test the model, a simulation is run with a stair-pattern thrust command in the range $[0 : 800]$ μN. The maximum value has been chosen in a way such that, as the pressure in the tank decreases, the controller will not saturate to reach the desired command. A step of 100 μN is used to approach the maximum value.

The closed-loop control perform satisfactorily by regulating the thrust accurately, see Fig. 2.50. The performance indices for the controller are reported in Tab. 2.18. The control variable, shown in Fig.

Table 2.18: Performance indices for the simulation of the closed-loop control system integrated in the comprehensive micro-propulsion system model.

ISE	**IAE**	**ITAE**
$7.52 \cdot 10^{-15}$	$7.90 \cdot 10^{-7}$	$6.29 \cdot 10^{-5}$

2.49 is rather stable for very low flowrates and starts oscillating as the commanded thrust increases. Though, this behaviour had already been studied in section 2.5. An important remark is that the commanded thrust is achieved while the upstream pressure is decreasing, although very slowly. The process variable is the mass flow through the thruster and not the one output by the valve, hence the valve outlet flowrate is less stabilized, as seen in Fig. 2.48. Tab. 2.19 summarizes the parameters used in the simulation of the thrust control system.
As explained in Chapter 3 the PID-PWM based control did not perform successfully in the complete system, due to hardware limitations. A modified version of the SMC control scheme, explained in section

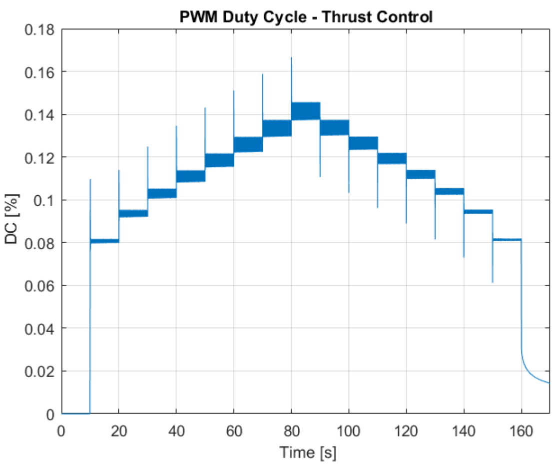

Figure 2.49: Values of the duty cycle of the PWM voltage input. The control variable is rather stable for very low flowrates and starts oscillating as the commanded thrust increases.

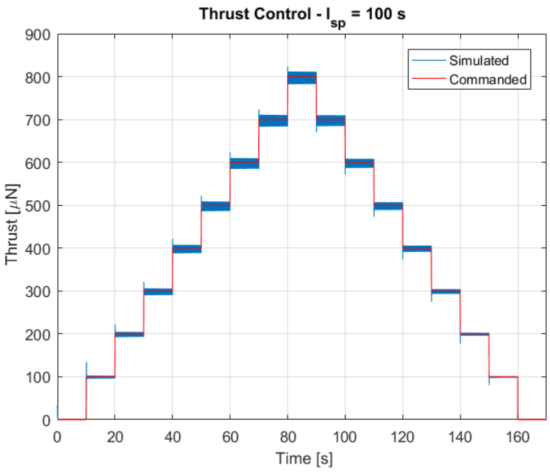

Figure 2.50: Comparison between the commanded thrust and the delivered one. As the control variable, the simulated delivered thrust is rather accurate and stable for low values.

Table 2.19: Parameters used in the simulation of the thrust control system. The rest of parameters are set according to Tab. 2.13.

Parameter	**Value**
$p_{tank,0}$ $[bar]$	5
m_{H2O} $[g]$	30
V_{tank} $[mL]$	40
$p_{th,0}$ $[Pa]$	100
I_{sp} $[s]$	100
$t_{simulation}$ $[s]$	100
f_{PWM} $[Hz]$	250
F_{max} $[\mu N]$	800
F_{step} $[\mu N]$	100
Gains	
k_p	$2.8 \cdot 10^5$
k_i	$2.1 \cdot 10^7$
k_d	114.6

2.5.7, has been implemented in the experiments. Given the hybrid nature of the control scheme, being derived by theoretical and empirical considerations, the Simulink model has been updated after the experiments. The results of the comparison between the results from simulations to the tests are described in Chapter 4.

2.7. Summary and Conclusions

This section summarizes the content of the chapter and draws several conclusions on the activity described. Since the chapter deals with several different aspects, the different considerations are made separately:

- The analytical model of the dynamics of the electro-magnetic actuated micro-valve has been developed based on the physical processes occurring when the valve is actuated. It is possible to split the model into three interfacing domains: electro-magnetic, fluid and mechanical. The valve is energized by a voltage signal, which yields an actuation current that in turns creates a magnetic flux within the inner coil. Consequently, the plunger is subject to a magnetic force that pulls it to finally open the valve. The usual strategy to simulate the flow within the micro-valve is to use the discharge coefficient, which is comprehensive of many processes actually occurring when the valve is actuated. This high-level parameter links directly the pressure drop across the valve to the mass flowrate flowing through it. A novel approach is represented by the insertion of a new state variable to accurately describe the transient behaviour of the fluid flow; the equation is derived using Navier-Stokes equation. On one hand, the additional equation resemble better the transient behaviour of the flow establishment; on the other hand, the derivation from Navier-Stokes equations implies the use of strong assumptions, such as the parallel plate flow, isothermal and incompressible flow. In addition, in the latter case, the mathematical description of the dynamics of the valve becomes more complex and hard to handle. However, the comparison between the numerical and analytical model justifies the use of the additional equation to describe the flow.

- The analytical model is validated and compared with a more sophisticated analysis using COMSOL Multiphysics simulation software. An approach to set-up the model is presented and described. The simulation comprises all the above-mentioned domains and is able to reproduce their interaction. The transient simulation is the most significant and allows a thorough comparison between the analytical predictions and the numerical ones. The models deliver compatible results in terms of steady-state mass flowrate, whereas they differ in the transient rise time to establish the flow. The discrepancy is within 30% that is equivalent to $\sim 3\ ms$.

- In order to assess the influence of each parameter, which is arbitrarily set in the model, a sensitivity analysis has been performed. The superiority of a global approach has been demonstrated. The idea of taking less sampling points but smartly distributed within the parameters space is effective: the one-at-a-time strategy, where each parameter is varied independently while the others are kept constant, required larger computational time and it was not possible to perform it in a reasonable time using 16 GB RAM - 3.16 GHz computational unit.

  The most influential parameter were found to be those linked to the electric characteristic of the system, namely the equivalent coil resistance and the number of coil turns. Nevertheless, several sub-groups of parameters, split into geometric, electric, magnetic and dynamics features, were analyzed to assess their contribution. Such results are useful to be able to tune the model to match different real devices; furthermore, if the model is used to predict design performances, the influence of each parameter may be taken as guideline for developing different design options.

- The ON/OFF valve is inherently not designed for controlling the flowrate. Nevertheless, for a continuous control the PWM actuation can be adopted, using the signal duty cycle as the control variable. The control law consist on the simple PID controllers. To tune the gains of PID the controllers several strategies have been presented: the approach that delivered the best results is based on the development of an averaged model, affine in the control, which can be linearized and hence analyzed with the tools typical of linear systems. The flowrate range is large, consequently the linearization point is truly important. A shortcoming of PID controllers is that they are meant for linear systems, hence they might not perform well far from the chosen operating point. To solve this problem, a gain scheduling approach could be adopted or, more simply, the range of desired flowrate be restricted.

In addition, a discontinuous control is also investigated using the SMC as a control scheme. Theoretically, the performances of such controller are superior and are not influenced by the model uncertainties. Nevertheless, hardware limitations, such as sensor sampling time and minimum achievable duty cycle, degrade the effectiveness of the controller. Based on considerations yielded by the experiments, a modified version of the SMC control scheme was developed and tested successfully, in simulations as well as in experiments.

- Finally, the micro-valve model developed in the first section 2.1 was integrated with the comprehensive model of the micro-propulsion system. The complete system comprises the analytical model of the propellant tank, filled with water and pressurized nitrogen, the micro-valve and a preliminary model for the VLM micro-thruster. Simulations showed the possibility to successfully control the thrust by implementing the control laws.

3

Experimental Characterization and Control

The following chapter describes all the experimental tests and set-up that have been employed in this thesis project. The description will follow a structure that is consistent with the one presented in Chapter 2. Section 3.1 presents the test whose objective was the characterization of the valve and the validation of the model. Section 3.2 presents the results of the response characterization of the valve to different PWM frequencies and duty cycles. Section 3.3 presents a method to measure the mass flowrate from the depressurization of the propellant tank without using a dedicated sensor. Section 3.4 and 3.5 describe the tests' results for the control system to regulate the output flowrate from the micro-valve. Section 3.6 describes the results of the tests performed with the complete micro-propulsion system, integrated with the closed-loop control system. Finally, section 3.7 summarizes the results and draws conclusions on the experimental part of this work.

3.1. Experimental Characterization of ON/OFF actuation

Up to this point, the modelling effort has focused on developing a model regardless of any particular valve design. The strong point so far is that it is rather straightforward to use the tool for predicting the performance level of different design configurations. Based on the experimental results, the model can be tuned to match as closely as possible the performances of the real device. In particular, to characterize the micro-valve, the discharge coefficient is assessed for different pressure drops and compared to the simulated results. In addition, a qualitative analysis is performed upon the transient response of the valve.

3.1.1. ON/OFF Actuation: Experimental Setup

In order to measure the flowrate for different pressure drops across the valve, the set-up schematized in Fig. 3.1 was built. The valve is controlled using a spike-hold circuit delivered by the electronics board, which is controlled by the NI USB-8451 board connected to the PC. The detailed description of the circuit is reported in Fig. 3.2. Moreover, the pressure and temperature sensors communicate via I^2C with the computer through the NI USB-8451 board. The scale is directly connected to the PC and sends data directly to it. All the output data from the sensor, actuation and start/stop experiment commands are handled in the PC using LabView.

- The VHS Lee Valve (INKX0511400A) is a high speed, 2-way normally closed solenoid operated valves. The device used in the tests is shown in Fig. 3.2. The valve can only be fully actuated, without any built-in proportional behaviour. The valve has already flown as part of a cold-gas propulsion system for the Delfi-Next mission by TU Delft. The valve is actuated using a spike and hold circuit, designed by the manufacturer, shown in Fig. 3.2.

- The NI USB-8451 is a master interface for connecting to and communicating with inter-integrated circuit (I^2C), System Management Bus ($SMBus$), and serial peripheral interface (SPI) devices. It

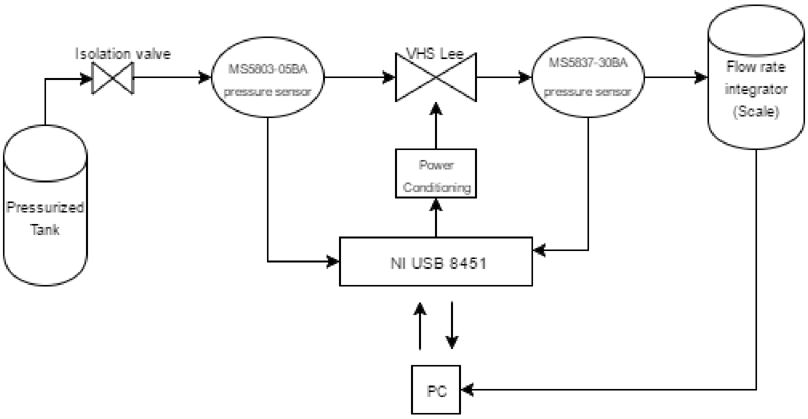

Figure 3.1: Block diagram of the experimental set-up used for the valve characterization.

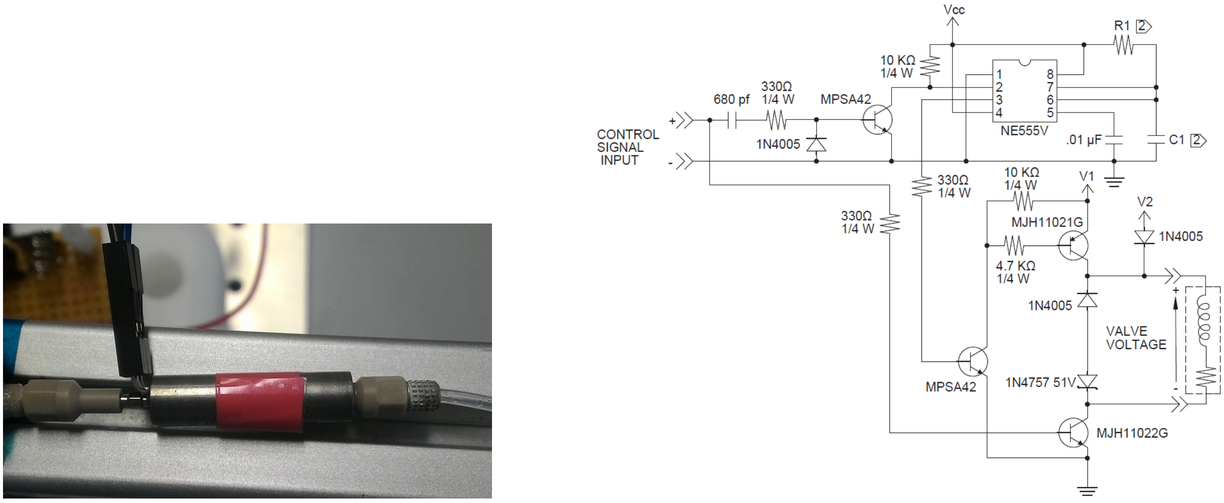

Figure 3.2: VHS Lee Valve used for testing and the actuation spike and hold circuit, on the right.

enables the communication with COTS electronics and integrated circuits. It also includes eight general-purpose digital I/O lines that can be used for several applications. The sampling time is $0.1\ s$ on average based on the reading frequency of the sensor.

- The pressure and temperature sensors are both from *TE connectivity*. The MS5803-05BA is a 5-bar altimeter sensor with SPI and I^2C bus interface. The maximum achievable resolution for pressure and temperature measurements is $0.036\ mbar$ and $0.01\ ^oC$, respectively. It provides a precise digital 24 Bit pressure and temperature value yielding an accuracy of $\pm 100\ mbar$ for the full pressure range and $\pm 2.5\ ^oC$ for the temperature. The sensors presents a very low hysteresis and an acceptable stability of both pressure and temperature signal for the required application. The MS5803-30BA is a 30-bar pressure sensor with only I^2C bus interface, specifically designed for water depth measurement systems. The maximum achievable resolution for pressure and temperature measurements is $0.20\ mbar$ and $0.0022\ ^oC$, respectively. The best full-range accuracy is $\pm 200\ mbar$ for pressure and $\pm 1.5\ ^oC$ for temperature. In addition to the common features of the 5-bar sensor, the MS5803-30BA is waterproof, which makes it suitable for measuring water pressure in the feeding lines.

- The scale is the HCB 123 - Highland Series from *Adam Equipment*. The maximum capacity is $120\ g$ and the resolution is $1\ mg$. It is equipped with a USB communication interface, which can be easily fed into the Labview code. The sampling time is $0.6\ s$ between two consecutive readings. The sampling time is relatively large for control purposes: the control input is updated every time a measurement is sensed, however, the dynamics of the micro-valve is rather fast and

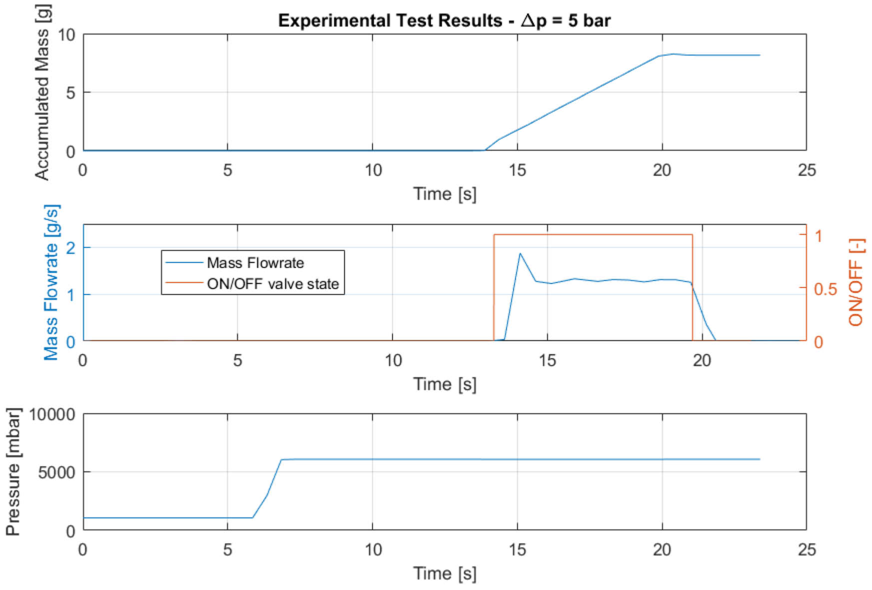

Figure 3.3: Experimental test results concerning accumulated mass, mass flowrate and pressure at valve inlet. The test case is with pressure drop $\Delta p = 5\ bar$.

consequently the hold time may prevent an effective control action. This is very true when it comes to the implementation of the SMC controller, where the discontinuous control input is kept to either completely ON or OFF for the entire hold period.

3.1.2. ON/OFF Actuation: Experimental Procedure

The feeding pipe to the valve is filled with water. The pressurized N_2 is injected to pressurize the line. Depending on the type of operations to test, whether constant pressure or blow-down, the pressurized tank is kept connected or not. The valve is then actuated and the output from the sensors and the scale are registered for post-processing. The mass flowrate is calculated using a simple numerical derivative between two subsequent time instant:

$$\dot{m}_{k-1,k} = \frac{M_k - M_{k-1}}{t_k - t_{k-1}} \tag{3.1}$$

where M is the accumulated mass and t is the time instant. For instance, the results from the test with $\Delta p = 5\ bar$ is shown in Fig. 3.3. To determine the discharge coefficient as a function of the inlet pressure, the orifice equation is used. The form of the discharge coefficient that is obtained by experimental tests is slightly different from the one described in section 2.1. The reason why this happens is that it is impossible to measure the outlet area of the actual device, thus the experimental discharge coefficient includes the product between the theoretical one and the outlet area in such fashion:

$$C_{d,exp} = C_d \cdot A_{out} = \frac{\dot{m}}{\sqrt{2\rho\Delta p}} \tag{3.2}$$

The mass flowrate used in Eq. 3.2 is the steady-state value.

3.1.3. ON/OFF Actuation: Results and Discussion

The scale measurements are rather stable and the noise level is really low, which yields smooth experimental results. The scale of the pressure measurement plot does not allow to visualize the noise in the signal, which will become relevant in section 3.3 where it will be post-processed to obtain mass flow measurements. The experimental discharge coefficient for different pressure drops is compared to the values used in the analytical simulation. The latter is based on the numerical simulation, as discussed in section 2.3 and on the differential equations developed in section 2.1. The comparison is shown in

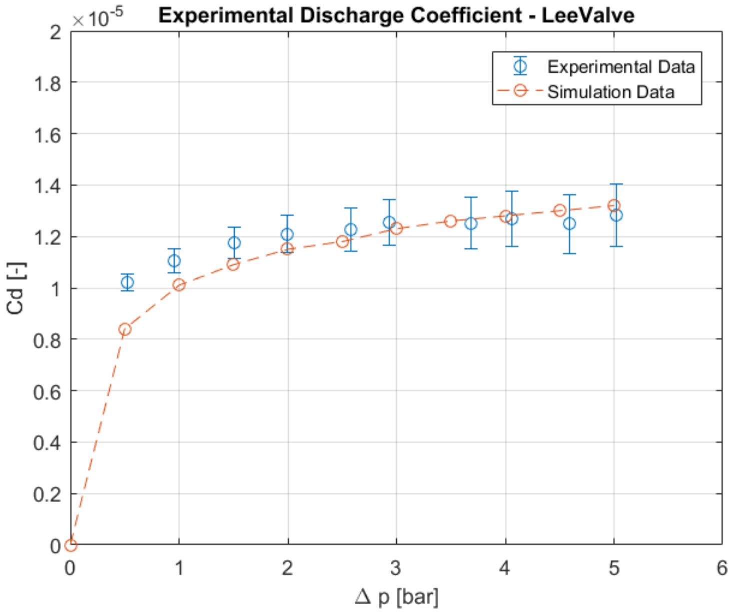

Figure 3.4: Comparison of the experimental discharge coefficient from tests and simulations using VHS Lee Valve.

Fig. 2.1 3.4. The results are satisfactory for several reasons. First of all, the maximum difference is found for a Δp of 0.5 bar and is less than 15%, which is acceptable for the analytical model. Secondly, it is remarkable that just by using numerical simulations referencing only to the dimensions of the real device, it is possible to predict with such a small error the operations of the real device. This, again, will be useful when design iterations will start, before manufacturing any valve. In principle the model could be tuned by introducing a slight variation in few critical parameters that influence the steady-state behaviour of the valve, such as the spring elastic constant. However, the less the model is tuned according to experimental results, the more powerful its use will be when employed for the design process.

The error on the determination of the discharge coefficient can be calculated according to error propagation theory [64]:

$$\delta C_d = C_d \sqrt{\left(\frac{\delta(\Delta p)^{-\frac{1}{2}}}{(\Delta p)^{-\frac{1}{2}}}\right)^2 + \left(\frac{\delta \dot{m}}{\dot{m}}\right)^2} \tag{3.3}$$

where:

$$\frac{\delta(\Delta p)^{-\frac{1}{2}}}{(\Delta p)^{-\frac{1}{2}}} = \frac{1}{2}\frac{\delta \Delta p}{\Delta p} \text{ and } \delta \Delta p = \delta p \sqrt{2} \tag{3.4}$$

3.2. Experimental Characterization of PWM actuation

An important feature of the valve is to be actuated by fast-switching PWM voltage signal. As already mentioned, this is critical and fundamental to let the valve to be controlled. Therefore, the behaviour of the valve for different PWM frequencies and duty cycles has to be investigated.

3.2.1. PWM Actuation: Experimental Setup

The experimental set-up is nearly the same as the the one described in section 3.1.1 with the addition of a *RedBear* Blend Micro board, shown in Fig. 3.5 to deliver a stable PWM input voltage to the spike-and-hold circuit. Fig. 3.6 shows the components of the experimental setup for the characterization of the valve when actuated by PWM voltage signal.

The Blend Micro is an single integrated development board, consisting of an Arduino with a Bluetooth Low Energy chip. The micro-controller unit (MCU) is Atmel ATmega32U4. The clock speed is $8\ MHz$ and the operating voltage is $3.3\ V$. The board can be programmed using the Arduino interface: the internal frequencies of the analog output pins are $250Hz$ and $500\ Hz$. To adjust the duty cycle of the PWM, the *analogWrite* command is used, which delivers a PWM at the prescribed frequency and the specified duty cycle ranging from 0 to 255.

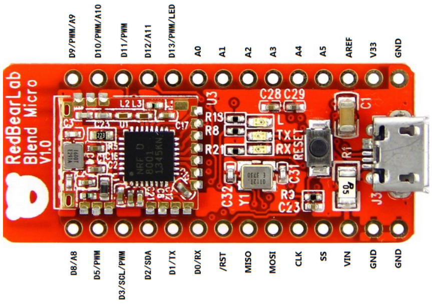

Figure 3.5: Blend Micro board from *RedBear* used to generate the PWM voltage signal.

3.2.2. PWM Actuation: Experimental Procedure

The major difference with section 3.1.2 is that the control voltage for actuation is operated in PWM mode. In principle, the PWM can be implemented in the Labview code: the control digital pin of the NI-USB 8451 could be switched ON/OFF by sending commands from the computer. Nonetheless, the timing of the operations relies on the computer clock: depending on the internal CPU activity the operations are executed subsequently. For this reason the ON/OFF cycle to perform the PWM is not stable and constant in time, the duty cycle varies significantly even if it is not changed by the user. This behaviour is not acceptable, especially in terms of characterization of the valve, where the absolute

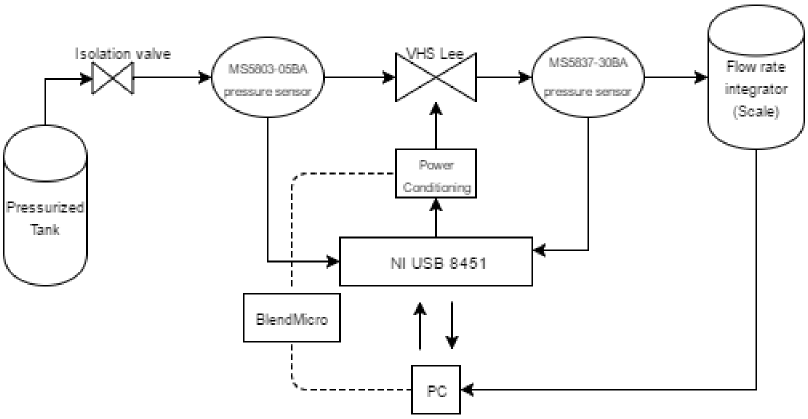

Figure 3.6: Block diagram of the experimental set-up used for the valve characterization when actuated by PWM voltage signal.

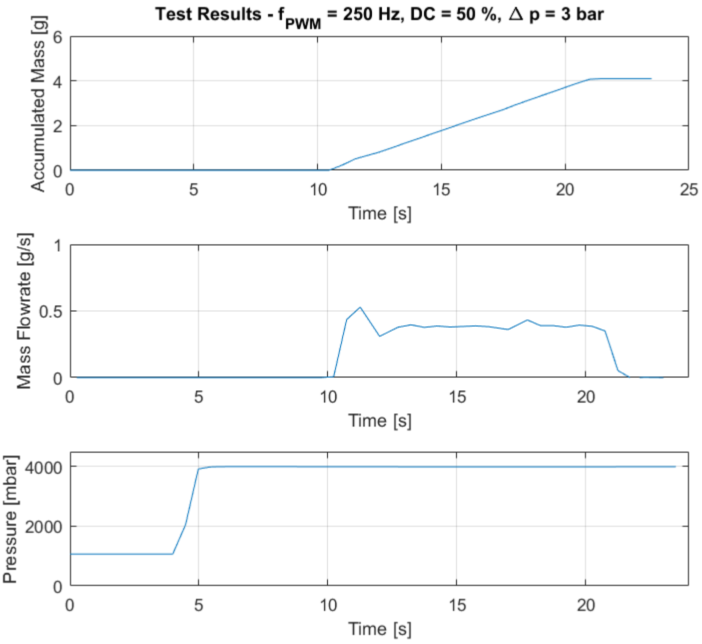

Figure 3.7: Set of results for the accumulated mass, the flowrate and the inlet pressure for the valve actuate using PWM frequency of $f_{PWM} = 250\ Hz$. The test is performed using a duty cycle of $DC = 50\%$.

value of the duty cycle for a given frequency is registered. The RedBear Blend Micro has several digital pins that can be operated as PWM output. The routine to generate the switching signal is implemented by the manufacturer and it is found to be stable and robust by measuring it with an oscilloscope. One simple digital pin can also be used for generating PWM by commanding ON/OFF digital state and delays, in the same fashion as the LabView software-based implementation. Unlike the CPU accuracy, the micro-controller delivers a fairly stable behaviour using the latter approach also.

The feeding pipe to the valve is filled with water. The pressurized N_2 is injected to pressurize the line. Depending on the type of operations to test, whether constant pressure or blow-down, the pressurized tank is kept connected or not. The valve is then actuated and the output from the sensors and the scale are registered for post-processing. The flowrate is determined using Eq. 3.1. A typical set of test results is shown in Fig. 3.7.

The accumulated mass is measured directly by the scale. The constant pressure is provided by the pressurized Nitrogen tank. To proceed with the analysis, the steady-state flowrate for each duty cycle and PWM frequency is determined. To do so, the average is calculated: the steady-state time is set after the initial peak in the flowrate and the last value taken for the average is the time instant before the valve is switched off completely.

3.2.3. PWM Actuation: Results and Discussion

The extensive test results can be summarized in Fig.3.8 and 3.9.

The plots show the flowrate for different duty cycles and different pressure drops across the valve. Two frequencies were investigated as in the simulation approach, namely 250 and 500 Hz. The dependency of the flowrate on the duty cycle for the lower frequency is almost linear except for the flattened part at very low duty cycles. Such behaviour was expected from the simulations results, where a second-order behavior was rather clear. Beside this, there are some unexpected values that might be disregarded in the analysis. For instance, the flowrate for 60 % duty cycle and 1 bar of Δp is slightly off from the expected value. This may be due to errors in the particular test procedure that need further investigation.

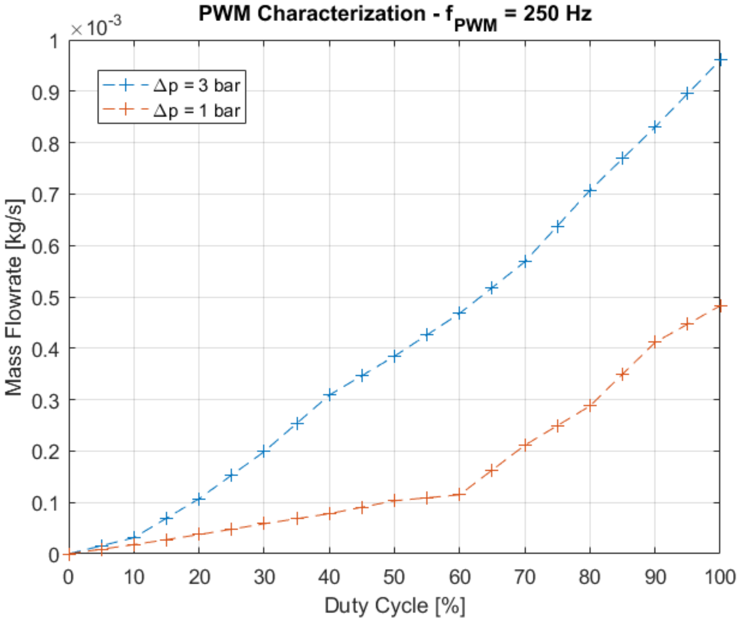

Figure 3.8: Mass flowrate as a function of the duty cycle of the PWM at the frequency $f_{PWM} = 250\ Hz$.

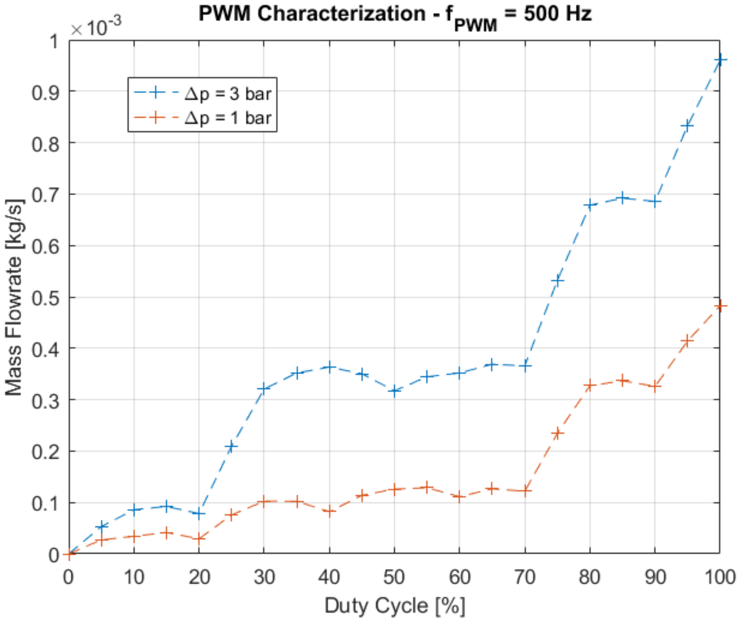

Figure 3.9: Mass flowrate as a function of the duty cycle of the PWM at the frequency $f_{PWM} = 500\ Hz$.

Regarding the case of higher frequency of 500 Hz, the results are less satisfactory. The issue associated with such frequency is inherent of the device; indeed, the datasheet reports a maximum switching frequency of 1000 Hz. When operated with 500 Hz, the valve did not respond correctly for duty cycles lower 40 %. The high frequency prevent the micro-valve from actuating correctly, making the switch unreliable. Furthermore, it could happen that stressing the valve in this way yields a damage for long-run operations. Although this might be the fundamental reason, errors in the test procedure shall not be excluded.

On the whole, it is safe to discard 500 Hz as the operating frequency. There are no significant advantages in using such frequency and, obviously, the test results are rather meaningful on its applicability. Hence, only lower frequencies are taken into account for the implementation.

3.3. Mass Flow Measurements

To characterize the valve, the mass flowrate represented solely a post-processed measurement. The analysis concerned the steady-state value of the output flowrate, without any needs to process the measurements during the experiment. Nevertheless, to perform the regulation of the flowrate within a closed-loop system it is critical to sense the flowrate and feed its value in the loop during the experiment. The scale may, in principle, be used to perform such action; however, it is removed from the loop and substituted by a mass flow measurement derived by the depressurization of the tank. The scale output data rate is slow, reaching an average time between two consecutive readings of 0.6 s; such a low updating frequency degrades the performance of the controllers yielding instability of the control variable. Furthermore, the objective of the thesis is to develop the closed-loop control system for nano-satellites application, hence the scale is too bulky to be thought as a potential device to implement in a real micro-propulsion system ready to fly. Naturally, the working principle of the scale is not really suitable for micro-gravity environment.

The mass flowrate can be determined by the difference between two consecutive pressure reading of the pressurized nitrogen. The idea is to exploit the ideal gas law and assess the change in volume, related to the mass of water that is displaced, to the value of pressure. Given a pressurized tank filled by $m_{0,N2}$ kilograms of Nitrogen, at a constant temperature T the derivative of the volume is expressed:

$$\dot{V} = \frac{\partial V}{\partial p}\frac{dp}{dt} = -\frac{m_{0,N2}RT}{p^2}\dot{p} \tag{3.5}$$

where V is the volume of Nitrogen, p is the pressure, R the specific universal gas constant. For the implementation in the Labview code, the differential expression in Eq. 3.5 must be integrated:

$$\Delta V = -m_{0,N2}RT\int_{t_0}^{t_1}\frac{\dot{p}}{p^2}dt = m_{0,N2}RT\left(\frac{1}{p_{t_1}} - \frac{1}{p_{t_0}}\right) \tag{3.6}$$

where t_1 and t_0 are two consecutive time instants where the pressure readings are available. The process is considered isothermal, hence the temperature constant.

Given that water is in-compressible, the change in Nitrogen volume is related to a displaced volume of water. Hence, the water mass flowrate can be determined as:

$$\dot{m} = \rho_{H_2O}\frac{\Delta V}{\Delta t} \tag{3.7}$$

where $\Delta t = t_1 - t_0$ and ρ_{H_2O} is the density of water.

To validate the proposed procedure, a test has been run comparing the flowrate measurement derived from post-processed scale measurements and real-time mass flow measurements coming from pressure readings. Fig. 3.10 shows the comparison. It is important to note that this method works only in a blow-down mode, where the pressure actually decreases and allows all the analytic calculation described above. The major drawback of the approach presented hereby is taking the derivative of a sensed signal. Pressure measurements carry an inherent noise that is amplified when inserted in Eq. 3.6. Fig. 3.10 shows how the mean value of the flowrate measurement derived from pressure is coherent with the one calculated from the scale. The accuracy of the method is thus reliable and promising for further investigations. However, the signal is not precise and its variance is significant. To overcome this issue, a point-by-point filter can be implemented to smooth the curve and yield a more accurate and precise mass flow output signal. Since the frequency of the noise is much higher than any measurement spectral content, a low-pass filter is chosen.
The Butterworth low-pass filter is represented by its frequency magnitude response with a normalized gain [65]:

$$G(\omega) = \frac{1}{\sqrt{1+\left(\frac{\omega}{\omega_c}\right)^n}} \tag{3.8}$$

where ω is the angular frequency, ω_c is the cut-off frequency and n is the order of the filter. In the practical implementation, several parameters need to be set:

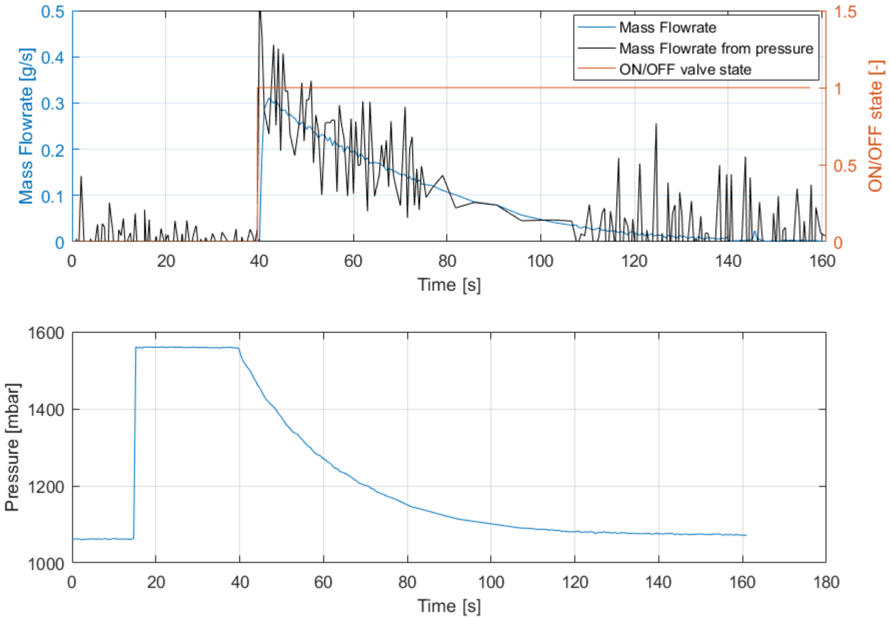

Figure 3.10: Comparison between the mass flowrate values derived from post-processed scale readings and those calculated from tank depressurization.

Sampling Frequency [Hz]	**Order [-]**	σ^2 $[(\frac{kg}{s})^2]$	**Unfiltered** σ^2 $[(\frac{kg}{s})^2]$	**Delay [s]**
5	5	1.08E-11	0.0093	1.89
5	2	1.78E-10	0.0246	1.01
10	2	5.92E-13	0.0098	2.14
10	5	4.44E-10	0.0262	2.79
1	2	1.26E-09	0.0202	0.18

Table 3.1: Performance of different filters applied to pressure signal for mass flow measurements.

- **Sampling frequency** is the frequency f_s in Hz at which the signal to filter is sampled.
- **Low cut-off frequency** is the frequency at which the gain falls 3 dB from the maximum value. The standard value is set to $0.125\ Hz$. The cut-off f_c frequency must respect the Nyquist criterion $0 < f_c < 0.5 f_s$.
- **n** is the order of the filter and defines the slope of the cut-off transition.

The sampling frequency and, to a smaller extent, the order of the filter affect the filtered signal in terms of delay and resultant variance of the system. To investigate the behavior of different filters, the options proposed in Tab. 3.1 were tested. For each alternative, the delay introduced in the system was assessed by measuring the time difference of the signal response at the instant in which the valve was turned ON. In order to estimate the noise level, the variance is taken as reference. It is calculated when the valve is turned OFF at the beginning of the experiment, where the value of the flowrate is actually null. The control has to react fast to any disturbance or change in set-point. Hence, the delay needs to be constrained. By increasing the sampling frequency, the delay increases but the variance is reduced. The same effects occur when increasing the order of the filter. An acceptable trade-off between residual variance and system delay is found for the 2^{nd} order filter using 1 (standard) or 5 Hz sampling frequency. The plots of the tests are shown in Fig. 3.11.

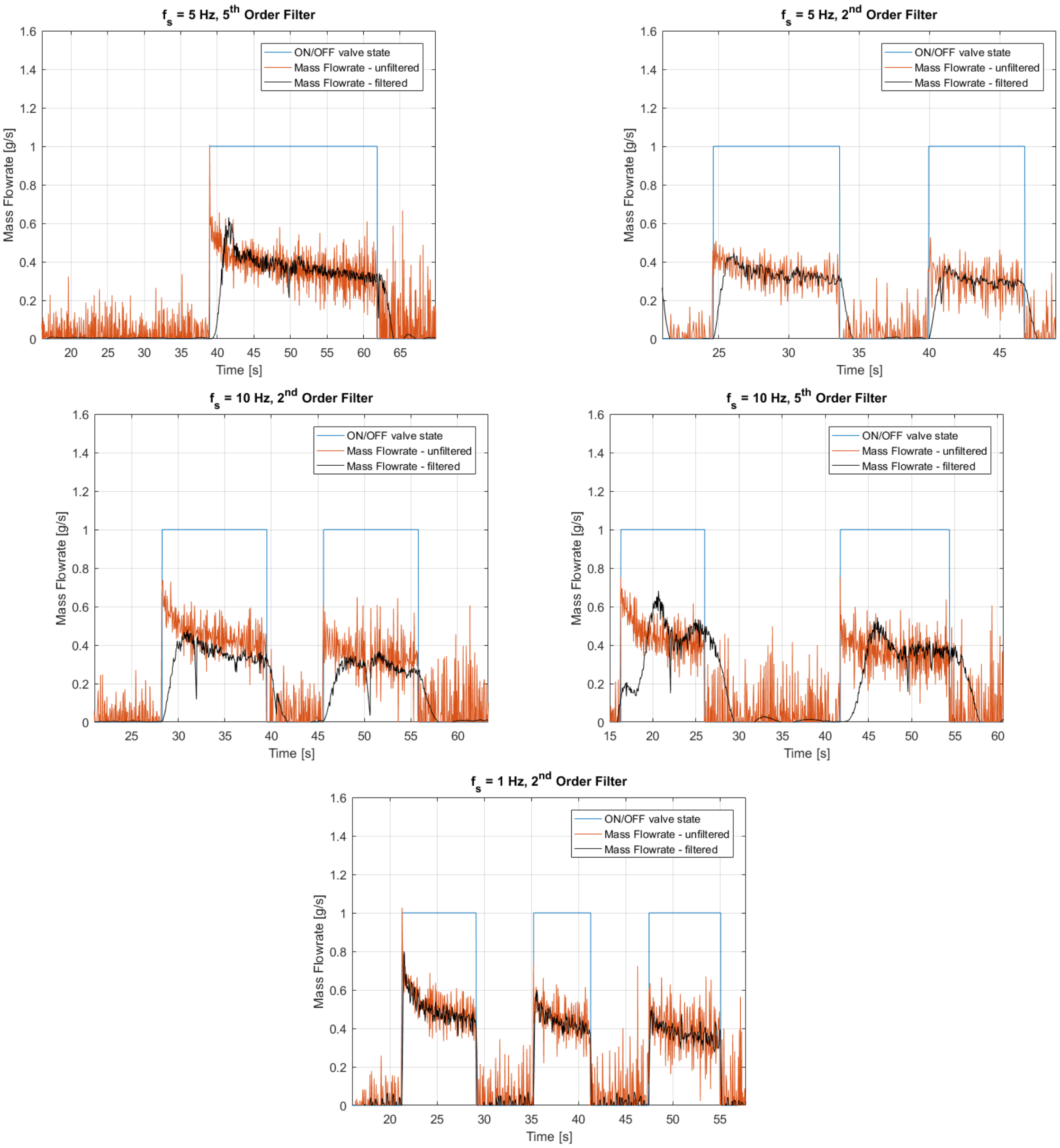

Figure 3.11: Performance of different filters applied to the pressure signal for mass flow measurements. The top left is the first test

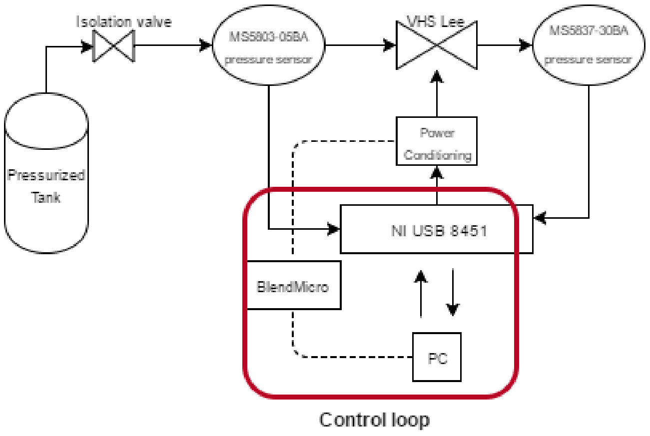

Figure 3.12: Block diagram of the experimental set-up used for the closed-loop control for regulating the flowrate.

Table 3.2: PI gains tuned using the averaged model for experiments.

Tuning	k_p	k_i
$10^{-4}\frac{kg}{s}$	$3.0 \cdot 10^2$	$5.9 \cdot 10^4$

3.4. Valve Control PID

To regulate the outlet flowrate from the valve, the closed-loop control system designed in Chapter 2 is implemented with PID control to adjust the duty cycle.

3.4.1. Valve Control: Experimental Setup

The experimental setup to test the capability of controlling the flowrate is different from the one presented in section 3.1.2. In particular, the scale is removed. Since no miniaturized mass flowrate sensor was available at the time this thesis has been developed, the flowrate was measured by processing the pressure data at the tank. The procedure has been explained in the previous section 3.5. The PID controllers are implemented in the Labview code. Fig. 3.12 shows a schematic of the main components.

3.4.2. Valve Control: Experimental Procedure

The Nitrogen tank is fed by the pressurized tank. The amount of gas is determined by weighting the tank before and after it has been filled by the gas. The amount of pressurized N_2 is required to determine the mass flowrate. The tank is then connected to the feeding line, which is filled with water. The commanded flowrate is set and can be changed during the experiment, or be programmed to change at the beginning of the test. Pressure at the tank, outlet pressure, temperature and operating duty cycle data are logged.

3.4.3. Valve Control: Results and Discussion

The tests were first run using the controller gains determined in section 2.5. As explained in section 3.5, the mass flowrate signal is rather noisy without any filters and the accuracy to measure values $10^{-4}\frac{kg}{s}$ is not reached, as shown in Fig. 3.13. The actual measurement would be shaded by the random oscillations of the process variable. For this reason, in the actual implementation, it was only possible to control the flowrate within a higher range of flowrate, up to $0.6\frac{g}{s}$. An additional issue with the process is that, given the variance of the signal, the derivative contribution made the controller unstable. Even though the derivative gain in Tab. 2.12 is very low, it was preferred to re-design the PI control using the same methodology. If the averaged model is taken as reference, the PI gains are found to be those listed in Tab. 3.2. The controllers perform satisfactorily in controlling the output flowrate, see Fig. 3.13 and 3.14. Nevertheless, the settling time is significantly higher $\sim 1\ s$ than the designed one. This may be due to the properties of the process variable signal, which was considered without noise in the simulations and the insertion of the Butterworth filter in the experimental setup.

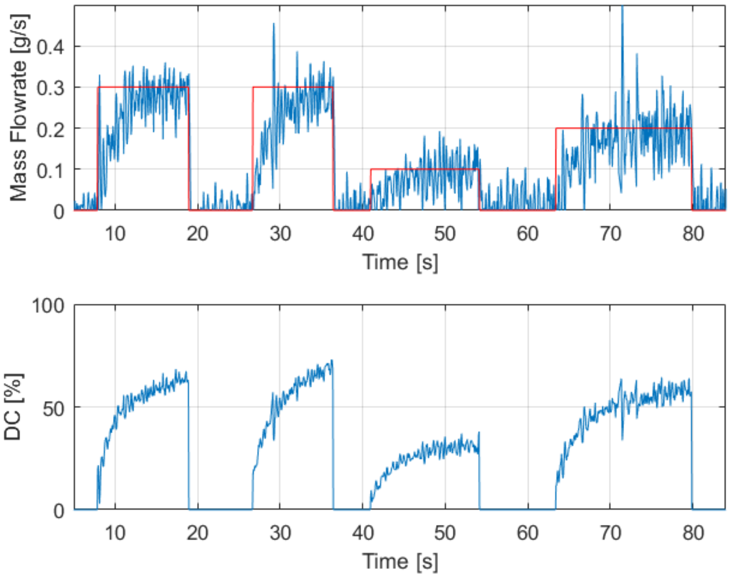

Figure 3.13: Mass flowrate pulse command with 2^{nd} order Butterworth (1 Hz sampling frequency) filter applied to the pressure readings. The variance of the signal is high, hence it is impossible to control the output below $10^{-4}\ \frac{kg}{s}$.

Furthermore the noise level of the signal is so high that if a stair-pattern command is given, in the same fashion as Fig. 3.14, the different output are hardly recognizable. This behaviour degrades significantly the signal resolution, which is defined as the minimum change in the command that can be sensed. The 2^nd order Butterworth filter with 5 Hz sampling frequency has been implement to improve the poor resolution. As explained in section 3.5, increasing the sampling frequency yields a longer delay in the system response. The trade-off between resolution and response time should be done when the complete system is tested and operative modes are better defined.

By introducing the 2^{nd} order Butterworth filter with a 5 Hz sampling frequency the flowrate output signal improves significantly in terms of variance but, on the other hand, a time delay is inserted in the system. For the above filter, the settling time increases up to nearly 3 s as can be seen in Fig. 3.15. To improve the response time, the gains can be adapted to the real application. This a standard way of proceeding, where the simulations provide a baseline for the controllers gain that are then adjusted to meet the requirements and improve the performances in a real application. The proportional part of the controller is responsible for making the system response faster [53]. However, a large proportional gain may lead to instability of the system. Fig. 3.16 shows the response of the microvalve to a stair-pattern commanded input for the proportional gain set to $k_p = 800$. The improved performances in terms of signal quality yields a better resolution of the output signal, as shown in Fig. 3.16. Indeed, steps in the commanded input down to $5 \cdot 10^{-5}$ are resolved. At some instants, large spikes occur in the mass flowrate measurements. A reason for this is the presence of air bubbles in the feeding lines, that are created when the pressurized tank is connected to the tube. Furthermore, the initial pressure of the tank has been set to 4.5 bar in order to demonstrate that the controllers are valid for the wide pressure range. Consequently, the duty cycle is relatively low compared to Fig. 3.14.

As already mentioned, the resolution of the controller is constrained by the measurement signal rather than the hardware limitations. The variance of the mass flowrate signal is listed in Tab. 3.1, which yields a standard deviation of $\sigma \sim 1 \cdot 10^{-5} \frac{kg}{s}$. Hence, theoretically, the minimum difference in the flowrate that can be detected should be σ: Fig. 3.17 shows that the maximum resolution of $1 \cdot 10^{-5} \frac{kg}{s}$ can be achieved using the described set-up. Nevertheless, the performance is rather poor and needs to be improved by using more accurate mass flow measurements.

A common issue with PI controllers is the saturation of the control actuator. An integrator windup is

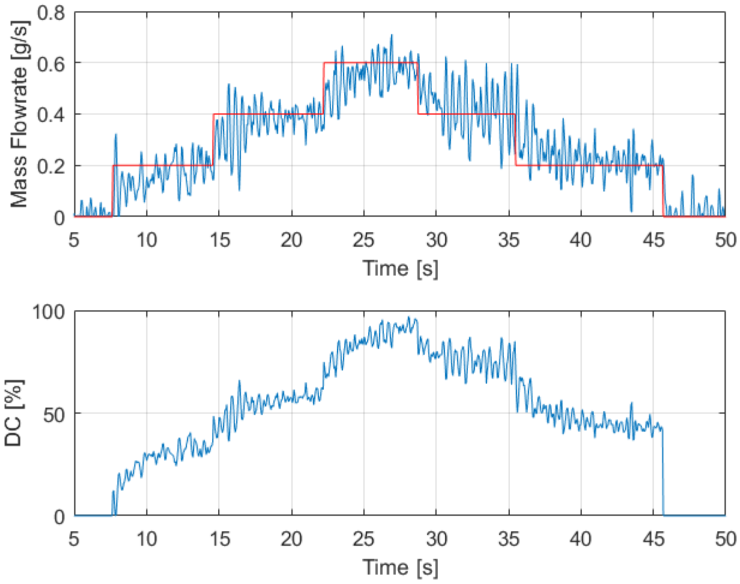

Figure 3.14: Mass flowrate pulse command with 2^{nd} order Butterworth (1 Hz sampling frequency) filter applied to the pressure readings. The variance of the signal is high. The mass flowrate resolution is degraded.

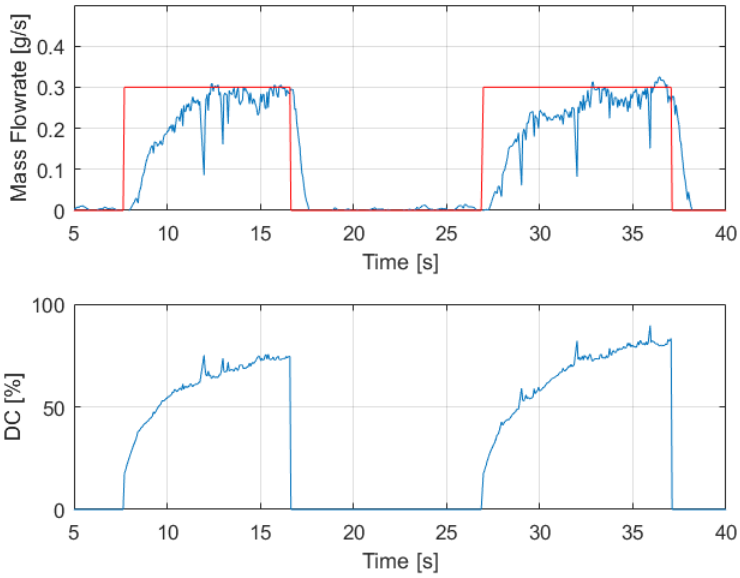

Figure 3.15: Mass flowrate pulse command with 2^{nd} order Butterworth (5 Hz sampling frequency) filter applied to the pressure readings. The variance of the signal is reduced, a delay is inserted according to the analysis made in section 3.5.

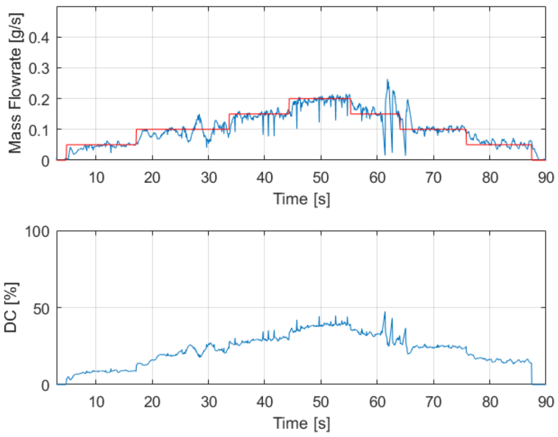

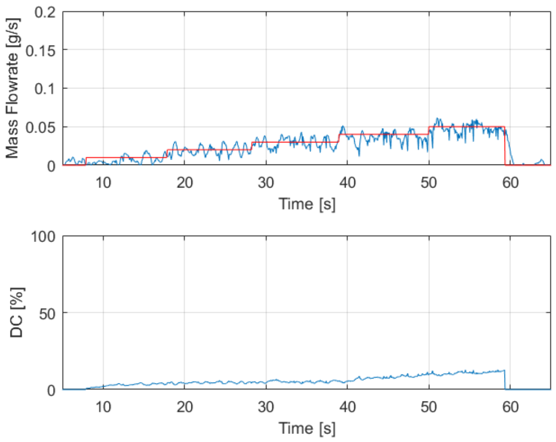

Figure 3.16: Mass flowrate pulse command with 2^{nd} order Butterworth (5 Hz sampling frequency) filter applied to the pressure readings. The variance of the signal is reduced. The mass flowrate resolution improves.

Figure 3.17: Test with $1 \cdot 10^{-5} \frac{kg}{s}$ step commanded input. Theoretically, the best resolution of the system is determined by the mass flowrate measurement standard deviation.

the process where the integral controller contribution keeps increasing even if the saturation limit has been reached. In principle, the integral error shall vanish when the system has spent some time in steady-state. If the integral error is not zero when the set-point is changed or a violent disturbance occurs to the system, the control-loop may react slower than required since it is biased by the present integral error. By implementing a signal limiter for the control variable, which is correlated with the hardware limitation, the integrator is prevented from winding up. An additional error e_s is introduced to represent the difference between the controller output and the actuator output. Such error is fed back into the integrator through a prescribed gain. If the actuator is not saturated, the error e_s has no effects on the closed-loop, whereas if the actuator is saturated the additional feedback loop drives the error e_s to zero. This forces that the controller output is kept close to the saturation limit. Such Anti-Windup Scheme is implemented in Labview and its schematics is shown in Fig. 3.18.

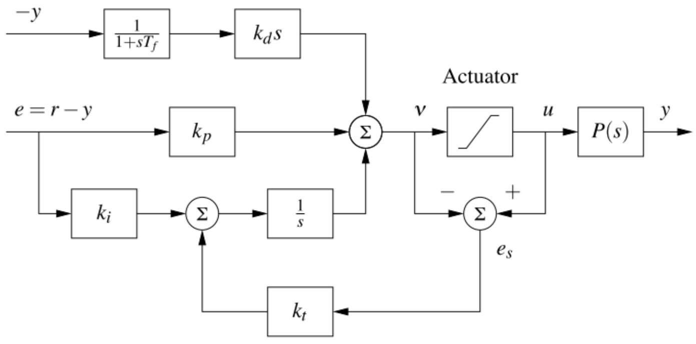

Figure 3.18: Anti-Windup Scheme implemented in Labview [8].

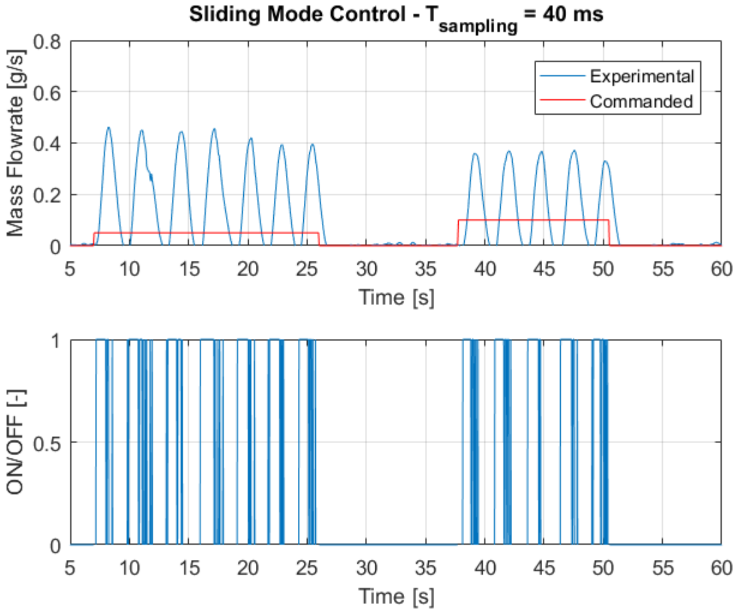

Figure 3.19: Experimental results for the sliding mode control designed according to section 2.5.7.

3.5. Valve Control SMC

Sliding mode control is a very accurate and robust control approach that is not sensitive to model uncertainties. Furthermore, it exploits the possibility to operate actuators in a fast switching mode, typical for PWM-driven devices. Nevertheless, the simple control developed in section 2.5.7, is not appropriate for a discrete control, characterized by a finite sampling time.

The experimental setup is identical to that described in the previous section 3.4, as well as the procedure. The control law is implemented in Labview through a formula node. The parameter p is chosen equal to 1000 to be compliant with the simulated test cases. However, the parameter p has no influence on the controller response as long as the convergence is not certain. Fig. 3.19 shows the attempt to control the mass flowrate using the sliding mode control approach: a step command is given as input to the system but the response is not controlled. The switching frequency is driven by the sampling time, which happens to be too slow compared to the response of the system. For this reason the output oscillates with a large amplitude between the maximum value, related to the condition of the valve fully open, and the minimum value, that is when the valve is turned off. It is remarkable to show how the simulations could predict the same behaviour whenever a finite sampling time of $t_s = 40\ ms$ was introduced in the Simulink model. If Fig. 2.39 is compared to Fig. 3.19, one could see how the large oscillations in the simulation are compatible with the test results. The real test shows smoother peaks than the simulation results; the reason might be linked to the fact that the dynamics predicted by the model is slightly faster than the actual one, yielding a steeper rise and decay in the flowrate.

The modifications made to the classic SMC control scheme, which are treated in section 2.5.7 are based on the results of the test hereby described. The minimum sampling time is too large to perform a successful control using a classic SMC control, hence the opening time of the valve should be limited to the minimum spike time, regardless of the sampling time.

3.6. Complete Micro-Propulsion System

The contingent objective of the thesis is the integration of the complete micro-propulsion system, including the propellant tank, the micro-valve, the VLM micro-thruster and the required electronics for sensing, valve actuation and heaters control. The tests are performed both to verify the compliance of all the elements for a preliminary configuration of the micro-propulsion system and, of course, to implement the closed-loop thrust control system.

3.6.1. Complete System: Experimental Setup

The micro-propulsion system comprises several components:

- Propellant tank: a pressurized cartridge filled with N_2 and attached to the micro-valve feeding line;
- 5 bar MS5803-05BA pressure/temperature sensor located at the tank outlet;
- Lee VHS Micro-valve, shown in Fig. 3.2;
- Delta Elektronica ES 030-10 power supply at 12 V for valve actuation;
- Power conditioning board for valve actuation that implements the spike and hold circuit, shown in Fig. 3.2;
- VLM device mounted on a customized interface for easy fluidic connection and sensing, shown in Fig. 3.20;
- 30 bar MS5837-30BA pressure/temperature sensor in the thruster upstream with respect to the chamber;
- NI USB-8451 for sensors' signal readout, as described in section 3.1;
- Delta Elektronica ES 030-10 power supply for the thruster heaters;
- Two thermo-couples located at the nozzle;
- NI-9211 for acquiring thermo-couples measurements.

The pressure at the tank is measured with a 5 bar pressure sensor, only compatible with gas. This is done to avoid any conflicts in I^2C addressing between the sensors, since the thruster has an integrated 30-bar pressure sensor. The pressure measurement at the tank is used to determine the mass flowrate through the system, as explained in section 3.5. However, when the entire system is integrated the mass flowrate is one order of magnitude lower than the level used in the previous tests, yielding an extremely noisy signal. It is hard to distinguish the real measurements from the noise. Consequently, the mass flowrate calculated using pressure data cannot be taken as reference for the analysis. To perform the control loop, the pressure in the thruster is taken as the process variable.

The VLM device, shown in Fig. 3.20 with its interface structure, is monitored during operations by a set of pressure and temperature measurements. The liquid parameters are registered upstream of the chamber inlet and the temperature is affected by the structure heating dissipation. Moreover, the heaters resistance is measured constantly to derive the temperature by a simple correlation between $R[\Omega]/T[K]$. The temperature of the VLM device is also registered downstream, close to the nozzle, by two thermo-couples. In this fashion, the temperature gradient between the heaters and the edge of the chip can be registered to assess the conductivity, and hence the potential dissipation, of the micro-thruster.

Fig. 3.21 shows the complete setup and the schematic of the main components.

3.6.2. Complete System: Experimental Procedure

The complete micro-propulsion system has been tested in two different scenarios.

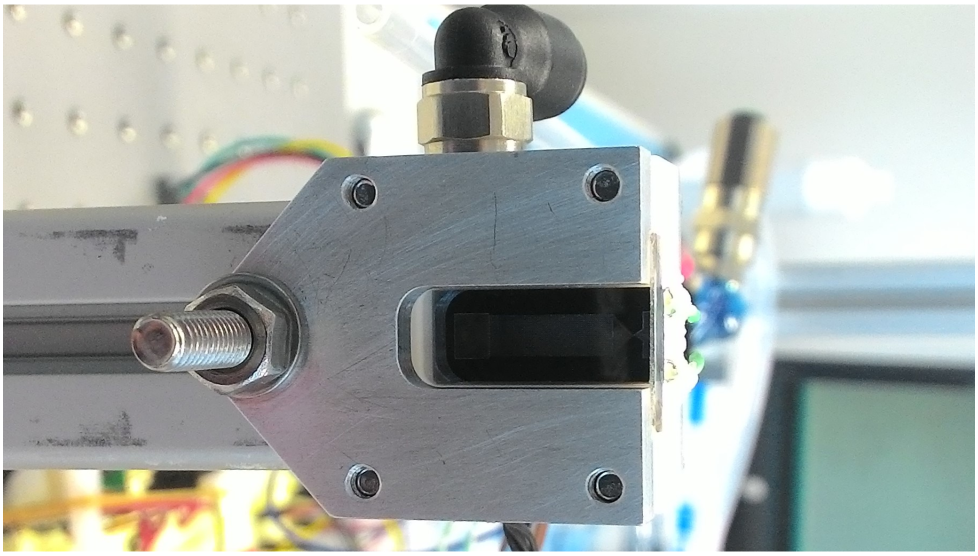

Figure 3.20: A close-up of the VLM chip mounted on the interface structure.

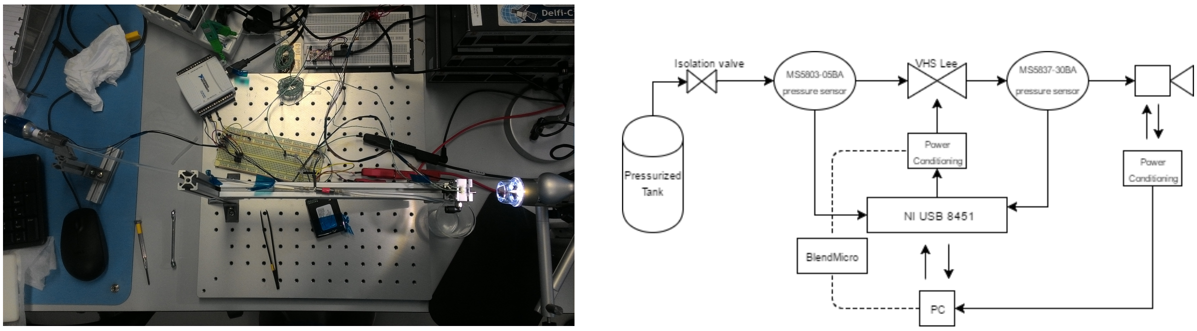

Figure 3.21: Overview and schematics of the test bench for the integrated micro-propulsion system

Uncontrolled System The uncontrolled operation is performed by integrating the three main components, namely the tank, the valve and the microthruster, and opening the valve completely so that the system reaches a stable point based on the tank pressure. The tank is first filled with pressurized Nitrogen and weighted to determine the amount of gas employed for mass flowrate calculation. The heaters of the microthruster are turned on to bring the VLM to a temperature of $160 - 180\ ^{o}C$, enough to vaporize the water. The valve is then opened and the boiling inside the chamber is monitored to prevent liquid water to be ejected through the nozzle. In case the temperature of the thruster is not high enough to perform a complete vaporization of the inlet flowrate, the heaters' power is increased manually to yield a stable vaporization. There are three ways to control the power delivered to the heaters:

1. **Manual Control**: the voltage of the power supply is changed manually from the Labview code;
2. **Power Control**: the set-point for the power is set and a simple PID control is implemented to determine the required voltage from the power supply;
3. **Temperature Control**: the set-point for the temperature is set and a simple PID control is implemented to determine the required voltage from the power supply;

Normally, the temperature control mode is used. If unexpected behaviour occurs, the mode is switched to manual that sets instantaneously the voltage to a safe value, usually 0 V.
The valve is simply switched on and off using the Labview code. A dedicated power supply, which delivers the 12 V signal to the valve spike and hold circuit is manually controlled.

To finalize the test, the valve is turned off until the inner cavity of the VLM is completely dry. The correct instant at which the test can be safely concluded is determined both by the pressure measurements, which need to step back to atmospheric pressure, and by visual inspection of the VLM chamber.

Controlled System The ultimate goal of the thesis project is to develop a preliminary control system for regulating the thrust delivered by the microthruster. The thrust is generated by accelerating the water vapor, present inside the chamber, through the nozzle. According to ideal rocket theory in section 1.2.5, the mass flowrate ejected through the nozzle is determined by the pressure inside the chamber. In a resistojet, as the VLM, the pressure builds depending on the vaporization rate, which in turns is regulated by the inlet mass flowrate and the heat transfer between the heaters and the liquid. As already mentioned in Chapter 1, this thesis focuses on the regulation of the mass flowrate flowing into the thruster.

For the controlled system, the micro-valve can be actuated in two different modes:

1. **Manual Mode**: the duty cycle fed to the PWM actuation signal is inserted manually;
2. **Automatic Mode**: the actuation of the valve is done automatically following two different control schemes.
    (a) PID control: the duty cycle of the PWM is adjusted according to the law used in section 3.4;
    (b) ON/OFF control: the control has a bang-bang action, coming from a modified version of the SMC controllers developed in section 2.5.7. The process variable is the pressure inside the chamber.

The manual mode for valve actuation, together with the manual control of heaters power, are included to cope with unexpected behaviours that may occur during the operation of the micro-thruster. The actions described in the previous paragraph are valid also for the tests of the controlled system. Given that the pressure inside the thruster's chamber is varied, the boiling needs to be monitored carefully to prevent liquid water from flowing through the nozzle, especially when the set-point is changed. However, the temperature was kept constant at $110^{o}C$ for the entire test, since the boiling proceeded flawlessly.

3.6.3. Complete System: Results and Discussion

The tests showed a successful operation of the integrated system, setting an important milestone in the development of the micro-propulsion system. The results for the controlled and uncontrolled systems are analyzed in the following paragraphs.

Uncontrolled System The relevant data for the analysis worked out in this thesis are essentially the tank pressure, the thruster pressure and the mass flowrate. Since the mass flowrate measurements are not meaningful, due to poor accuracy, they are not reported here. Fig. 3.22 shows the tank and thruster pressure during the test. At the instant the valve is actuated the pressure builds quite rapidly to the steady-state value, which is very close to the upstream pressure in the tank. The test started with a pressure in the tank of approximately $2700\ mbar$. The decay in pressure is rather slow, around $100\ mbar$ for a 9-minutes test. The pressure in the thruster is affected by the frequency of the boiling process. For this reason, the measurements of the pressure inside the thruster happens to be more noisy than the tank readouts.

The dip in pressure at $t \sim 310\ s$ may be due to an error in the sensor's reading, either in the I^2C interface board or in the Labview code. Potentially, the drop in pressure may have been caused by the explosion of an air bubble, accidentally present in the feeding tube. The latter option is justified by the similarities between the rise in pressure at the beginning of the operations and at the moment in which pressure is restored after the drop. If it was a reading error, one would expect a much steeper restoration in pressure without smooth transition to the steady-state value.

For the sake of comparison, the theoretical thrust can be calculated by coupling Eq. 2.75 and 2.76. For the test results, the temperature of the chamber is known and can be used to calculate the mass

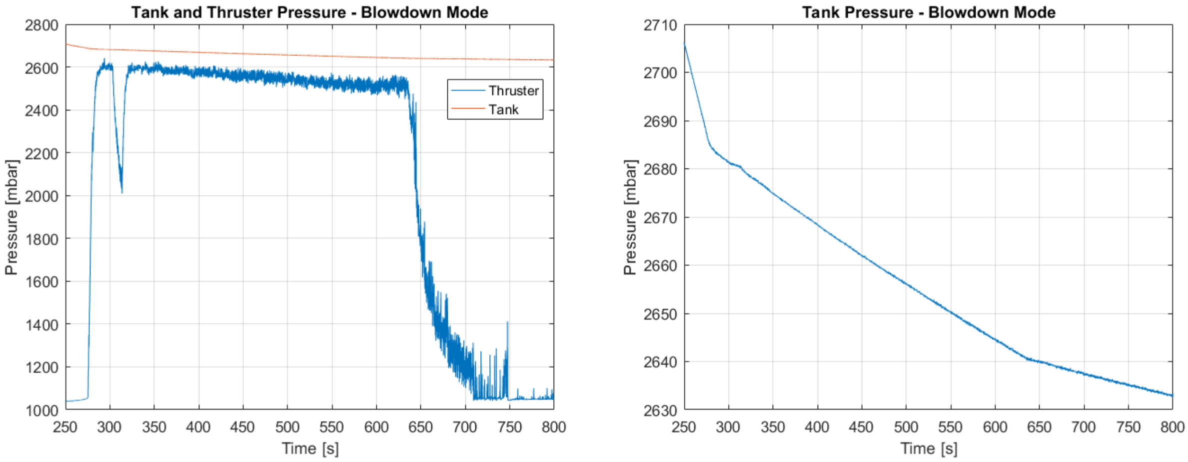

Figure 3.22: Tank pressure and thruster pressure during the blow-down uncontrolled test. On the right, a close-up of the tank pressure is presented.

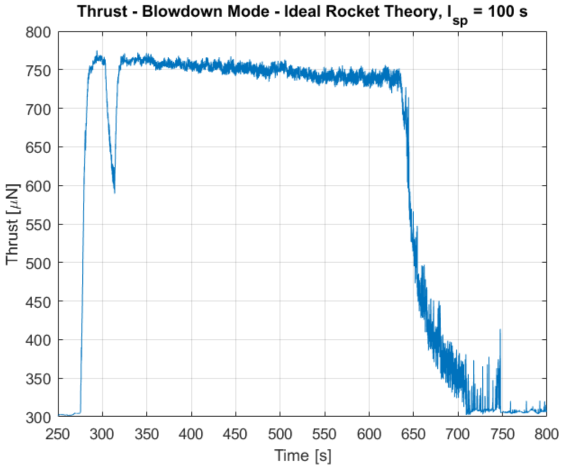

Figure 3.23: Thrust level calculated with the ideal rocket theory, using chamber pressure and chamber temperature from the experimental data. The speicific impulse is set to $100\ s$.

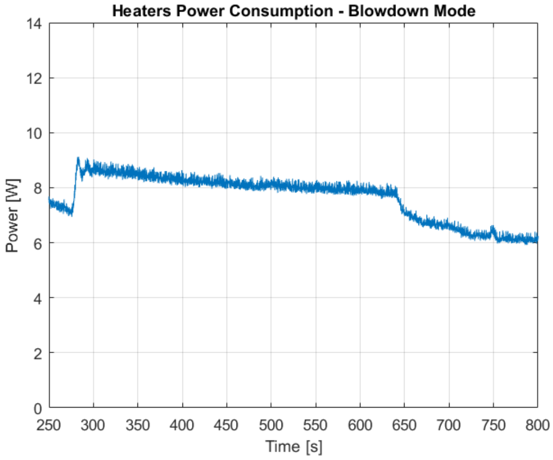

Figure 3.24: Power consumption of the VLM heaters during the full test.

flowrate according to the standard version of the ideal rocket theory in Eq. 1.43. The results for the thrust is far from being completely adherent to the actual delivered performance, since several assumptions are used:

- The specific impulse is set to $100\ s$, equivalent to the design value [63]. The specific impulse is dependent on the heater power and consequently to the chamber wall temperature [11]. However, characterization tests are still an on-going activity at TU Delft and it is still hard to determine precisely the correlation between the wall temperature and the I_{sp}. Thus, the value of $100\ s$ is considered representative and close enough to the real value for the purpose of this work.
- No performance losses are taken into account, such as the nozzle efficiency.

Nevertheless, the thrust predicted by the simulations, using the same assumptions as above and the same parameters, is compatible with the test results, as will be discussed in the next Chapter 4. Fig. 3.23 shows the results for the calculated thrust.

Finally, the power consumption of the entire system is determined by the voltage and current readings of the two power supply. The power consumption of the heaters is shown in Fig. 3.24. It ranges from a minimum of $6\ W$ at the end of the experiment to a maximum of $9\ W$, occurring at the beginning of

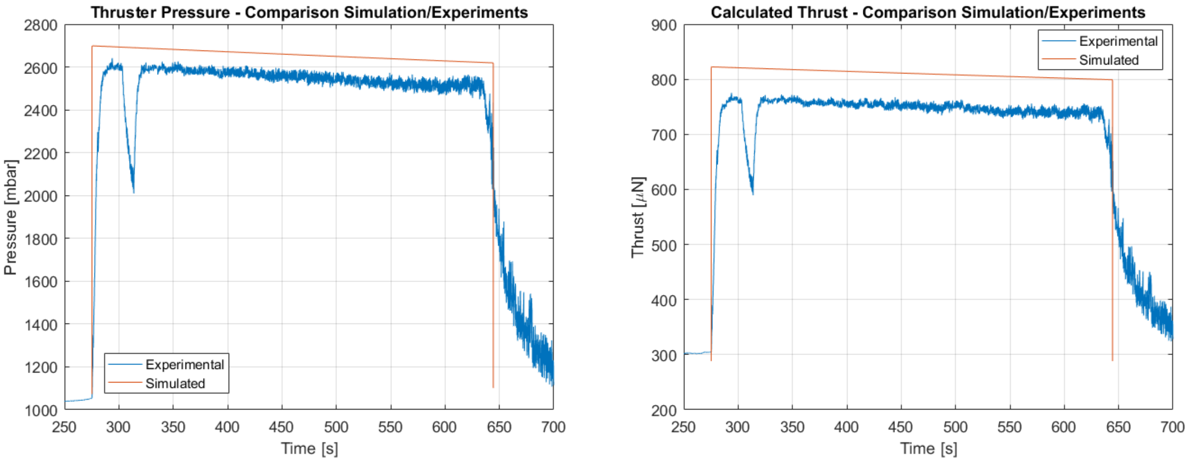

Figure 3.25: Comparison between simulated results and experimental data for the pressure in the VLM chamber for the uncontrolled system. The computed thrust is also compared as a post-processed variable.

the test where the pressure is higher. During steady-state operation, the average power consumption is $8.3\ W$. The power delivered to the heaters is dissipated by the interface structure that holds the thruster in place. Such structure warms up considerably during operation, meaning that it absorbs a significant fraction of heat and, in turns, dissipate it via convection.
The actuation of the valve is provided by the spike and hold circuit. During operations the valve is open and kept on for the entire test. The voltage provided by the power supply is $12\ V$ and the current is rather stable at $300\ mA$. The power required for the valve is:

$$P_{valve} = V \cdot I = 3.60\ W \tag{3.9}$$

Summing up the power required to actuate and operate the valve as well as that necessary to vaporize water, a preliminary estimate of the power consumption of the complete micro-propulsion system is:

$$P_{prop,sys} \sim 11.9\ W \tag{3.10}$$

The experimental results are compared to the results from the simulations. The comparison is shown in Fig. 3.25. The response time of the simulated system is faster than that found in the test. The analytical model neglects the boiling process, hence the time for building the pressure is underestimated. The thruster's steady-state pressure value differs 5% between the simulated and the experimental results, whereas it goes up to 7% for the computed thrust. The fall in pressure, when the valve is turned off, is not well resembled and the simulations deliver a faster transient. The discrepancy may be due to the fact that the boiling process is neglected in the analytical model; when the valve is turned off, water is still present in the VLM chamber that keeps boiling until it vanishes as the pressure does the same consequently. Although the model still needs to be improved, the comparison shows a good agreement between the simulation and the test of the comprehensive micro-propulsion model.

Controlled System The control system does not require any additional hardware, being solely implemented in the Labview code. As already anticipated, the PID control of the valve does not perform satisfactorily. The controllers make use of the mass flowrate as the process variable to regulate the duty cycle of the PWM voltage signal as the control variable. The mass flowrate measurement, derived from the pressure sensors, is not able to resolve the low values, $\sim 1\ \frac{mg}{s}$, which are found in the operations of the micro-propulsion system. Such shortcoming negatively affects the effectiveness of the controllers. The pressure in the thruster can be selected as the process variable, instead of the mass flowrate, to guarantee a more precise and accurate signal to be processed. However, although the process variable is changed, controlling the valve by regulating the duty cycle of the actuation PWM voltage signal is not successful. The minimum opening time of the valve is $0.1\ ms$, which is equal to the minimum spike time held by the spike and hold circuit; the flowrate flowing during the minimum opening time of the valve is enough to bring the system to the saturated steady-state, as if the valve

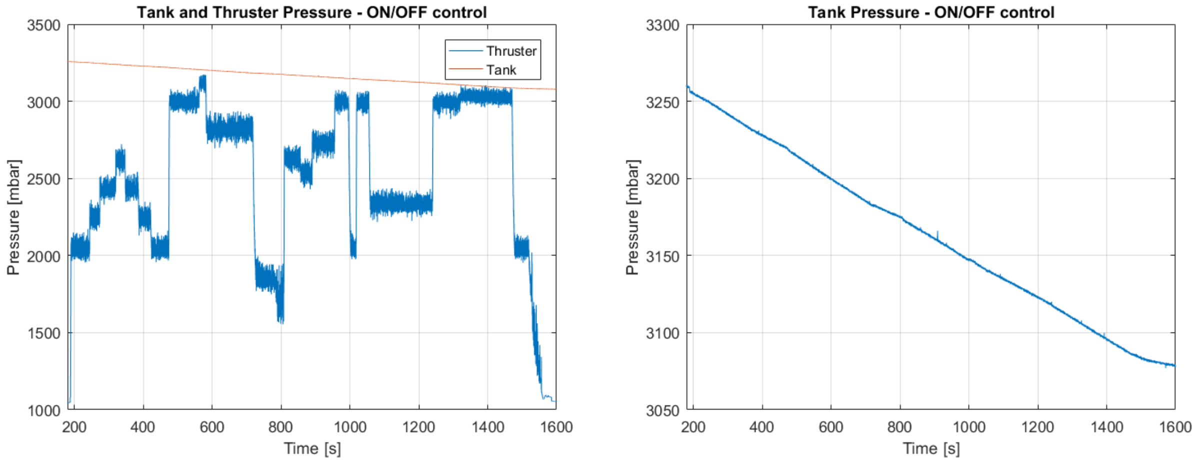

Figure 3.26: Tank pressure and thruster pressure during the blow-down controlled test. On the right, a close-up of the tank pressure is presented. The data are for the full test.

was completely open. As soon as the valve opens the pressure is rapidly built, on the contrary when the valve is turned off the transient behaviour is much slower to bring to zero the gauge pressure. Hence, the minimum allowable duty cycle does not limit the flowrate enough to enable the control of the operating pressure inside the thruster and eventually the thrust.

A regular discretized package of liquid flow, using the Lee Valve, is always above the range of relevant flowrate. The minimum duty cycle, using 250 Hz for the PWM frequency, is found to be 2.5 %, or 6.375 in the scale 1-255. In order to use the full range of duty cycle provided by the Blend Micro board, the frequency must be scaled down to:

$$f_{min} = \frac{1}{255 \cdot t_{min}} = 39.2\ Hz \tag{3.11}$$

where 255 is the duty cycle range delivered by the board and t_{min} is the minimum spike time. The behaviour of the system with a different PWM frequency is similar to the one described above.

The successful test employed the ON/OFF control with a bang-bang strategy, based on the sliding mode control surface. The valve is actuated whenever the sliding surface is negative, according to the control law developed in section 2.5.7. Since the rise transient of pressure, when the valve is actuated, is much faster than the transient fall of pressure, when the valve is turned off, the update on the control input does not follow the sampling time of the sensors. If the control variable actuates the valve, it does it for the minimum amount of time t_{min} and then it shuts it down, without waiting for the next pressure reading. In this way the opening time of the valve is really a minor percentage of the operating time. On one hand, this yields a slower dynamics of the actuator that delivers discretized package of liquid flow at a low frequency, and hence a less accurate control with a prominent chattering behaviour. On the other hand, the time-averaged flowrate that is achieved is much lower than the minimum value attained with the PWM control, thus enabling the control of the pressure inside the thruster chamber.

The full test is performed in nearly 30 minutes, as shown in Fig. 3.26. The initial tank pressure is $\sim 3250\ mbar$ and decays nearly $\sim 200\ mbar$ throughout the test. There are no significant change in the slope of the tank pressure when different operating point are commanded. The flowrate flowing through the system is so low that it is difficult to resolve it from the de-pressurization of the tank. The commanded thruster pressure is changed to several levels and for different time span, as shown in Fig. 3.26. The most relevant part of the experiment, in terms of thrust-control, is the response to the stair-command input, between $\sim 160\ s - \sim 475\ s$.

- **Response Time**: the response time to a change in the command is rather fast, ranging from 1 to $1.5\ s$. As already mentioned, when the pressure has to be built, the system reacts quicker

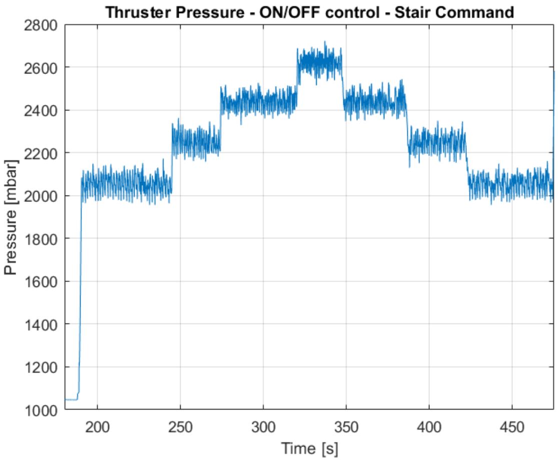

Figure 3.27: Thruster pressure during the stair-command test section. The command is a step-wise increase of pressure in the range $2-2.6\ bar$, with a step of $0.2\ bar$.

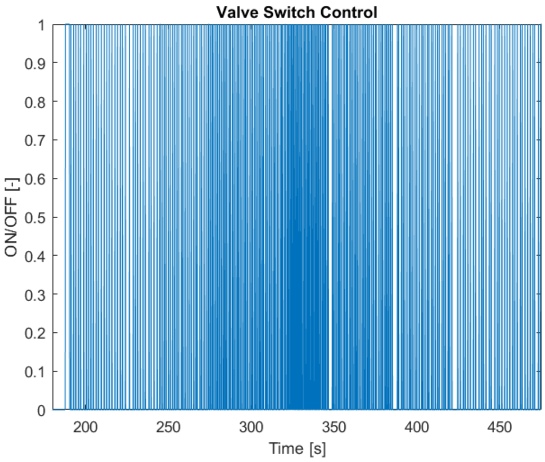

Figure 3.28: Valve actuation switch during the stair-command test section.

than the case in which the commanded pressure is reduced. The difference is estimated in $\sim 1\ s$ on average in the response time.

- **Steady-State Error**: the ON/OFF strategy is highly dependent on the dynamics of the system for the two modes selected by the controller. For instance, if the actuation of the valve delivered the same response as the de-actuation, in terms of settling time, one would expect a symmetric chattering around the commanded set-point. Since the actuation of the valve yields a fast transient, where the flowrate increases almost instantaneously and thus the pressure, the average pressure turns out to be higher than the commanded input. The difference between the commanded input and the delivered averaged pressure is on average 2% of the set-point. This yields a difference of nearly $40\ mbar$ for the analyzed pressure range. One possible solution is to include an adaptive coefficient on the set-point to shift the response to the desired value. In addition, the sliding surface may be used in the original form, where the derivatives of the error may help in reducing the chattering and the steady-state error.

- **Resolution**: no targeted tests have been performed to assess the minimum pressure step that could be resolved. Nevertheless, one could draw insights on the minimum achievable step by analyzing the chattering behaviour, even though potentially improvable. The amplitude of the chattering around the averaged value is $\sim 50\ mbar$. If the resolution criterion is set to be that the averaged value between two consecutive steps needs to differ at least the amplitude of the chattering then $50\ mbar$ is the minimum achievable step.

Also in the case of the controlled system, the experimental results are compared to the results from the simulations. The Simulink model is adapted to match the exact implementation of the test setup. In particular, the sampling time is taken into account to execute the SMC control scheme using the thruster pressure as the process variable. The block diagram showing the most important parts is shown in Fig. 3.29.
Fig. 3.30 shows the comparison between simulations and experimental data for the controlled system. The simulated response of the system is actually worse than the experimental data in terms of chattering around the commanded input. The reason is that the de-actuation dynamics simulated by the analytical model is much more rapid than the real process, nearly $3\ s$ faster. Hence, following the same control scheme adopted in the laboratory setup, the OFF time of the valve leads to an overestimated drop in pressure than the real case. Indeed, unlike the experimental data, the averaged steady-state value is lower than the commanded set-point.

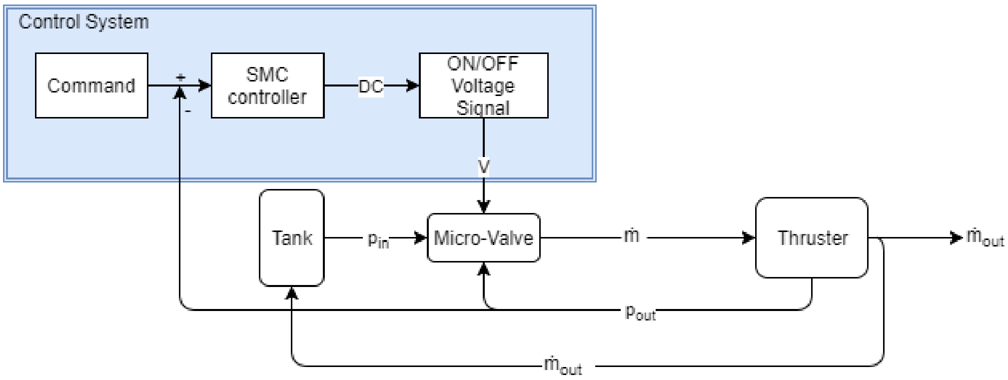

Figure 3.29: Block diagram of the complete SMC-controlled micro-propulsion system. The figure shows the key blocks implemented in the Simulink model, which is not reported here for helping the visualization of solely the important blocks.

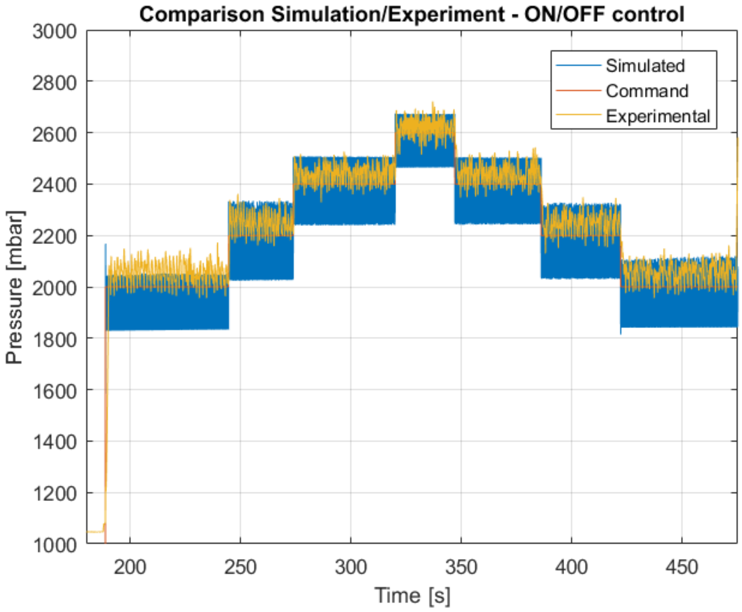

Figure 3.30: Comparison between simulated results and experimental data for the pressure in the VLM chamber for the controlled system.

3.7. Summary and Conclusions

This section summarizes the content of the experimental chapter and draws several conclusions on the laboratory activities described. Since the chapter deals with several different aspects, the different considerations are made separately:

- The analytical model has been validated by characterizing the discharge coefficient of the real device. The model was tuned to match the features of the actual hardware, such as the coil resistance and the solenoid diameter. The results were satisfactory, given that the largest discrepancy was within 15%, found for pressure drops below $1\ bar$. Achieving this good resemblance of experimental data by the theoretical system is promising for the future model's employment.

- The characterization of the valve actuated with a PWM voltage signal has shown that there is an almost-linear relationship between the duty cycle and the output flowrate, excepts for a flattened region for low duty cycle. The linearity is less visible in the simulation results, which show a clear parabolic dependence. Due to hardware limitations, the behaviour of the valve for almost the entire range of duty cycles was unexpected, and not reliable, for a frequency equal to $500\ Hz$.

- The mass flowrate is the best choice for the process variable. The controllers perform better and more accurately if based on the flowrate. Nevertheless, no flow sensors were available and suitable for nano- and pico-satellite applications. Hence, a sensor-less alternative has been investigated to assess the mass flowrate from the pressure readings at the tank. Given that the pressure signal is noisy, the mathematical processing of such variables yields an increase in the noise level. To reduce such disturbances, a 2^{nd} order Butterworth real-time filter has been added to the control loop that helped in smoothing the measurement, despite introducing a delay in the signal. The above-mentioned implementation performs satisfactorily when the flowrate is above $10^{-5}\ \frac{kg}{s}$, whereas it cannot resolve values below that threshold.

- The closed-loop control of the valve has been tested, using the mass flowrate as process variable. Since the commanded flowrate was within the acceptable range for the sensor-less implementation, the PWM-PID control, developed in the modelling Chapter 2, delivered an acceptable control. The continuous PWM-PID control performed better than the discontinuous SMC control, since the large sampling time degraded the performances of the sliding surface control.

- The first test of the uncontrolled complete micro-propulsion system was performed by connecting the pressurized propellant tank, the micro-valve and the vaporizing liquid micro-resistojet (VLM). The system was operational for different pressure levels (up to $8\ bar$) and long time (up to $1.5\ hrs$). The valve was completely open and the pressure drop across it was so low that the mass flowrate reached the order of $\frac{mg}{s}$. The averaged power consumption of the entire system is $\sim 11.9\ W$. This figure is strongly affected by the heat dissipation that occurs in the thruster interface, which is still not optimized for heat insulation.

- Finally, the closed-loop control for the micro-propulsion system has been tested. The very low mass flowrate prevented the use of the sensor-less implementation to perform the control-loop. Furthermore, the minimum achievable duty cycle was already enough to bring the system to the maximum operating point, as if the valve was fully open.

  Due to the above-mentioned reasons, the control scheme was changed based on the insight given by the experiment. A hybrid, based both on theory and tests, SMC control approach was developed where the valve was actuated for the minimum achievable opening time. The process variable is selected as the pressure within the thruster, which is directly linked to the mass flowrate flowing in the system and eventually the thrust. Such control is possible because of the difference on the rise in pressure with respect to the decay, which happens to be much slower. The hybrid control law performed successfully, even though a significant chattering is present in the thruster pressure. A response time of $1.5\ s$ is achieved for a step in the commanded set-point of $200\ mbar$, the steady-state error is within 2% and the resolution is nearly $50\ mbar$, although dedicated tests should be performed to better define the minimum resolved difference.

Although successful tests were performed using the modified-SMC control scheme, the PID-PWM is still an alternative that might be adopted to improve the performance of the controller. The chattering behaviour is relevant, as seen in Fig. 3.27; the PID-PWM would allow a smoother response improving the achievable resolution. As discussed in this thesis, to implement a PID-PWM loop in the complete system, the hardware must be upgraded, especially the micro-valve, to comply with the low mass flowrate values typically required by the system. Nevertheless, the response time and accuracy for the modified-SMC are acceptable and hence such control scheme might be suitable for a flight prototype.

4

Conclusions

The following chapter intends to draw conclusions on the entire work. The results are discussed as a whole to stress the logic behind the adopted work-flow; furthermore, several recommendations are suggested for future works to extend the achievements of the one presented here. Section 4.1 presents a discussion upon all the significant results of the thesis and puts into an overall perspective all the intermediate steps that have been taken. Section 4.2 reports the conclusions for the the thesis and presents the recommendations for follow-up projects.

The ability to control the thrust magnitude delivered by a micro-propulsion system represents a valuable opportunity to enhance the capabilities of nano- and pico-satellites missions. In order to regulate the thrust level of a VLM device, the mass flowrate flowing through the feeding lines is adjusted to meet the commanded output. The fundamental device to achieve such task is the micro-valve that is actuated during the operations of the micro-thruster.

4.1. Discussion on Results

To develop the control concepts an analytical model of the system is required. The model provides a preliminary tool to simulate the performances of the system, as well as to design the controllers, PID for instance. Nevertheless, the model has been developed for future work and reference, inasmuch it may be used to design a customary micro-valve, specific for the micro-propulsion system. On one hand, the analytical model for control purposes needs to be a simplified representation of the physical phenomenon and, above all, easy to handle in terms of equations; on the other hand, if the model represents the baseline for developing newly designed devices, it shall provide an accurate representation of every physical process occurring within the device. Since the model developed in Chapter 2 has such dual objective, the model strategy is the result of a trade-off between accuracy and complexity, yielding a set of equations suitable for control purposes and design.
The two state-space models presented in section 2.1 are similar and the complexity scales up from one to the other. Although the state-space model in Eq. 2.26 is much simpler (less states, linear output relationship), there are several reasons to prefer the modified state-space model presented in Eq. 2.28. First of all, the transient behaviour of the flowrate establishment is not only dependent on the dynamics of the moving plunger; assuming such would mean neglecting any inertia of the fluid and assuming that the fluid flow reacts instantaneously to the change in valve outlet aperture. Fig. 2.17, which is a result of the more sophisticated numerical simulations, shows that the differences between the dynamics of the plunger and the fluid flow establishment are significant and cannot be neglected: for control purposes, the transient behaviour is too important since most of the control depends on the response features of the system, in terms of overshooting and settling time, in addition the fluid flow physics is critical for designing the geometry of the device for future applications. Another reason that defines Eq. 2.28 a more suitable model for this thesis is that it decreases the dependency on experimental coefficients based on the actual device. Specifically, the output equation is defined regardless of the discharge coefficient of the micro-valve. It is true that, in Eq. 2.28, the pressure loss

caused by the abrupt change in fluid direction is represented by an experimental coefficient but it is usually assessed based on the geometry and the area ratio. In any case, the influence of the discharge coefficient in Eq. 2.26 is much greater with respect to the pressure loss coefficient in Eq. 2.21.

The analytical model has been validated by building a numerical model in COMSOL Multiphysics. The validation with a more sophisticated tool is critical for assessing the accuracy of the model regardless of the particular device. The parameters defining the key features of the micro-valve are used similarly in the analytical model and the numerical, yielding a methodology to integrate the results of the two models for developing design options. For instance the pressure loss coefficient for a certain configuration may first be estimated by the numerical simulation and then employed in the analytical model as shown in Fig. 2.12. However, if the objective is to assess the accuracy of two independent approaches, namely the analytic and the numerical, the models may be completely decoupled and the pressure loss coefficient determined by geometrical considerations or by actual data from the device's datasheet. Despite all the assumptions linked to the analytical model, the processes occurring within the micro-valve are well described by the equations 2.28. Section 2.3 describes the comparison between the two models. The results are compatible not only in terms of the output flowrate but also for intermediate results, such as the actuation current. The transient behaviour presents an acceptable compliance in terms of overshooting, however there is a difference in the settling time. The assumption of laminar flow within infinite parallel plates may be improved by more realistic configurations, such as radial flow, although Smal [3] refers a minor improvement at the cost of increased complexity. The steady-state outlet flowrate is estimated with a difference of less than $\sim 15\%$ in the worst case scenario for a 6 V actuation voltage.

The sensitivity analysis showed the dependency of simulation results upon the different parameters, which are set in the model. The stochastic approach is incredibly more meaningful and quick when the number of parameters is conspicuous. Software-based analysis based on gridded test cases (not stochastic) were run to investigate the reciprocal influence but the computational time increased exponentially. Furthermore the global sensitivity analysis allows to explore a larger design space. The sensitivity analysis yields useful results and data for a designer to understand what are the influences of certain parameters, whose control he owns, on the system output. The electric parameters, directly linked to the magnetic force responsible of the actuation, are found to be the most influential on the outlet mass flowrate.

The development of an actual control system for nano- and pico-satellite applications requires, obviously, a real hardware set-up. The objective of the experimental part of the thesis was to implement a control-loop to accurately regulate the mass flow-rate in the micro-valve and, ultimately, to integrate the complete controlled system, including the propellant tank and the VLM micro-thruster as well as all the electronics for the closed-loop control system. The available micro-valve, described in Chapter 3, is a electromagnetic solenoid-actuated device with no proportional capabilities. Since the valve can be solely switched ON and OFF, the control method needs to rely on the actuation strategy, which is based on PWM. A high frequency PWM actuation switches the micro-valve ON/OFF approximating a continuous input whose value is regulated by the PWM duty cycle. The use of ON/OFF micro-valve may be disadvantageous in terms of reliability and complexity of the control, nevertheless proportional valves are usually more bulky and power consuming than simple ON/OFF valves. For the implementation on miniaturized systems, such as nano- and pico-satellites, the size and the power consumption become a major constraint, hence the ON/OFF micro-valves may be regarded as the most suitable to be implemented. The characterization of the micro-valve response to different duty cycles and PWM frequency has been examined both theoretically by means of simulations and experimentally. Fig. 4.1 shows the different results and the influence of the PWM frequency. The test results and the analysis made using the simulations' outcome were critical for choosing the frequency of the PWM signal. As explained in section 2.5.3, the hardware limitations, which are hardly identifiable from the simulations only, drove the choice for the switching frequency. However, for 250 Hz PWM frequency the analytical model delivers a satisfactory approximation of the system response for different duty cycles. In principle, the higher the switching frequency the more the system reacts as if the input was a continuous signal. This, in turns, would allow to decrease significantly the minimum ON time, which determines the minimum achievable flowrate.

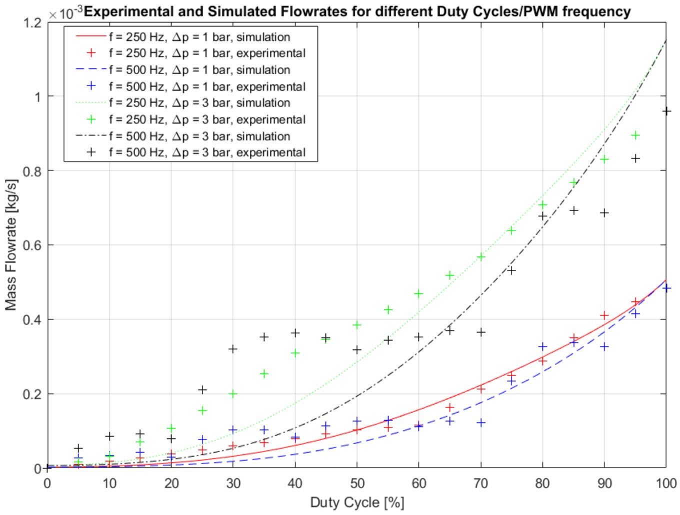

Figure 4.1: Outlet mass flowrate for different PWM frequencies and pressure drop as a function of input voltage PWM duty cycles. The results represent the starting point for the design of the control system.

There are various strategy for controlling the mass flowrate through the micro-valve. Being the first implementation of the closed-loop control system, the simple PID controllers were developed. The process variable is the mass flowrate and the control input is the duty cycle of the PWM. Due to the nonlinearities present in the model, it is impossible to use classic techniques for analytic gain tuning, such as transfer function and, in general, Laplace s-domain techniques. As explained in section 2.5.5, the experimental gain tuning approach is less effective than the innovative averaging approach found in recent literature. The averaging process turns the non-linear discontinuous model into a non-linear system affine in the control input. Such manipulation allows to use linearization to determine the most suitable gains for the controller, at least within the range where the linearization holds. As seen in Fig. 2.37, the superior performance of the controllers tuned using the averaged model is specifically found in the stability of the control variable and the limited oscillations of the process variable.
The experimental results show a satisfactory performance of the controllers. The flowrate is controlled successfully, even if the response time is significantly higher than the simulated one. However, such discrepancy is due to the measurements system for the mass flowrate, which needs to be filtered to obtain a decent signal. The filtering action introduces a delay, as explained in section 3.5, degrading the effectiveness of the controllers only. The flowrate measurements from the pressure readings is not accurate enough for controlling satisfactorily the flowrate for really low commanded inputs. However, in replacement of bulky flowrate sensors, which are not suitable for the integration with the miniaturized satellites, the idea of measuring the flowrate by processing the pressure signal is innovative and promising as well. The promising alternative of using a sliding mode control to regulate the flowrate through the micro-valve has been investigated but due to limitations in the hardware setup it was necessary to come up with a modified version of the discontinuous control, explained in section 2.5.7.

The final part of the work focused on the integration of the entire micro-propulsion system, comprehensive of the propellant tank, the micro-valve and the micro-thruster. The system has been tested in the uncontrolled blow-down mode as well as in the controlled mode, as described in section 3.6. The test represented the first experimental verification of the integration of the complete micro-propulsion system. It was not possible to determine the flowrate flowing through the system due to the low values encountered during operations. Nevertheless, the pressure in the tank, the temperature and all the thruster's parameters were monitored. The test was successfully completed and proved that the VLM can be operated for a long duration ($\sim 1.5\ hrs$) and different pressures (up to $\sim 8\ bar$). Simulations have been run using the same parameters, such as tank pressure and test duration, of the experiment. The comparisons of the pressure inside the thruster and the computed thrust are shown in Fig. 3.25.

The response of the simulated system is more rapid than the one found in the experimental tests. This might be explained by the lack of description of the vaporization process, which is responsible for the transient building of the pressure inside the micro-thruster. Also, the discrepancy in the tail-off section after de-actuating the micro-valve may be due to the fact that there is not a proper description of the boiling occurring inside the chamber. In particular, the water inside the chamber is assumed to vanish as soon as the valve de-actuates, which is not realistic when compared to the experimental results, where there is still water in the chamber to vaporize when the micro-valve is turned off. Although the model still needs to be improved, the comparison shows a good agreement between the simulation and the test of the comprehensive micro-propulsion model.

The limitations coming from the current available hardware prevent the PWM control from working successfully, as explained in section 3.6. The modified version of the sliding mode control scheme has been implemented for a discrete control of the pressure within the VLM chip. The pressure built in the micro-thruster is directly linked to the mass flowrate flowing inside the chamber. The thruster pressure has been chosen as process variable because of a lack of accuracy in the mass flowrate measurement derive from the tank pressure readings. Fig. 3.30 shows the comparison between simulations and experimental data for the controlled system.

The chattering behavior is worse in the simulation results rather than in the experimental. The reason is that the fall in pressure when the valve is de-actuated is much faster in the simulations: assuming the same control scheme, which is an adaptation of the SMC scheme based on experimental considerations, leads to a large OFF time interval that makes the pressure fall excessively. Consequently, the averaged value of the thruster pressure is lower than the set-point, unlike the experimental results.

4.2. Conclusions and Recommendations

The following section draws the conclusion of the entire thesis with respect to the initial objectives and the research questions. Hereby, the comprehensive objective is reported:

The project goal is to improve and enhance micropropulsion capability of nano- and pico-satellites by implementing a closed-loop thrust magnitude control system achieved by controlling the propellant mass flow through the microvalve and in the micro channels of the feeding system.

The overall objective is achieved, as demonstrated throughout the report. The pressure inside the thrust, which is responsible for generating the thrust in the vaporizing liquid micro-resistojet, was successfully controlled by regulating the average flowrate flowing through the system. This enhancement of the micro-propulsion capabilities paves the way to more complex systems that would allow nano- and pico-satellites to perform sophisticated orbital maneuvers.

With respect to the research questions listed in Chapter 1, a set of tentative answers is given:

1. The actuation of the valve was modelled successfully by integrating three different physical processes: electro-magnetic, fluid and mechanical. An important novelty introduced in this thesis is the description of the transient fluid flow by means of simplifies Navier-Stokes equations, derived under the assumption of a fluid flow between infinite parallel plates, isothermal, incompressibile and unidirectional. The drawback of the more accurate description of the fluid flow is the complexity of the mathematics behind the state-space model of the system's dynamics. This is particularly disadvantageous when it comes to design the controllers, where the state-space model is manipulated to derive control concepts theoretically. However, the superior accuracy of the predictions, found in the comparison between the analytical and numerical model, justifies the additional complexity introduced.

2. The continuous control of ON/OFF valves can be done solely by actuating it using a PWM voltage signal and adjusting the duty cycle. If the switching frequency is high enough, the system reacts to the average of the output. The controllers can be designed as simple PID, whose gains are determined by using an averaged model based on the analytical model of the micro-valve. Simulations showed that the controllers performed satisfactorily for a flowrate above $10\ \frac{mg}{s}$, but degraded for lower values of the process variable.
   The sliding mode control (SMC) is a discontinuous control scheme, which is suitable when dealing with model uncertainties. In particular, a modified version of the SMC, based on experimental considerations, was eventually the control law that enabled the regulation of the thruster pressure in the complete system. An important remark is that the simulations were able to predict also the unsuccessful implementation of the classic SMC scheme.

3. A preliminary setup of the closed-loop control for the micro-propulsion system was tested successfully. The continuous control based on PWM-PID did not perform satisfactorily when implemented in the comprehensive system; nonetheless, when the control scheme was tested with the micro-valve only, setting the flowrate to higher values, the results were satisfactory. This means that the concept of continuously regulating the flowrate by adjusting the duty cycle does work, but the current available micro-valve does not achieve the required mass flowrate. Moreover, the continuous control-loop was implemented without any sensor for mass flowrate measurements. Despite its poor accuracy for very low mass flowrates, the concept is promising also in light of all the size constraints and requirements typical of nano- and pico-satellites. Clearly a mass flow sensor helps in improving the accuracy of the control, but a more accurate pressure sensor could do the job either way.
   The discontinuous control based on the modified-SMC control law, using the thruster's pressure as process variable, enabled a successful regulation of the operating point of the thruster and consequently the thrust, with a response time of $1.5\ s$. The discontinuous control yields a significant chattering behaviour around the set-point, nearly $50\ mbar$. To improve such undesired phenomenon, the continuous control, either by modifying the SMC law or by implementing the PWM-PID with another ON/OFF valve, shall be implemented.

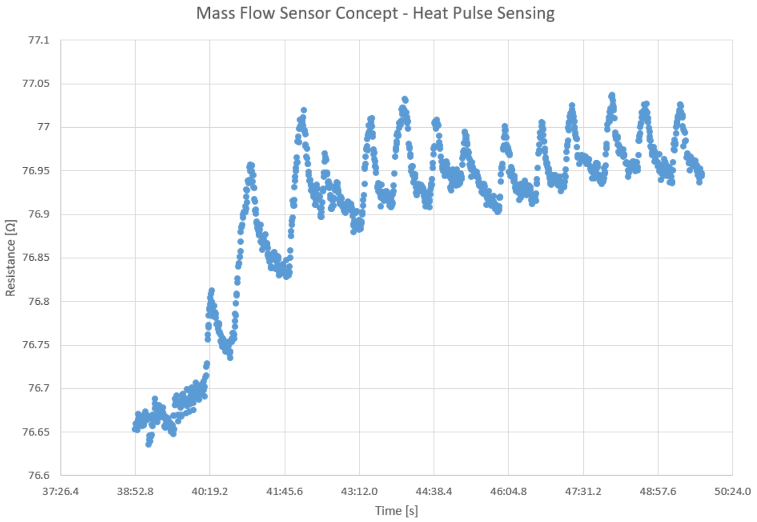

Figure 4.2: Proof of concept for the mass flow sensor using the VLM thruster design.

Being one of the first investigations of the implementation of a closed-loop control system for nano- and pico-satellites, the thesis has opened a lot of opportunities for potential follow-up activities:

- Closely related to the work described in this thesis, several recommendations for future activities can be suggested. First of all, the analytical model might be improved by rethinking the major assumption of the fluid flow between parallel plates. In case this is done, the objective needs to be a reasonable trade-off between complexity and accuracy. If the complexity can be decreased, several control concepts can be investigated such as working out the algorithms for designing a SMC continuous control scheme, suitable for first-order systems. Regarding the control scheme, it would be interesting to study the effects of the vibrations in water, due to the boiling, on the controllers effectiveness. In addition, regarding the complete model, the heating process of the water inside the VLM needs to be included to obtain a more realistic description of the processes inside the micro-resistojet.

  Regarding the experimental setup, it would be interesting to find a component off-the-shelf with a lower actuation voltage and, above all, capable of delivering really low flowrates. In this way, the PWM-PID control could be implemented in the complete model, delivering a more accurate control with less chattering. To further improve the accuracy, the closed-loop control system may be integrated with a mass flow sensor to obtain a precise measurement of the flowrate. Nonetheless, the mass flow sensor needs to be highly miniaturized in order to be suitable for the integration with nano- and pico-satellites.

- The need for a mass flow sensor comes from the poor accuracy that is achieved by processing the pressure readings to obtain the mass flowrate. A potential option is to manufacture a thermal mass flow sensor in-house. A thermal mass flow sensor is basically a sensor that measures the time it takes for a heat pulse to travel, through water, between two known locations. The micro-thruster already presents the required technology for sensing, given that the thermo-heaters have a temperature-dependent resistance. Several tests were performed to investigate the feasibility of the concept: the sensing of the heat pulse travelling through the structure, hence without water, was proved, as shown in Fig. 4.2. Despite this partial success, multiple aspects need to be investigated thoroughly and could not be treated in this thesis due to the limited available time: first of all, the inner cavity needs to be designed to facilitate the fluid flow with an easy geometry, such that it is possible to reconstruct the mass flowrate value from the velocity; secondly, there is a need to prevent the heat pulse to travel through the structure and be sensed at the downstream resistor because this might prevent the identification of the heat pulse carried by water. Finally, more reliable electric connection and a solid support structure need to be designed.

- The micro-valve for micro-propulsion can be designed and manufactured in-house. Since different problems have been encountered with the performance level of the actual valve and given the lack of alternatives in the market, it could be a promising option that of manufacturing a micro-valve for micro-propulsion purposes. The results of the survey regarding the different actuation principles of customary micro-valve found in literature are reported in Tab. 1.1.
- The control loop is currently implemented in the LabView code, hence a computer is needed for the operations and testing. For a real implementation of the closed-loop control system, the control scheme has to be transferred into a microcontroller or into analog electronics, which make use of comparator and amplifier op-amps. Regarding the implementation using a microcontroller, the task would be to translate the LabView code to the low-level coding language used to instruct the microcontroller.

Bibliography

[1] R. Munson, D. F. Young, T. H. Okiishi, and W. W. Huebsch, *Fundamentals of Fluid Mechanics*, 6^{th} ed. (John Wiley & Sons, 2009).

[2] J. A. C. Benignos, *Measurement and Modeling of the Flow Characteristics of Micro Disc Valves*, Master's thesis, Massachusetts Institute of Technology (2001).

[3] O. Smal, B. Raucent, and H. Jeanmart, *Fluid flow modelling of a micro-valve,* International Journal for Simulation and Multidisciplinary Design Optimization (2009).

[4] M. C. Carrozza, A. Arena, D. Accoto, A. Menciassi, and P. Dario, *A sma-actuated miniature pressure regulator for a miniature robot for colonoscopy,* Sensors and Actuators (2003).

[5] M. Bidabadi, M. A. Heidari, and A. Rahbari, *A novel analytical model of a mems vaporizing liquid micro thruster,* in *Iran University of Science and Technology, Dept. of Mechanical Engineering, Conference Paper* (2010).

[6] A. Pavlov, N. van de Wouw, and H. Nijmeijer, *Frequency response functions and bode plots for nonlinear convergent systems,* in *Proceedings of the 45th IEEE Conference on Decision & Control* (2006).

[7] K. J. Åström and T. Hägglund, *PID controllers* (International Society for Measurement and Control: Research Triangle Park, 1995).

[8] K. J. Åström and R. M. Murray, *Feedback Systems: An Introduction for Scientists and Engineers* (Princeton University Press, 2012).

[9] G. Matticari, M. Materassi, G. Noci, L. Fallerini, and P. Siciliano, *Use of a "wide dynamic range" electronic flow regulator to increase the flexibility and versatility of electric and cold gas small propulsion systems,* in 32^{nd} *International Electric Propulsion Conference* (2011).

[10] G. Noci, G. Matticari, P. Siciliano, and L. Fallerini, *Cold gas micro propulsion system for scientific satellites fine pointing: Review of development and qualification activities at thales alenia space italia,* in 45^{th} *AIAA/ASME/SAE/ASEE Joint Propulsion Conference & Exhibit* (2009).

[11] A. Cervone, B. Zandbergen, D. C. Guerrieri, M. De Athayde Costa e Silva, I. Krusharev, and H. van Zeijl, *Green micro-resistojet research at delft university of technology: new options for cubesat propulsion,* CEAS Space Journal (2016).

[12] A. Meckes, J. Behrens, and W. Benecke, *Electromagnetically driven microvalve fabricated in silicon,* Actuators and Systems (IMSAS) (1997).

[13] Y. Shinozawa, T. Abe, and K. T., *A proportional microvalve using a bi-stable magnetic actuator,* in *Tenth Annual International Workshop on Micro Electro Mechanical Systems, 1997* (1997).

[14] M. M. Micci and A. D. Ketsdever, *Micropropulsion for small spacecraft* (American Institute of Aeronautics and Astronautics, 2000).

[15] S. Shoji and M. Esashi, *Microflow devices and systems,* Journal of Micromechanics and Microengineering (1994).

[16] W. Tang, T. Nguyen, and R. Howe, *Laterally driven polysilicon resonant microstructures,* Sensors and Actuators (1989).

[17] W. O. Kwang and H. A. Chong, *A review of microvalves,* Journal of Micromechanics and Microengineering (2006).

[18] P. Galambos, J. Lantz, M. S. Baker, J. McClain, G. R. Bogart, and R. S. Simonson, *Active mems valves for flow control in a high-pressure micro-gas-analyzer,* Journal of Microelectromechanical Systems (2011).

[19] M. S. Groen, D. M. Brouwer, R. J. Wiegerink, and J. C. Lötters, *Design considerations for a micromachined proportional control valve,* Micromachines (2012).

[20] D. Brouwer, *Design Principles for Six Degrees-of-Freedom MEMS-Based Precision Manipulators*, Ph.D. thesis, University of Twente (2007).

[21] M. Esashi, *Integrated micro flow control systems,* Sensors and Actuators (1990).

[22] E.-H. Yang, C. Lee, and J. Khodadadi, *Development of mems-based piezoelectric microvalve technologies,* Sensors and Materials (2007).

[23] I. Chakraborty, W. Tang, D. P. Bame, and T. K. Tang, *Mems micro-valve for space applications,* Sensors and Actuators (2000).

[24] P. Shao, Z. Rummler, and K. Werner-Schomburg, *Polymer micro piezo valve with a small dead volume,* Journal of Micromechanics and Microengineering (2004).

[25] J. S. Bintoro, *An electromagnetic actuated microvalve fabricated on a single wafer*, Ph.D. thesis, Georgia Institute of Technology (2004).

[26] K. Williams, N. I. Maluf, E. N. Fuller, R. J. Barron, D. P. Jaeggi, and B. P. van Drieenhuizen, *A silicon microvalve for the proportional control of fluids,* in *10th International Conference on Solid-State Sensors and Actuators* (1999).

[27] E. T. Carlen and C. H. Mastrangelo, *Paraffin actuated surface micromachined valves,* (2000).

[28] J. S. Fitch, A. K. Henning, E. B. Arkilic, and J. M. Harris, *Pressure-based mass-flow control using thermopneumatically-actuated microvalves,* in *Proceedings-Sensors and Actuators Workshop* (1998).

[29] C. M. Pemble and B. C. Towe, *A miniature shape memory alloy pinch valve,* Sensors and Actuators (1999).

[30] J. Barth, C. Megnin, and M. Kohl, *A bistable shape memory alloy microvalve with magnetostatic latches,* Journal of microelectromechanical systems (2012).

[31] N.-T. Nguyen and S. T. Wereley, *Fundamentals and Applications of Microfluidics* (MEMS Microelectromechanical Systems Series, 2002).

[32] M. Athayde Costa e Silva, D. Cordeiro Guerrieri, and A. Cervone, *State space modeling of fluid flow for thrust control in mems-based micropropulsion,* in *Space Propulsion Conference 2016* (2016).

[33] A. Abed, *Dynamic model of pressure regulating valve,* International Journal of Engineering Sciences & Research technology (2014).

[34] A. J. Ortega, B. N. Azevedo, L. F. G. Pires, A. O. Nieckele, and L. F. A. Azevedo, *A numerical model about the dynamic behavior of a pressure relief valve,* in 12^{th} *Brazilian Congress of Thermal Engineering and Sciences* (2008).

[35] B. J. Patil and V. B. Sondur, *Mathematical modeling and simulation of direct acting pressure relief valve with the effects of compressibility of oil using matlab simulink,* International Journal of Latest Trends in Engineering and Technology (IJLTET) (2013).

[36] J. R. Valdes, M. J. Miana, J. L. Nunez, and T. Putz, *Reduced order model for estimation of fluid flow and flow forces in hydraulic proportional valves,* Energy Conversion and Management (2008).

[37] K. W. Oh, K. Lee, B. Ahn, and E. P. Furlani, *Design of pressure-driven microfluidic networks using electric circuit analogy,* The Royal Society of Chemistry (2012).

[38] P. Galambos, C. D. James, J. Lantz, R. C. Givler, J. McClain, and R. J. Simonson, *Passive mems valves with preset operating pressures for microgas analyzer,* Journal of microelectromechanical systems (2009).

[39] D. Maurya, S. Das, and S. Lahiri, *An analytical model of a silicon mems vaporizing liquid microthruster and some experimental studies,* Sensors and Actuators (2005).

[40] G. P. Sutton and O. Biblarz, *Rocket Propulsion Elements*, 7^{th} ed. (John Wiley & Sons, 2001).

[41] C. A. J. Hanselaar, *Evaporative Two-Phase Micro-Flow Modelling*, Master's thesis, TU Delft (2016).

[42] P. Rangsten, Palmer, K., J. Bejhed, A. Z. Salaverri, K. Jonsson, and T.-A. Gronland, *Closed-loop thrust control in a mems-based micro propulsion module for cubesats,* in 27^{th} *Annual AIAA/USU Conference on Small Satellites* (2013).

[43] P. Rangsten, J. Bejhed, H. Johansson, M. Bendixen, K. Jonsson, and T.-A. Gronland, *Advanced mems components in closed-loop micro propulsion applications,* in 26^{th} *Annual AIAA/USU Conference on Small Satellites* (2012).

[44] U. Kvell, M. Puusepp, F. Kaminski, J.-E. Past, K. Palmer, T. Gronland, and M. Noorma, *Nanosatellite orbit control using mems cold gas thrusters,* in *Proceedings of the Estonian Academy of Sciences* (2014).

[45] S. P. Lunge, S. Kurode, and B. Chhibber, *Proportional actuator from on off solenoid valve using sliding modes,* in *1st International and 16th National Conference on Machines and Mechanism* (2013).

[46] N. C. Cheung, K. W. Lim, and M. F. Rahman, *Modelling a linear and limited travel solenoid,* in *Proceedings of IECON '93 - 19th Annual Conference of IEEE Industrial Electronics* (1993).

[47] X. Zhao, L. Li, J. Song, C. Li, and X. Gao, *Linear control of switching valve in vehicle hydraulic control unit based on sensorless solenoid position estimation,* IEEE Transactions on Industrial Electronics (2016).

[48] P. D. Walker, B. Zhu, and N. Zhang, *Nonlinear modeling and analysis of direct acting solenoid valves for clutch control,* Journal of Dynamic Systems, Measurement, and Control (2014).

[49] L. Qiu and K. Zhou, *Introduction to Feedback Control* (Prentice Hall, 2009).

[50] *COMSOL Multiphysics 5.2a: Reference Manual* (2016).

[51] A. Saltelli, M. Ratto, T. Andres, F. Campolongo, J. Cariboni, D. Gatelli, M. Saisana, and S. Tarantola, *Global Sensitivity Analysis. The Prime* (John Wiley and Sons, 2008).

[52] *Sensitivity analysis,* `https://nl.mathworks.com/help/sldo/sensitivity-analysis.html`, accessed: 2017-04-19.

[53] F. Haugen, *PID control* (Tapir - Academic press, 2004).

[54] S. Cajetinac, D. Seslija, S. Aleksandrov, and M. Todorovic, *Pwm control and identification of frequency characteristics of a pneumatic actuator using plc controller,* Electronics and Electrical Engineering (2012).

[55] M. Pipan and N. Herakovic, *Volume flow characterization of pwm-controlled fast-switching pneumatic valves,* Journal of Mechanical Engineering (2016).

[56] X. Shen, J. Zhang, E. J. Barth, and M. Goldfarb, *Nonlinear model-based control of pulse width modulated pneumatic servo systems,* Journal of Dynamic Systems, Measurement, and Control **128** (2005).

[57] B. Hejrati and F. Najafi, *Accurate pressure control of a pneumatic actuator with a novel pulse width modulation–sliding mode controller using a fast switching on/off valve,* Journal of Systems and Control Engineering **227** (2012).

[58] S. Hodgson, M. Tavakoli, M. Tu Pham, and A. Leleve, *Nonlinear discontinuous dynamics averaging and pwm-based sliding control of solenoid-valve pneumatic actuators,* IEEE/ASME Transactions on Mechatronics **20** (2015).

[59] W. Perruquetti and J. P. Barbot, *Sliding Mode Control in Engineering* (Control Engineering - Marcel Dekker Inc., 2002).

[60] T. Nguyen, J. Leavitt, F. Jabbari, and J. E. Bobrow, *Accurate sliding-mode control of pneumatic systems using low cost solenoid valves,* IEEE Transactions on Mechatronics (2007).

[61] J.-H. Lee, Y.-W. Yun, H.-W. Hong, and M.-K. Park, *Control of spool position of on/off solenoid operated hydraulic valve by sliding-mode controlle,* Journal of Mechanical Science and Technology 29 (2015).

[62] M. R. Adeli and H. Kakahaji, *Modeling and position sliding mode control of a hydraulic actuators using on/off valve with pwm technique,* in *Electrodynamic and Mechatronic Systems - Proceedings of 2011, 3rd International Students Conference on Electrodynamics and Mechatronics, SCE III* (2011).

[63] T. van Wees, C. Hanselaar, E. Jansen, I. Granero, A. Cervone, and B. Zandbergen, *Design, fabrication , testing and modelling of a vaporizing liquid micropropulsion system,* in *Space Propulsion Conference* (2016).

[64] M. Drosg, *Dealing with Uncertainties. A Guide to Error Analysis* (Springer, 2009).

[65] L. Tan, *Digital Signal Processing : Fundamentals and Applications* (Academic Press, 2008).